School of Chemical and Petroleum Engineering

Department of Chemical Engineering

Advanced Yolk-Shell Nanoparticles as Nanoreactors for Catalysis

Meiwen Wang

This thesis is presented for the Degree of

Doctoral of Philosophy

of

Curtin University

October 2017

Declaration

To the best of my knowledge and belief this thesis contains no material previously published by any other person except where due acknowledgement has been made. This thesis contains no material which has been accepted for the award of any other degree or diploma in any university.

Signature:  Date: 24/10/17

(Meiwen Wang)

Acknowledgement

First of all, I would like to take this opportunity to express my gratitude to my principle supervisor, Prof. Shao-bin Wang, for his invaluable advice and helps in research and also financial support for conducting characterization measurements at UWA microscopy centre.

Secondly, I sincerely thank my co-supervisor, Dr Jian Liu, for whose guidance and encouragement throughout my PhD study. He has given me many inspirations in research. Without his counselling and training, I could not make it this far today. It is my real honour to be a student under his supervision.

Subsequently, I would like to thanks my peer colleagues, Dr Yash Boyjoo and Hao Tian, for contributing many brilliant suggestions in conducting experiments and writing manuscripts. Moreover, not forget to mention my research mates from other groups, Dr Chao Su, Dr Yi Cheng, Wenjie Tian and Ping Liang, for their invaluable time to carry out application testings for my samples.

Here, I would also express my appreciations to UWA CMCA microscopy centre technical staffs, Assoc/Prof Martin Saunders, Dr Alexandra Suvorova, Dr Aaron Dodd and Ms Lyn Kirilak for their kind helps in conducting sample characterization measurements.

Last but not least, I thank the Curtin Chemical Engineering laboratory technician team members for their full support in purchasing chemicals and training for analytic instruments.

Abstract

Yolk-shell structured nanocatalysts are believed to be one of the most promising structured nanoparticles to improve catalytic activity, stability and recyclability. Many researchers and scientists have stated that structural design of nano-scale catalysts is as important as selecting the suitable materials. The unique structure and myriad of applications have made yolk-shell structured nanoparticles receiving immense scientific interests. A brief overview of recent yolk-shell structured nanocatalysts synthesis methods and research progress are done to gain the principle understanding of this advanced structured nanoparticles; summarize the catalytic performances of these nanocatalysts covering photocatalysis, methane reforming and electrochemical conversion in the last five years. To design the facile synthesis routes for yolk-shell structured nanoparticles, copper oxide (CuO), resorcinol-formaldehyde (RF) and silica (SiO_2) are firstly chosen as the materials for studying the effects of synthetic parameters in fabrication. The basic and popular selective etching method is used for generating CuO@SiO_2 yolk-shell nanocatalysts. It is discovered that polymers such as PVP and CTAB have great impact on restricting the growth and affecting the shape of metal or metal oxide nanoparticles. Base on this study, CuO and RF are then further employed for the designed generation of Core-shell Cu/ɣ-Fe_2O_3@C and yolk-shell structured Cu/Fe@ɣ-Fe_2O_3@C nanocatalysts. CuO is used as the template, RF as the carbon resource for the carbon shell and iron nitrate solution as the iron precursor forming ɣ-Fe_2O_3 cores. With increasing carbonization temperature and time under nitrogen gas flow, solid ɣ-Fe_2O_3 cores transfers into yolk-shell Fe@ɣ-Fe_2O_3 cores via Ostwald ripening. The electrocatalytic activity for oxygen reduction reaction (ORR) is investigated on such catalysts exhibiting better catalytic performances in compared with other Fe-based nanocatalysts. Subsequently, iron precursor is replaced by cobalt nitrate and nickel nitrate for further study. In contrast with iron precursor, cobalt and nickel precursors are not strong enough to etch all CuO templates with the same adding amounts of iron precursor, forming Ni-Cu/Cu_2O@C and Co-Cu/Cu_2O@C core-shell particles. CuO template is reduced to Cu_2O and Cu during the annealing process under nitrogen gas flow. ORR tests are carried out once more for these core-shell particles. Testing results suggest that Cu/Cu_2O@C and Co-Cu/Cu_2O@C core-shell particles

possess good catalytic activities towards ORR, and the ultra-fine Co_3O_4 nanoparticles attribute to the better performance of Co-Cu/Cu_2O@C particles. The continuation of facile synthesis method design is further extended to Titanium oxide (TiO_2). Yolk-shell TiO_2@TiO_2 particles have been fabricated through a four-step synthesis method using titanium(IV) butoxide as the titanium precursor and resorcinol-formaldehyde (RF) as the sacrificing template. RF layer is removed via gentle calcination to create yolk-shell structure. It is believed that such well-designed semiconductor metal oxide yolk-shell structured nanocatalyst could have great catalytic activity towards many applications, especially for photosynthesis. The synthetic methods applied in fabricating yolk-shell structured nanocatalysts are designed to be facile, environmental friendly and high in controllability, especially for synthesizing metal@metal or metal oxide nanoparticles. Generally, yolk-shell structures are created by employing hard templating method. The removal of hard templates often involves high temperature calcination under air or using highly hazardous chemicals, such steps are usually difficult to control, waste of materials and also could damage the nanoparticles to some extent. The methods have been used in this thesis can fabricate yolk-shell structure while carbonizing the carbon shell under nitrogen gas, and metal oxides can be reduced to metal at the same time. The composition and structure of nanoparticles can be easily controlled by shortening or prolonging the carbonization time, or manipulating the calcination temperature. These methods are also suitable in synthesizing co-catalyst associating nanoparticles; the co-catalyst could form into small clusters co-existing with main catalyst via ion attachment step and annealing process under nitrogen gas.

Publications by the Author

1. Wang M, Su C, Saunders M, Liang J, Shao Z, Wang S, et al. Yolk–Shell-Structured Cu/Fe@γ-Fe2O3 Nanoparticles Loaded Graphitic Porous Carbon for the Oxygen Reduction Reaction. Particle & Particle Systems Characterization.n/a-n/a.

2. Wang M, Boyjoo Y, Pan J, Wang S, Liu J. Advanced yolk-shell nanoparticles as nanoreactors for energy conversion. Chinese Journal of Catalysis. 2017;38(6):970-90.

3. Boyjoo Y, Wang M, Pareek VK, Liu J, Jaroniec M. Synthesis and applications of porous non-silica metal oxide submicrospheres. Chemical Society Reviews. 2016;45(21):6013-47.

4. Gao J, Chen J, Li X, Wang M, Zhang X, Tan F, et al. Azide-functionalized hollow silica nanospheres for removal of antibiotics. Journal of Colloid and Interface Science. 2015;444(Supplement C):38-41.

5. Yin C-Y, Nikoloski AN, Wang M. Microfluidic solvent extraction of platinum and palladium from a chloride leach solution using Alamine 336. Minerals Engineering. 2013;45(Supplement C):18-21.

6. Yin C-Y, Nikoloski AN, Wang M. Microfluidic solvent extraction of copper from malachite-chalcopyrite mineral leach solution. CHEMECA 2012; 23-26 September; Wellington, New Zealand. 2012.

Contents

Chapter 1: Introduction

1.1 Background

Nanoscience and nanotechnology are the scientific terms that only focus on the substances at size range from 1 to 100 nanometers; manipulating at such small scale unleashes the power to change and improve the intrinsic quality of ones (1). Today, nanotechnology plays an extremely important role in commodity production, medical treatment and energy generation; it was initially mentioned in 1959 (2), but was only emphasized after more than 20 years and become popular recently. The advancement of high resolution electron microscopy enables the understanding of nano-scale particles, which is the main factor encouraging the rapidly growth of interests of nanotechnology. Over the past decade, research teams all over the world had put enormous efforts in investigating the potential of nanoparticles to meet the requirement and development needs for modern civilization lifestyle. Effective and sustainable process has become more important and desirable to overcome the drawbacks of conventional production methods. Such requirements have particularly put a great deal on the catalysts being involved in almost all productions, especially energy related processes.

Catalyst acting as a media boosts reaction rate and purifies final products through minimization of by-product or waste products, which is highly significant for achieving sustainability. Catalyst in nano-scale is extremely popular due to its outstanding advantage of high in active sides due to its large catalytic contacting surface area (3-5). However, only reducing size of catalyst could not satisfy the requirement of a good catalyst as most of catalysts tend to be very unstable and deactivated rapidly which is not economically feasible to be used commercially. A good catalyst should possess some distinctive characters, such as stable, high selectivity and activity, able to be recycled, non-toxic and low in cost (5, 6). Therefore, along with the reduction in size, further design of nanocatalysts is necessary. Selection of materials and structural design are the other two main critical factors for improving the performance of nanocatalysts.

Recently, many complex structured nanocatalysts have been fabricated and reported showing extremely good performance in some advanced applications. Yolk-shell architectures are the sparkling ones which received overloaded attentions from scientists and researchers. The unduplicatable merits of such structure solve many encountered problems for catalysis. However, fabricating yolk-shell structure nanoparticles is still under many challenges awaiting more research works to discover facile and precious synthesis methods with scale-up production possibility.

1.2 Research objectives

The main focus of this research is to design the synthesis methods to create yolk-shell structured nanoparticles with well-selected materials for catalysing electrochemical reactions, but not limited to this. The development of fabrication routes are based on the principle fabrication methods, such as selective etching, templating and Ostwald ripening. The following studies were carried out for achieving these goals:

- Synthesized yolk-shell nanocatalysts using the most common and versatile materials, copper oxide and silica, to study the basic effects of synthesis parameters in order to obtain a good understanding of synthesis control.
- Extended experiments to carbon and inorganic metal precursors to fabricate yolk-shell nanocatalysts.
- Designed facile synthesis methods to create nanoparticles having popular transition metals as yolks and carbon as shell.
- Studied the catalytic activity of such nanocatalysts for fuel cell oxygen reduction reactions.
- Further modified the designed yolk-shell nanoparticles with different metal precursors, understood the effects of various precursors in forming yolk-shell structure.
- Extended experiments to titanium oxide, designed sysnthesis method to fabricate titanium oxide yolk with titanium oxide shell, such nanoparticle is believed could be superior applying in photocatalytic applications.

1.3 Thesis organization

This thesis consists of six chapters: introduction, literature review, experimental results and discussions, and conclusion and outlook.

Chapter 1: Introduction

Briefly introduce some basic backgrounds of nanotechnology and nanocatalysts. The research objectives and also thesis organization are also listed in this chapter.

Chapter 2: Literature review

In this part, an intensive and detail summary of latest yolk-shell structured nanocatalysts is given together with the evaluation of basic synthesis methods. The applications of using yolk-shell nanoparticles as catalysts are also introduced and discussed with up-to-date research examples. An outlook of yolk-shell nanoreactors is at the last part of this chapter.

Chapter 3: Brush-like copper oxide encapsulated within mesoporous silica shell yolk-shell nanoparticles

This chapter presents the research activities were conducted to fabricate yolk-shell nanoparticles with common and versatile materials. The particular copper oxide and silica oxide was chosen for this study. Varying the synthetic parameters to study the effects in synthesizing yolk-shell nanoparticles, and also examining the morphology of as-prepared particles using microscopy obtain an understanding on yolk-shell structure fabrication strategies.

Chapter 4: Yolk-shell structured Cu/Fe@ɣ-Fe_2O_3 nanoparticles loaded graphitic porous carbon for the oxygen reduction reaction

A carefully and innovatively designed synthesis method was applied in this study using abundant copper oxide as the base template to create metal or metal oxide with carbon shell yolk-shell nanoparticles. Iron nitrate was used as the incorporate metal source for adding co-catalyst into the perspective nanoparticles. Yolk-shell structured Fe@Fe2O3 yolks formed within carbon shell via simple annealing process. The mechanism was proposed and catalytic performance was evaluated via fuel cell

oxygen reduction reaction, which exhibited comparable performance to other Fe-based nanocatalysts being reported by other research groups.

Chapter 5: Ni and Co doped core-shell structured Cu/Cu_2O cores encapsulated within C shell for fuel cell reactions

Further to the synthesis design from Chapter 4, nickel acetate and cobalt acetate were introduced separately to replace iron nitrate as the amalgamate transition metal precursors added to copper oxide templates. Core-shell structured cores Cu/Cu_2O formed when carbonization process was carried out while Ni transformed into NiO patch attached on Cu/Cu_2O cores and Co seeded the formation of Co2O3 ultrafine nanoparticles co-existing within carbon shell with Cu/Cu_2O cores, respectively. Such resulted nanocatalysts were tested in oxygen reduction reaction and hydrogen evolution reaction showing good catalytic abilities.

Chapter 6: $TiO_2@TiO_2$ yolk-shell nanoparticles as perspective catalysts for photocatalytic reactions

To develop a facile fabrication method synthesizes $TiO_2@TiO_2$ yolk-shell nanoparticles. In this study, a series of experiments were conducted to fine tuning the morphology of $TiO_2@TiO_2$ nanoparticles. Such nanocatalysts are expected to possess great catalytic activity for photocatalytic applications.

Chapter 7: Conclusions and Perspectives

This chapter summaries all works have been reported in this thesis and gives a detail outlook of yolk-shell nanocatalysts.

Reference

1. Stamenkovic VR, Mun BS, Arenz M, Mayrhofer KJJ, Lucas CA, Wang G, et al. Trends in electrocatalysis on extended and nanoscale Pt-bimetallic alloy surfaces. Nat Mater. 2007;6(3):241-7.

2. Toumey C. Plenty of room, plenty of history. Nat Nanotechnol. 2009;4(12):783-4.

3. Chen X, Wu G, Chen J, Chen X, Xie Z, Wang X. Synthesis of "Clean" and Well-Dispersive Pd Nanoparticles with Excellent Electrocatalytic Property on Graphene Oxide. J Am Chem Soc. 2011;133(11):3693-5.

4. Narayanan R, El-Sayed MA. Catalysis with Transition Metal Nanoparticles in Colloidal Solution: Nanoparticle Shape Dependence and Stability. The Journal of Physical Chemistry B. 2005;109(26):12663-76.

5. Lim CW, Lee IS. Magnetically recyclable nanocatalyst systems for the organic reactions. Nano Today. 2010;5(5):412-34.

6. Frenkel AI. Applications of extended X-ray absorption fine-structure spectroscopy to studies of bimetallic nanoparticle catalysts. Chem Soc Rev. 2012;41(24):8163-78.

Chapter 2: Literature Review

2.1 Introduction

Long before the term "nanotechnology" appeared in the scientific world, the concept of micro- or nano-scale work was mentioned by Richard Feynman, on 29 December 1959 in his visionary lecture entitled "There's plenty of room at the bottom". It took more than 20 years for scientists to realize the power behind this concept (1). Our understanding of materials at the electronic and atomic scales relies heavily on the use of electron microscopes. The development of electron microscopy techniques in recent decades has finally enabled scientists to explore the mysteries of the nanoscale world. This has resulted in the "nanotechnology fever" that we are experiencing today. Nanotechnology has enabled many state-of-the-art inventions; one of them is the nanoreactor, an important and innovative creation for mimicking processes that occur in nature. The characteristics of natural processes, such as spontaneity and using the lowest-energy path, enable nature to operate in the smartest way; this has provided inspiration for many artificial materials and processes. Nanoreactors first appeared in the 1990s and became good potential candidates for catalytic applications (2). Nanoreactors replicate the mechanisms of natural catalysts such as enzymes, bacteria, and cellular organelles in boosting reaction rates and production yields. Nanoreactors have several advantages over conventional ones, such as the ability to perform parallel chemical reactions, the elimination of undesirable products, and enhancement of the catalytic performance as a result of large surface:volume ratios. Researchers have therefore devoted much effort to understanding and investigating nanoreactors, especially the relationship between nanoarchitecture and catalytic performance.

High energy demands, limited natural fossil fuel reserves, and the environmental consequences of energy generation are causing great concern globally; therefore much current scientific research is focused on sustainable energy generation. Average energy consumption is increasing because of the increasing global population and development of new technologies. Although the idea of using renewable energy to replace conventionally produced energy arose decades ago, low efficiency, high capital costs, and environmental consequences are challenges that have yet to be tackled. In recent years, catalytic energy conversion, which involves

transformation of energy from one form to another or of wastes to valuable products, has become an attractive method for solving these problems. Energy-conversion techniques such as the use of carbon resources, solar energy conversion, and electrochemical fuel cells have the potential to resolve current difficulties. In terms of catalysis, nanoscale catalysts show enhanced catalytic activities and stabilities, which are essential characteristics for chemical reactions. Among the latest nanocatalysts for energy conversion, catalysts with advanced structures outperform traditional ones, and yolk–shell-structured catalysts give the best performances.

Yolk–shell nanoparticles (YSNs) or "nanorattles" have attracted much attention because of their unique structures and enhanced performances in a wide range of applications, including catalysis, energy storage and conversion, environmental remediation, and nanomedicine. In principle, a yolk-shell structure represents an advanced development of a core-shell structure with a core@void@shell configuration (Figure 2.1 (A)) having high surface area to volume ratio (3-8). Recently, an extensive range of materials have been used to develop yolk–shell-structured nanoparticles to fulfil different needs in various applications. Generally, YSNs have a metal or metal oxide core that is encapsulated in inorganic or polymer shells of various shapes. Silica and carbon are the commonest shell materials because of their simple functionality, high biocompatibility, stability, and abundance (9-12). Conducting polymers are also good shell materials because of their inertness and high conductivity and, most importantly, the possibility of tailoring their functional groups (13). There are many significant variations that can be used to improve the performances and mechanical strengths of YSNs, such as changing the dimension, shell thickness, size uniformity, and nanoparticle shape. Various methods have been developed for synthesizing YSNs with tuneable parameters. These methods include selective etching, soft templating (or bottom-up methods), hard templating, ship-in-a-bottle, Ostwald ripening, galvanic replacement, and use of the Kirkendall effect.

Catalysts should have certain characteristics, including long life, reusability, and high catalytic activity, selectivity, and stability, even in harsh environments (3, 5, 14-16). All these requirements can be satisfied by yolk–shell structures because the YSN core, which is usually the active site for the catalytic reaction, is protected by a shell, and this prevents decay during catalytic reactions (4, 6, 17). Moreover, in many cases, the shells of YSNs are porous and permeable, allowing sufficient diffusion of

reactants in and out of the YSNs through the nanoporous channels, while protecting the metal core from aggregation and sintering (10, 18, 19). The advantages of YSNs as nanoreactors can be summarized as: (1). the manipulable physical and chemical properties of the core and shell; (2). a movable core within the shell for cooperative catalysis; (3). a homogeneous reaction environment for heterogeneous catalysis because the voids act as a reservoir; (4). protection of the catalytic core nanoparticles and suppression of agglomeration; and (5). controllable diffusion rates (3-7, 20-29). Recently, the structures of YSNs have been intensively investigated and have been shown to greatly affect the catalytic performances. Furthermore, the successes achieved using YSNs have led to the rapid development of YSNs with increasingly complex architectures. These YSN architectures can be briefly categorized as: (1). a single core encapsulated in a shell (Figure 2.1(A)); (2). multiple cores within a shell (Figure 2.1(B) and (C)); (3). a single yolk encapsulated in a shell with multiple cores loaded on the shell surface (Figure 2.1(D)); and (4). a single core within multiple shells (Figure 2.1(E)) (3, 5, 24, 30, 31). Among these, a single core within a single shell is the most basic YSN structure and can be achieved using numerous methods. The other YSN structures are generally derived from this basic structural concept. YSNs with multiple cores within a porous shell are favoured because the contact surface area provided by multicores is larger than that provided by a single core, reactant transfer into and out of the core is easier, the catalytic activities are higher, and multiple cores can be either of uniform (Figure. 2.1(B)) or different sizes (Figure. 2.1(C)) (32). A single yolk within a capsule with multiple metal nanoparticles loaded on the shell surface is another category (Figure 2.1(D)). The multiple metal nanoparticles serve as active sites that are different from those in the central yolk. This architecture enables more than one catalytic reaction to be performed and enhances the catalytic performance. A more advanced YSN structure consists of multiple shells with a single core (Figure 2.1(E)). Multiple-shell nanoparticles have higher loading capacities and larger surface areas than single-shell nanoparticles (24). This structure is generally applied for multistep catalytic reactions, and all the materials involved in such nanoparticles must be highly selective to avoid unwanted by-products (24, 33). The best YSN structure cannot be defined because every chemical reaction has its own needs, and the optimum composition, shape, and structure can only be determined based on the YSN performance.

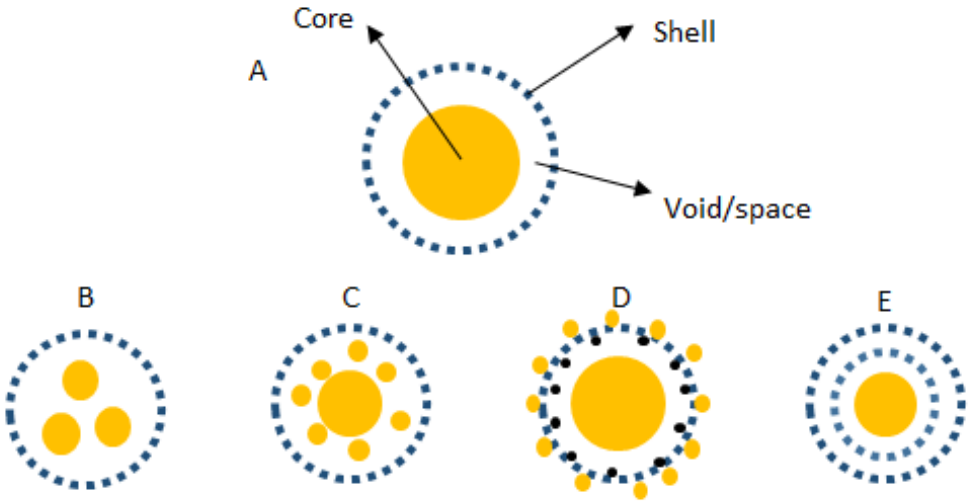

Figure 2.1: Diagram of different spherical architectures of YSNs: (A), core encapsulated in shell; (B), multiple cores within solid shell; (C), core–satellite–shell structure; (D), single yolk encapsulated in shell with multiple cores loaded on shell surface; (E), single core within multiple shells.

Some examples of the use of YSNs as nanoreactors are as follows. Au@ZrO_2 performed well in CO oxidation; Pd@SiO_2 gave a very high production yield (99.5%) in Suzuki coupling reactions; Ni@SiO_2 showed high catalytic activity in steam methane reforming; Au nanoparticles in a permeable carbon shell (Au@HCS) provided an efficient catalyst for the reduction of 4-nitrophenol by $NaBH_4$ to 4-aminophenol (18, 20, 21, 34).

In this chapter, we give a detailed summary of basic methods for YSN synthesis as well as recent advances in applications of YSNs as nanoreactors for energy conversion, with extensive coverage of yolk–shell compositions. Energy-conversion applications include methane reforming, photosynthesis, and electrocatalysis, which are popular and important energy-conversion techniques. Yolk–shell nanotechnology is a relatively new field; therefore many applications are not yet well developed. However, based on the rapid growth of interest in YSN applications, this review brings together the latest achievements in yolk–shell nanoreactors for catalysis, which will contribute greatly to our fundamental understanding and enable further developments.

2.2 Synthetic methods

2.2.1 General synthesis methods

Yolk–shell nanoreactors have great potential for use in an extensive range of applications; therefore many synthetic methods for the preparation of various YSNs have been developed. Different methods are used to obtain specific compositions, architectures, and dimensions. All these approaches have common characteristics: e.g. they are easy to perform, effective, economically viable, and environmentally friendly. Selective etching, soft templating (bottom-up methods), hard templating, ship-in-a-bottle, Ostwald ripening, galvanic replacement, and the Kirkendall diffusion method (Figure 2.2) are general methods for YSN synthesis (3, 20). In this section, we will briefly introduce each method and compare them.

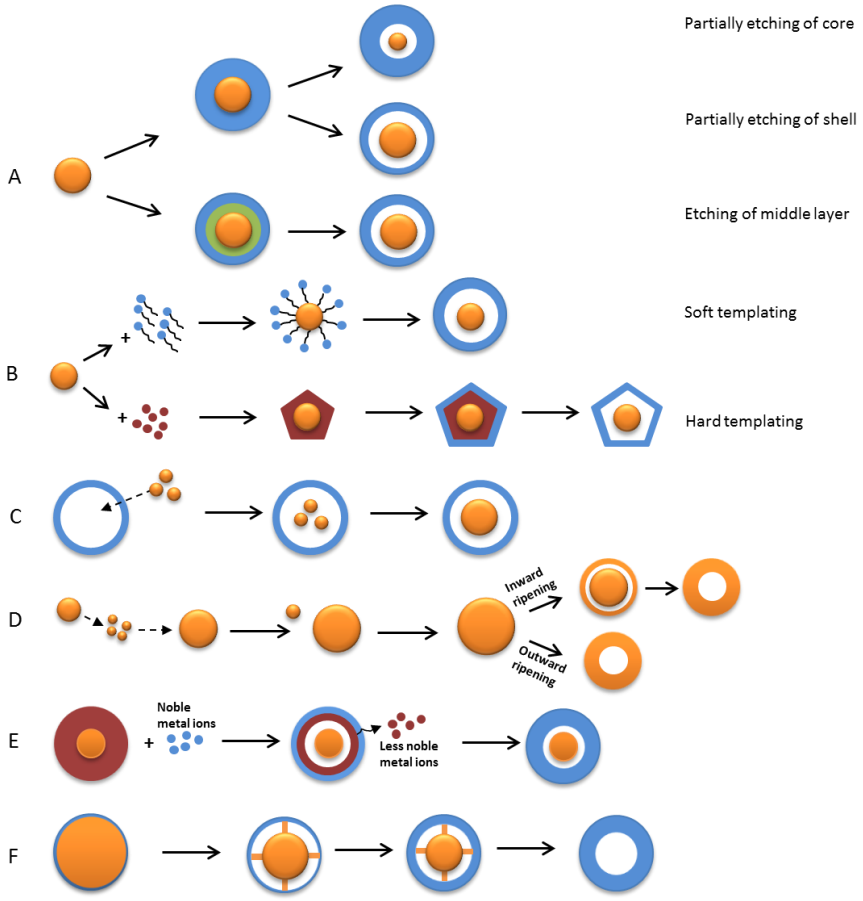

Figure 2.2**:** Simple diagrams of general synthetic methods: (A). selective etching method; (B). soft- and hard-templating methods; (C). ship-in-a-bottle method; (D). Ostwald ripening method; (E). galvanic replacement method; and (F). Kirkendall diffusion method.

Selective etching uses chemicals or calcination to selectively remove either part of the shell or part of the core to create a void between the core and the shell, as shown in Figure 2.2(A). There are three types of selective etching method: partial etching, surface-protected etching, and shell formation via chemical reactions (3). The first method, partial etching, is one of the commonest fabrication routes because of its simplicity. Generally, a void is created by introducing a certain amount of an acidic or basic etchant (such as HF or NaOH) to partially etch out core or shell material. The core size and shell thickness can be tuned by adjusting the amount of etchant used. The second method, surface-protected etching, was first developed in 2007 (3). Many researchers have stated that this strategy was a significant breakthrough in synthesizing porous silica nanoparticles. For sol–gel-derived silica nanoparticles, the dense silica layer makes it difficult for outside molecules to reach the inner active core; surface-protected etching overcomes this drawback (35). In this method, the surfaces of metal oxide (such as silica) particles are coated with a protecting layer such as poly(vinylpyrrolidone) (35) and 3-thiocyanatopropyltriethoxysilane (36)) and then an appropriate etchant is introduced to etch away part of the metal oxide from the interior and create a porous shell structure at the same time. This protecting layer enables the metal oxide nanoparticles to retain their original size, while creating voids (35). In the third selective etching method, formation of the shell material through chemical reactions between core and shell materials is a spontaneous self-formation method. First, a core (pure metal or metal oxide) coated with a shell (pure metal or metal oxide) in a core–shell structure is prepared. Selective etching occurs when the shell reacts with the core to create a void between the core and shell. This synthetic method is not popular because it is only suitable for a limited number of nanoparticle compositions.

Soft templating is a flexible, simple, and effective method, especially for the fabrication of functional YSNs with porous shells (20). Soft templates are surfactants and polymers which possess a hydrophilic head and hydrophobic chain (15). When noble metal cores are evenly dispersed in a soft template mixture, the soft templates spontaneously attach to the cores to give well-defined assemblies under certain conditions to form core–shell nanoparticles. Hydrolysis and condensation of the core–shell nanoparticles remove the hydrophobic chains and form a space between

the core and the shell. YSNs are obtained by calcination to produce a porous shell, as shown in Figure 2.2(B) (15).

Hard templating is performed similarly to soft templating, but hard templates instead of soft templates spontaneously attach to the core material. The hard-templating method performs well in the synthesis of rigid YSNs with a movable core encapsulated in a hollow metal oxide shell (15). A pre-synthesized metal core is coated with a hard template and then the desired shell material attaches to the hard template layer to form sandwich-structured core–shell nanoparticles. Finally, an etchant is introduced to remove the hard template and create a void between the shell and the core.

Ship-in-bottle method involves entrapment of molecules in nanocapsules; the method is the reverse of the usual YSN methods such as selective etching or soft templating (22). In this synthesis route, a porous hollow nanoshell or nanocage is prepared first. Core precursors/molecules then enter the shell through channels in the porous shell. The core precursors/molecules then assemble to form single or multiple cores inside the hollow chamber, as shown in Figure 2.2(C).

Ostwald ripening is a physical recrystallization process and does not involve any chemical reaction. According to the International Union of Pure and Applied Chemistry, Ostwald ripening is "the growth of larger crystals from those of smaller sized ones which have a higher solubility" (3, 37, 38). Recently, a new Ostwald ripening mechanism was developed. It can be described as an oriented attachment process in which small crystals attach to each other in the correct orientation to form bigger crystals (39). This new method has been used in many research studies. The Ostwald ripening method is a thermodynamically favourable and spontaneous template-free strategy for creating yolk–shell or hollow nanoparticles (40). Unstable and less dense smaller nanocrystals with higher solubilities have a strong tendency to dissolve and redeposit on the surface through a recrystallization process, which leaves a hollow interior space, as shown in Figure 2.2(D) (40, 41). The formation of YSNs is driven by the differences among the chemical potentials of the crystallites (3, 42).

Galvanic replacement, which is a sacrificial template strategy, is an efficient and easy route for synthesizing YSNs with controllable morphologies, particularly controlled compositions and porosities (3, 43, 44). Many researchers consider galvanic replacement to be the most versatile synthetic method. The mechanism of galvanic replacement is based on a redox chemical reaction in which the metal from a metal salt is exchanged with metal ions from solution because of their different electrochemical potentials, as shown in Figure 2.2(E). The less noble metal from the metal salt nanoparticle is the sacrificial template and acts as a reducing agent; it is concurrently replaced by a more noble metal ion from the solution to achieve electrochemical potential equilibrium (45, 46). Galvanic replacement involves deposition of a more noble metal, alloying, and dissolution of a less noble metal. Dissolution of the less noble metal forms pinholes, which result in voids, and these expand towards the centre (44).

Kirkendall diffusion is another ion-exchange nanoparticle synthesis method after galvanic replacement and also a crystal growth synthesis method besides Ostwald ripening (37, 42). Kirkendall mass transfer occurs at the boundary of two different metals when an imbalance in their diffusion rates occurs, leaving vacancies at the material side with the faster diffusion rate (47). In YSN synthesis based on Kirkendall diffusion, a core–shell nanoparticle consisting of two different core and shell materials (metal or alloy) is first prepared. Usually, the core material is the sacrificial template and has a faster diffusion rate than the shell material. Voids are formed at the core/shell interface via thermal activation (Figure. 2.2(F)) (44). Further diffusion leads to formation of a hollow nanoparticle structure.

2.2.2 Comparison and analysis of general synthesis methods

Table 2.1: Comparison of common YSN synthesis methods

Synthesis method	Suitable composites	Nanoparticle structure	Complexity	Disadvantages	References
Selective etching	Most types of materials	Spherical and non-spherical	Moderate	Amount of etchant used	(3, 35)
Soft templating	Inorganic materials	Spherical	Simple	Uniformity; appropriate surfactants	(3, 15, 29)
Hard templating	Metals and metal oxides	Spherical	Simple	Rigid shape particles only; costly	(15, 29, 48, 49)
Ship-in-bottle	Most types of materials	Spherical	Moderate	Shell needs to be prepared first.	(3, 22)
Ostwald ripening	Inorganic oxides or sulphide semiconducting materials	Complex	Moderate	Controlling of void space	(3, 42)
Galvanic replacement	Noble metals and metal oxides	Various shapes and structures	Moderate	Time consuming; breakup of nanostructure	(3, 44, 46, 50)
Kirkendall effect	Metals and alloys	Complex	Moderate	Untuneable	(3, 37, 44)

Selective etching is one of the most popular methods for YSN fabrication and is suitable for synthesizing an extensive range of materials, especially silica- and carbon-based nanoparticles. Among selective etching approaches, surface-protected strategies are commonly used for fabricating hollow and non-spherical structures. Fine tuning the amount of etchants and surfactants enables control of the nanoparticle size and shell thickness. However, this is one of the main drawbacks of this method because the appropriate amounts of etchants and surfactants need to be determined by trial and error. The low uniformity of the nanoparticle size is another weakness. Selective etching is therefore not recommended for producing high-quality YSNs with a narrow size distribution. These problems can be solved by using a combination of selective etching and other synthetic methods.

Here, we briefly introduce some examples to elaborate the selective etching steps. One-component YSNs, namely silica@mesoporous silica (SiO2@m-SiO2), with

dense silica nanospherical cores were first prepared using the Stöber method. A sol–gel method with pore-forming agents was used to coat the silica nanospheres with a mesoporous silica layer to form a core–shell structure (51). The absence and presence of surfactants in silica core and mesoporous silica shell, respectively, resulted in structural differences, thus etchant (such as Na_2CO_3 or ammonia solutions) could selectively etch part of core material away to form void between core and shell. Afterwards, surfactants were removed through high temperature treatment (51). Two-component YSNs, Au@m-SiO_2, were prepared as follows. Au nanoparticles were prepared by traditional sodium citrate reduction and then the metal spheres were coated with a layer of dense silica via a sol–gel method. A mesoporous silica shell was deposited outside the dense silica layer to form a Au@SiO_2@m-SiO_2 core–shell structure (51). A Au@m-SiO_2 yolk–shell structure was created by introducing an etchant to etch away the dense silica layer. Three-component YSNs, Fe_3O_4@SiO_2@TiO_2, were synthesized using a surface-protected selective etching method. Each Fe_3O_4 sphere was coated with a layer of silica, followed by a layer of resorcinol–formaldehyde resin (RF), and an outer layer of amorphous TiO_2, using sol–gel processes, to form a FeO_4@SiO_2@RF@TiO_2 core–shell structure (52). The core–shell nanoparticles then underwent two-step annealing treatment. During the first calcination under nitrogen, a carbon layer was formed, which protected the precrystallized TiO_2 shell from morphological changes. A yolk–shell structure was created by removing the carbon layer through calcination in air (52).

Soft-templating methods overcome many of the difficulties associated with selective etching, such as multiple steps and the need for accurate amount of etchants. Soft templates such as surfactants, polymers, and viruses can be easily removed via simple processes such as washing and calcination, without using chemicals, in contrast to hard templates. Soft templating is therefore the perfect option for one-pot synthetic strategies (15, 29). For example, using FC_4 surfactant as soft template created encapsulated lipase within mesoporous silica YSNs; or resins attached on core produce mesoporous carbon shell (49, 53). The difficulties of soft-templating method are the trouble in controlling the uniformity of products and also the challenges of choosing appropriate surfactants (3, 15).

Hard-templating method performs well in the fabrication of rigid YSNs. Silica is a common hard template and is widely used to create noble metal@metal oxide YSNs.

Hard templating is easily controlled, and the results are easy to predict and highly reproducible (48). However, this synthetic method is not as popular as the soft-templating method used in industry because the range of particle shapes that can be obtained is limited and it is expensive, which makes it unsuitable for large-scale production. For example, mesoporous carbon nanoparticle synthesis using mesoporous silica as a hard template is not a feasible option, and soft templating is used instead (49). However, hard-templating methods can be used for small-scale preparation of nanoparticles such as metal cores encapsulated in TiO_2 shells (54, 55) and multi-shell Au/CeO_2 hollow spheres (48). Moreover, soft and hard templating methods so far have only been used for producing spherical nanoparticles.

Ship-in-bottle method can be used to create YSNs with a single core, multiple cores, or multiple shells and can be used for most types of material. As previously mentioned, the ship-in-a-bottle method is the reverse of other general synthetic approaches. It is therefore useful for producing highly inert materials which are difficult to dissolve and remove, such as zeolites (56). The ship-in-a-bottle route is therefore an efficient, economical, and controllable method for synthesizing yolk–shell-nanostructured nanoparticles (22). For example, fabrication of yolk–shell HPW@Hollow silicalite-1 has been reported(57).

Ostwald ripening is a template-free synthetic strategy and is a well-known method for generating nanoparticles with complex structures. This method is widely used to fabricate YSNs in inorganic oxide or sulfide semiconducting materials, e.g. TiO_2–YSNs (58), Pt@CeO_2 core-shell or YSNs (59), Au@SiO_2 (39) and ZnS core-shell nanoparticles (60). As mentioned above, Ostwald ripening is a spontaneous process, and although the void size can be controlled by varying the hydrothermal reaction time, precise tuning of the void size is still a major challenge in this fabrication process.

Galvanic replacement method is used for metal and metal oxide YSN fabrication. Au, Pt, and Pd salts are the most common noble metal compounds, and Ag, Ni, Al, and Cu are used as sacrificial templates in galvanic replacement processes (44, 61). The greatest advantage of this fabrication method is the ability to control the nanoparticle size and shape, and it is one of the most versatile synthetic methods for creating metal nanoparticles with complex structures. Morphological control greatly depends on the shapes and sizes of the template nanoparticles and the reaction conditions. In

addition, chemicals such as HCl can be added to the solution to regulate the reaction kinetics to increase the morphological control (44). However, this strategy also has drawbacks such as long reaction times and breakage of the nanostructure by dealloying, which tends to occur in the final stage of fabrication when the less noble metal redissolves from the shell material (44).

Kirkendall diffusion has attracted significant attention because of its frequent occurrence and the possibility of obtaining nanoparticles with unique compositions and complex structures (44). Similarly to the galvanic replacement method, this synthetic method is suitable for metal and alloy materials, and the formation process is thermodynamically favourable (37). The use of this method for fabricating YSNs is not yet well understood. It is believed that the yolk/core is initially connected to the shell by many filaments, as shown in Figure 2.2(F), and the filaments break before the yolk/core completely disappears through diffusion. Because of the uncertainty and uncontrollability of the Kirkendall diffusion process, tuning the YSN morphology is a challenge.

The use of YSNs is growing rapidly, and there is increasing demand for yolk–shell nanoreactors with more complex structures which can be precisely tuned. Much research is therefore being devoted to investigating new and more advanced methods for YSN synthesis. Here, we briefly introduce one newly developed synthetic route that has good potential for synthesizing multicomponent core–shell or yolk–shell colloidal hybrid nanoparticles. The seed-mediated growth method was first used to synthesize noble metal nanocrystals; it is based on the galvanic replacement and selective etching methods. The seed, i.e. the less noble metal salt, serves as a sacrificial template, which is replaced by ions of a more noble metal in the introduced solution. Seed-mediated growth, which is similar to galvanic replacement, takes advantage of the fact that the activation energy of the metal reduction reaction between a less noble metal and more noble metal is lower than that of nucleation of the seeds themselves (62). In addition, because the spontaneous nucleation of seeds is less favourable, natural and uneven crystal growth can be successfully suppressed; this is also the reason for the controllability of the nanoparticle shape and size (62). Recently, this synthetic route has been successfully used to fabricate noble metal YSNs such as Ag@h–SiO_2 YSNs (63), and the research focus has moved to synthesizing non-noble metal cores encapsulated in porous silica shells, e.g.

Ni@SiO_2 YSNs (64). Ni, which is one of the most effective catalysts, gives good catalytic performances in many significant reactions. The growth of non-noble metals is much more difficult to restrict than is seed growth of noble metals. This problem can be overcome by using a more powerful seed to restrict Ni growth within the porous shell. As shown in Figure 2.3, Pd was used as an effective catalyst for decomposition of Ni^{2+}–hydrazine complex (64). Pd^{2+} ions were introduced onto Fe_3O_4 together with Au to form a stronger seed. After creation of the Au and Pd seed, Ni^{2+}–$(N_2H_4)_n$ was added as a reducing agent and Au and Pd were replaced by Ni to form Ni@SiO_2 YSNs.

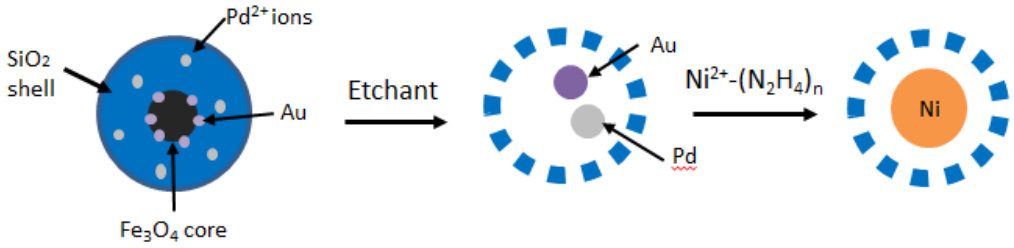

Figure 2.3: Synthesis of Ni@SiO_2 through seed-mediated growth method.

2.3 Advanced yolk-shell nanoreactors for energy conversion applications

Rapid advances in nanotechnology have led the chemical industry to a new peak. There have been enormous changes and improvements in the quality and quantity of chemical production compared with two decades ago. People therefore ask "What is the next move?" Of course, the next move will always be process optimization. Chemical processes involving renewable energy or low energy consumption, which have the potential to solve resource or environmental problems, always catch the world's attention. Catalysis of chemical reactions has become a key element in research.

The use of YSNs as nanoreactors for catalytic reactions has attracted much interest and become one of the hottest research topics. YSNs definitely have greater potential for use in long-lasting and low-cost catalytic processes than metal nanoparticles and core–shell nanoparticles, which also overcome many of the severe drawbacks of traditional catalysts. First, functionalization of both the core and the shell of YSNs can be achieved by attaching functional groups to the core and shell or by fabricating

the core and shell from appropriate materials. Because of the differences between the physical and chemical properties of the yolk and shell, multiple catalytic reactions can be performed simultaneously. Second, the encapsulated core or cores with active sites can move freely inside the shell, which allows reactants to reach the active sites more easily, and this improves the catalytic activity. Next, the voids between the yolk and shell provide a homogeneous reaction environment for reactants, which minimizes environmental effects in catalytic reactions. It is well known that homogeneous catalysis gives better results than heterogeneous catalysis (65). YSNs with various shapes, sizes, and structures can be easily produced using the numerous excellent synthetic methods described in the synthesis section. The shapes, sizes, and structures are important factors in the catalytic performance; this is why a large amount of research has been devoted to the development of synthetic methods. There is no "one size fits all" case in catalysis; therefore the fabrication of catalysts with the most appropriate features for achieving the best performances is crucial. Finally, the most important function of yolk–shell nanostructures is to avoid aggregation and deactivation of the active cores. Dispersed nano active cores, especially pure metal cores, tend to aggregate and lose their catalytic activity during exposure to chemicals, products, or by-products under experimental conditions. The YSN shell therefore acts as a protecting layer that efficiently prevents damage and allows transport of reactants and products from active sites.

Because of the many advantages of YSNs as catalysts for chemical reactions, any research conducted on this topic could lead to a scientific breakthrough. In the following subsections, we summarize a few important and advanced yolk–shell catalyst applications such as methane reforming, photocatalysis, and electrocatalysis. These reactions play significant roles in the current chemical industry and contribute greatly to green energy and chemical production.

As a result of the extensive advantages of YSNs as a nanocatalyst for chemical reactions, it is faithfully believed that any research work conducted on this topic could be a scientific breakthrough. In the following subsections, we would like to summarize a few important and advanced yolk-shell nanocatalysts applications, such as methane reforming, photocatalysis, and electrocatalysis. These reactions are playing significant roles in current chemical industry and contribute greatly for green energy and chemical productions.

2.3.1 Utilization of carbon sources – methane reforming

Clean and efficient energy generation is very much sought in our current environmental situation. Converting one of the major Greenhouse Gas – methane into clean syngas/hydrogen gas is a sensational development in generating sustainable energy. Hydrogen gas combustion has become another important way to produce energy, and it is also an important chemical for petroleum refining process. Presently, there are a number of hydrogen production processes available, such as steam reforming of methane (SRM), CO_2 (dry) reforming of methane (DRM), partial oxidation of methane (POM), bi-reforming of methane, autothermal reforming of methane and tri-reforming of methane (66). Among all, SRM, DRM and POM are more popularly employed than others. Hydrogen production from natural sources is a good start to decrease or even eliminate usage of traditional fuels (diesel and coke). In regard to catalysts used in methane reforming reaction, Ni has always been the favourite metal catalyst since the early stage. Rh, Ru and Pt are also proven to be very sufficient catalysts, however they are rare and expensive (67-69). Due to the availability, ease of preparation and low cost, Ni and Co are the favoured catalysts used in methane reforming industry (67, 69-71). As known, Ni nanoparticle is air-sensitive and gets deactivated during methane reforming reaction due to carbon deposition on the surface of the catalyst over a period of time (66, 69, 70, 72-74). Therefore, core-shell and yolk-shell nanostructured catalysts were introduced into methane reforming reaction to prevent carbon deposition on metal nanoparticles and also agglomeration. It is believed that protection shell can efficiently block carbon deposition on the edge and corner of active metal nanoparticles (75). Here, we briefly introduce some core-shell structured nanocatalysts and concentrate more on YSNs that were applied in SRM, DRM and POM hydrogen production processes.

Steam reforming of methane (SRM) is the most significant and well-developed hydrogen production method that produces the major amount of the total hydrogen gas production in the current years (66, 76). Syngas (mixture of carbon monoxide and hydrogen gas) is the product of steam reforming of methane reaction as shown in Equation 2.1(1), and water-gas shift reaction (Equation 2.1(2)) can enhance yield of hydrogen gas generation in the final product. SRM reaction is a highly endothermic chemical process which requires large amount of energy input to operate at temperatures between 675 and 1000 °C and highly pressurized condition, such

environment makes many materials unsuitable as a support for active metal catalysts (66, 70, 76). Moreover, in order to prevent carbon deposition which could cause deactivation of metal catalysts, the water/methane ratio of reactants input should be high (over 1:1), which is also required for water-gas shift reaction (66, 70, 74).

Equation 2.1: (1) SRM reaction equation; (2) water-gas shift reaction equation.

$$CH_4 + H_2O \rightarrow CO + 3H_2 \quad \Delta H^{o}_{298} = +206 KJ.mol^{-1} \quad (1)$$

$$CO + H_2O \rightarrow CO_2 + H_2 \quad \Delta H^{0}_{298} = -41 KJ.mol^{-1} \quad (2)$$

Core-shell nanoparticles were firstly used in SRM process before YSNs. $Ni_{core}@SiO_2$ (11 wt% nickel) were synthesized by a deposition-precipitation method, and achieved an approximate 85% of methane conversion at 750 ^{0}C with inlet water/methane ratio 3:1 for the first 4 hour (66). Moreover, core-shell nanoparticles consisting of Ni core and Al_2O_3 shell - $Ni_{core}@Al_2O_3$ (10 wt% nickel) were also prepared under multibubble sonoluminescence condition, and the best result of $Ni_{core}@Al_2O_3$ nanocatalysts was as high as 97% methane conversion at 750 °C with water/methane ratio 2 for reaction time up to 5 hours (74).

In further modifications of the catalysts, yolk–shell-structured $Ni@SiO_2$ catalysts were prepared by directly coating a Ni core with a silica shell, followed by selective etching of the core, and porous shell formation by calcination (72). SRM was performed using $Ni@SiO_2$ (89 wt% Ni) as a catalyst in a fixed-bed continuous-flow reactor at atmospheric pressure and 700 °C. A high water/methane ratio was used in the inlet to minimize the possibility of carbon deposition. The methane conversion and H_2 concentration were high, above 90% and 70%, respectively, for a reaction period up to 4 h. The experimental results were close to the theoretical values, and the catalytic activity of the recycled catalyst was almost the same as that of the fresh catalyst (72). Steam reforming experiments were also performed using yolk–shell catalysts with various metal weight percentages under the same experimental conditions. The metal weight percentage in the catalyst did not greatly affect the methane conversion or H_2 concentration. For example, with 20 wt% Ni in the catalyst, the methane conversion and H_2 concentration were 85% and 70%, respectively (72).

A $Ni@ZrO_2$ yolk–shell catalyst was synthesized using a double-template emulsion method by coating silica and ZrO_2 shells sequentially on Ni nanoparticles, followed by silica etching to form a yolk–shell structure (70). Very small Ni cores were synthesized using a reverse micelle approach, which is believed to facilitate particle dispersion, increase the number of active catalytic sites, and prevent coke formation (70). The catalytic ability of $Ni@ZrO_2$ (5.08% Ni) yolk–shell particles was tested using a fixed-bed quartz reactor at 750 °C, atmospheric pressure, and a steam/methane input ratio of 2.5. The results showed high catalytic activity, giving 93% methane conversion, and the activity was retained for 150 h, as shown in Figure 2.4.

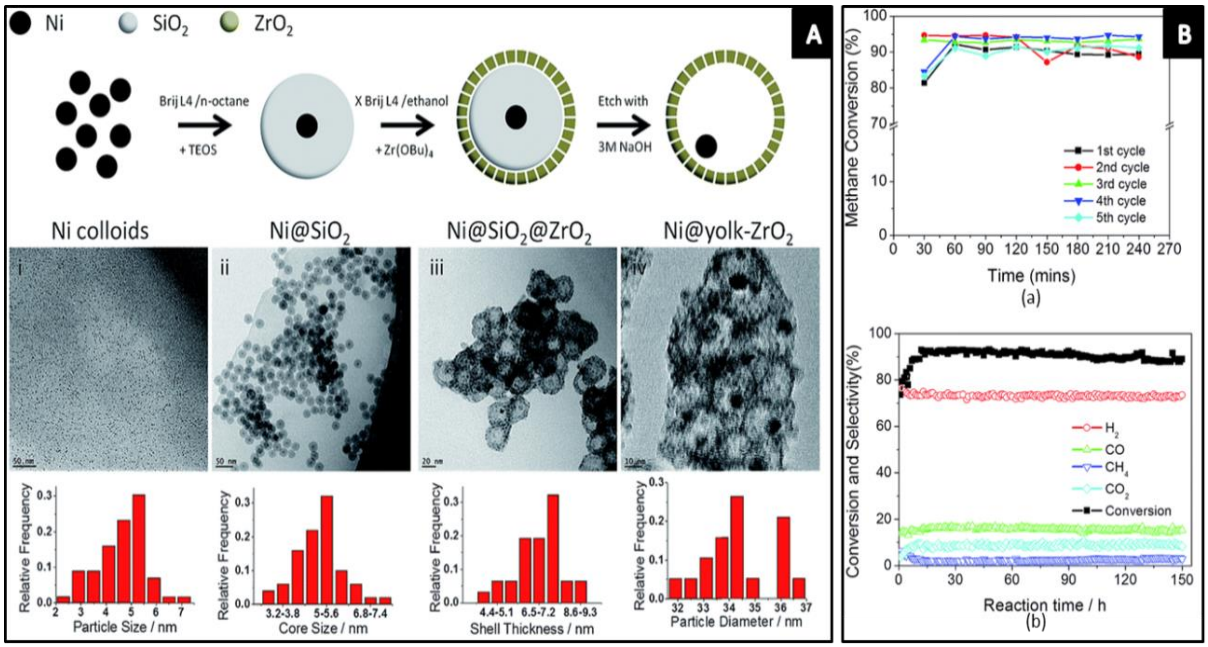

Figure 2.4: A. Schematic diagram of synthesis of $Ni@ZrO_2$ yolk-shell nanoparticle, and TEM images and core-size distributions at each synthesized step; B. (a) Recyclability and (b) durability tests of $Ni@ZrO_2$ yolk-shell nanoparticles on steam reforming of methane. (panels A and B reproduced with permission from ref. (70). Copyright © The Royal Society of Chemistry 2015)

The catalytic performances of the core–shell and yolk–shell nanoreactors mentioned above in SRM were compared. The results (Table 2.2) show that $Ni@ZrO_2$ is the best catalyst because it gives good methane conversion, has a low metal weight percentage, good stability and recyclability, and is easily synthesized.

Dry reforming of methane (DRM) is an important process because it converts two major greenhouse gases (methane and CO_2) to a useful product, i.e. syngas, as shown in Equation 2.2. Similar to SRM, DRM is also a highly endothermic reaction, which requires a high operating temperature. Initially, DRM was not investigated as intensively as SRM because of its low H_2/CO ratio (1/1); a low H_2 gas ratio in the final product is undesirable and coke formation becomes problematic in the absence of steam (77). However, this product ratio is appropriate for producing synthetic fuel via Fischer–Tropsch synthesis; therefore DRM has recently become a popular research topic (69, 77, 78).

Equation 2.2: DRM reaction equation.

$$CH_4 + CO_2 \rightarrow 2CO + 2H_2 \quad \Delta H^{o}_{298} = +247 KJ.mol^{-1}$$

$Ni_{core}@Al_2O_3$ core–shell nanoparticles also gave excellent performances in DRM, giving 92% methane conversion and 95% CO_2 conversion at 800 °C for up to 150 h, with a CH_4/CO_2 input ratio of 1. $Ni_{core}@MgO–Al_2O_3$ core–shell nanoparticles gave similar catalytic result under the same test conditions (79). $LaNiO_{3core}@SiO_2$ (10 wt%) core–shell nanoparticles were also tested in DRM in a coaxial dielectric barrier discharge plasma reactor under ambient conditions. The catalytic performance was better than that of traditional $Ni_{core}@SiO_2$, with CH_4 and CO_2 conversions of 88% and 78%, respectively (78). As well as conventional spherical nanoparticles, Ni–Mg phyllosilicate nanotubes@silica (Ni–Mg PSNTS@SiO_2) core–shell nanoreactors were recently synthesized, and gave 85% CH_4 conversion and 89% CO_2 conversion at 750 °C; the nanoparticles were stable for 72 h (71).

Yolk–shell catalysts with a yolk–satellite–shell structure (Figure 2.1(C)), i.e. Ni–yolk@Ni@SiO_2 nanoparticles, have been synthesized by selective etching via calcination and reduction (80). These nanoparticles consisting of a Ni yolk and satellite encapsulated within a silica shell had high stabilities and catalytic activities in CO_2 (dry) reforming of methane; the performances of Ni–yolk@Ni@SiO_2 were highly dependent on the silica shell thickness (80). When the silica shell thickness was 11.2 nm or more, the core–shell Ni@SiO_2 structure was converted to a yolk–satellite–shell nanocomposite, i.e. Ni–yolk@Ni@SiO_2, by calcination at 800 °C for 2 h (80). A series of experiments were performed using Ni–yolk@Ni@SiO_2

nanoreactors with various shell thicknesses as catalysts in DRM. The results show that the nanoreactor catalytic activity, stability, and carbon resistance increased with increasing shell thickness, and those small Ni satellites around the Ni core improved the catalytic activity. At the optimum shell thickness, i.e. 11.2 nm, Ni–yolk@Ni@SiO_2 gave 90% CH_4 conversion and 95% CO_2 conversion for up to 90 h without any carbon deposition.

Ni@SiO_2 yolk–shell nanoreactors, which were fabricated using the synthetic method reported by Song and his colleagues (72), (summarized in the discussion of SRM), were also tested in DRM. The DRM catalytic activity of Ni@SiO_2 YSNs of core size approximately 46.4 nm was low compared with their high activity in SRM. Because of the reverse waster-gas shift reaction, the CH_4 conversion (43.9%) was lower than the CO_2 conversion (57.3%) at 700 °C; it is suggested that water supplied by the reaction helps to stabilize the catalyst and prevent carbon deposition (81). However, despite the catalytic activity, Ni@SiO_2 showed excellent durability up to 590 h at both 700 and 800 °C and the conversions of CH_4 and CO_2 increased with increasing operating temperature because the DRM is endothermic, but the gas hourly space velocity of the reactants was unchanged (81).

Bimetallic mesoporous shell NiCe@m-SiO_2 yolk–shell catalysts synthesized by encapsulating CeO_2- modified Ni nanoparticles (less than 10 wt% Ce), formed in situ, in mesoporous silica shells significantly improved the dispersion of Ni nanoparticles, catalytic performance, and suppression of coke formation (69). DRM was performed in a fixed-bed reactor with a quartz tube and a reactant input ratio of 1:1. The CH_4 conversion reached 97.6% at 800 °C and 95.2% at 750 °C, and the conversion was unchanged after 40 h, as shown in Figure 2.5 (69). In DRM, CH_4 conversion is lower than CO_2 conversion because of the reverse water-gas shift reaction, and the catalytic performance increases with increasing reaction temperature. Table 2.2 summarizes the performances of the core–shell and yolk–shell catalysts used in DRM. Current research on DRM is progressing rapidly, and it is believed that more efficient and well-designed nanoreactors will be available in the near future.

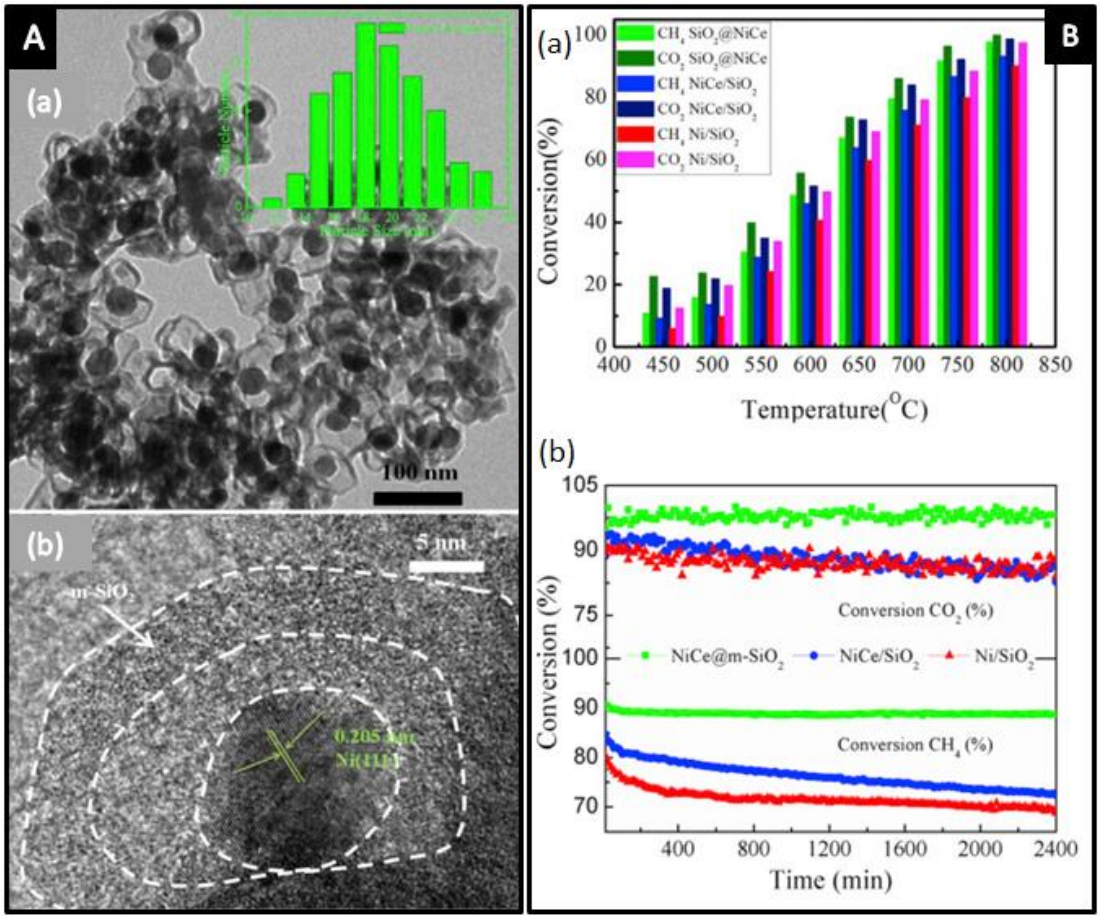

Figure 2.5: A. (a) TEM image of NiCe@m-SiO_2 YSNs and the inset is the size distribution of Ni nanoparticles, (b) HRTEM image of NiCe@m-SiO_2 YSNs; B. (a) CH_4 and CO_2 conversions catalysed by different catalysts at various temperatures, (b) catalytic stability of different catalysts. (panels A and B reproduced with permission from ref. (69). Copyright © 2015, Hydrogen Energy Publications)

Partial oxidation of methane (POM), also called oxy-methane reforming, mainly produces syngas (H_2 + CO). POM has some advantages over traditional SRM and DRM. POM produces syngas, which is desirable in green energy production, with a H_2/CO ratio of 2, and the reaction ($CH_4 + 1/2CO_2 \rightarrow CO + 2H_2$: $\Delta H_{298}^{o} = -37$ kJ mol^{-1}) is slightly exothermic and therefore needs less energy. The operating costs for POM are therefore lower than those for SRM and DRM (73, 82). The first catalysts developed for POM, consisting of Ni metal on an Al_2O_3 support, gave very high methane conversions and syngas selectivities, but severe sintering and aggregation of the catalysts occurred during the reaction (73). Nanoparticles consisting of a Ni core encapsulated in an Al_2O_3 shell were synthesized. $Ni_{core}@Al_2O_3$ (10 wt%) core–shell

nanoparticles gave an excellent catalytic performance in POM, with a methane conversion of 96% (83). Nanoparticles consisting of a Ni core encapsulated in a porous silica shell were also tested in POM. This nanocomposite has a high activity and long lifetime, especially at high temperatures. A Ni-350@meso-SiO_2 core–shell catalyst prepared using a modified Stöber method gave a maximum methane conversion of approximately 93% with 92% CO selectivity and 87% H_2 selectivity (73).]. The catalytic performance was tested in a continuous-flow fixed-bed reactor at atmospheric pressure and 750 °C for 500 min. The results show that the selectivity for H_2 was only slightly lower than that for CO. The catalytic activity was highly dependent on the size of the Ni core and an increase in the core size resulted in a significant decrease in methane conversion and selectivities for CO and H_2 (73). The same research team doped Ni@SiO_2 core–shell nanoreactors with various metals. The results show that La-doped Ni@SiO_2 particles (0.1 La–Ni@SiO_2) gave the best performance in terms of catalytic ability and durability by decreasing carbon deposition (84). Recently, Ni/ZrO_2@SiO_2 (24.8 wt% Ni, Ni/Zr = 1) core–shell nanoparticles synthesized using a modified Stöber method were tested in POM. A methane conversion of 99% was achieved at 750 °C (75). To the best of our knowledge, there has not been any yolk-shell structured nanocatalyst applied in POM reaction. The catalytic performances of all mentioned core-shell nanocatalysts are listed in Table 2.2.

Table 2.2: Summary of the catalytic performance of nanoreactors applied in Stream reforming of methane, dry reforming of methane and partial oxidation of methane applications.

Application	Catalyst			Performance			Ref
	Particle name	Structure*	Ni(Wt%)	Operating temperature	CH_4 conversion	Tested durability (hour)	
Steam reforming of methane $CH_4 + H_2O \rightarrow CO + 3H_2$ $\Delta H^o_{298} = +206KJ/mol$ $CO + H_2O \rightarrow CO_2 + H_2$ $\Delta H^o_{298} = -41KJ/mol$	**$Ni_{core}@SiO_2$**	CS	11%	1023K	85%	4	(66)
	$Ni_{core}@Al_2O_3$	CS	10%	1023K	97%	5	(74)
	$Ni@SiO_2$	YS	89%	973K	90%	4	(72)
	$Ni@ZrO_2$	YS	5.08%	1023K	93%	150	(70)
Dry reforming of methane $CH_4 + CO_2 \rightarrow 2CO + 2H_2$ $\Delta H^o_{298} = +247KJ/mol$	**$Ni_{core}@Al_2O_3$**	CS	11%	1073K	92%	150	(79)
	$LaNiO_{3core}@SiO_2$	CS	10%	NA	88.3%	30	(78)
	Ni-Mg PSNTS@SiO_2	CS	11.6%	1023K	85%	72	(71)
	Ni-yolk@Ni@SiO_2	YS	18.6%	1073K	90%	90	(80)
	$Ni@SiO_2$	YS	42.4%	973K	43.9%	590	(81)
	NiCe@m-SiO_2	YS	10.6%	1023K	95.2%	40	(69)
Partial oxidation of methane $CH_4 + \frac{1}{2}O_2 \rightarrow CO + 2H_2$ $\Delta H^o_{298} = -37KJ/mol$	**$Ni_{core}@Al_2O_3$**	CS	10%	1073K	96%	50	(83)
	Ni-350@meso-SiO2	CS	43% (calculated)	1023K	93%	8.3	(73)
	0.1 La-Ni@SiO_2	CS	43% (calculated)	973K 1023K	85.2% 96.1%	64	(84)
	Ni/ZrO2@SiO_2	CS	24.8%	1023K	99%	160	(75)

*CS: Core-shell; YS: Yolk-shell

2.3.2 Photocatalysis

Photocatalysis can be defined as the acceleration of chemical reactions by light energy. It has been widely researched for decades because it is a green process. Photocatalytic reactions can be classified as up-hill or down-hill; up-hill reactions convert light to chemical energy, e.g. photosynthesis in plants, whereas down-hill reactions convert reactants to products via light absorption (85). Artificial up-hill reactions are currently of great interest. Photocatalysis is attractive and important in many applications such as organic pollutant degradation, selective organic transformations, killing cancer cells, water splitting, reduction of CO_2, and biomass conversion (59, 86). Among these applications, research is currently focused on water splitting, reduction of CO_2, and organic pollutant degradation. As mentioned in the section on methane reforming, there is a great demand for sustainable energy production. Photocatalysis can make an important contribution to green energy generation; it has the advantages of eliminating harsh reaction conditions and increasing reaction rates via visible-light absorption (59, 87). Abundant data are available because photocatalysis has been extensively researched for many decades. Here, we summarize current progress in research on core–shell materials and YSNs as catalysts for water splitting, reduction of CO_2, and organic pollutant degradation; the catalytic performances of all the nanoreactors discussed are listed in Table 2.3.

Water splitting reaction, which converts water to clean fuels, i.e. H_2 and O_2, using solar energy, is the most attractive photocatalytic reaction. Traditionally, H_2 has been obtained from seawater by chemical electrolysis. This method is not widely used for large-scale production of H_2 because of the very high operating costs (88). The use of photocatalysis could overcome this problem and enable the development of low-cost and efficient methods for H_2 gas generation. In photocatalytic water splitting, electrons in conduction bands and holes in valence bands split water molecules into oxygen and hydrogen; the electrons and holes are created by ionization of photocatalysts through exposure to light (Figure 2.6A) (89). Since the 1970s, when Fujishima and Honda first reported the use of TiO_2 as a catalyst for water splitting, much research has been conducted on developing appropriate photocatalytic systems for producing chemical energy through water splitting (85, 90, 91).

Many materials such as noble metals, metal oxide semiconductors, nitrides, oxynitrides, and oxysulfides have been investigated as potential catalysts (92, 93). Among all the tested photocatalysts, semiconductors are the most suitable because they have appropriate bandgaps, low electrical resistance, are cheap, and can be produced on a large scale A semiconductor of small particle size was first used for water splitting, but the particles recombined via the charges created by light absorption, causing a decrease in the surface area and efficiency (94). Photocatalytic water splitting consists of two half reactions: water oxidation to O_2 and water reduction to H_2 (92, 95); specific catalysts are needed for each half reaction. Advanced-structured and composite nanoreactors have been designed, synthesized, and tested for water splitting. Noble metal and transition metal oxides are often used as cocatalysts in nanoreactors with advanced structures (92, 96). These advanced nanoreactors increase the conversion rate and prevent recombination of the products (H_2 and O_2) to water molecules. The performances of TiO_2 and ZnO are better than those of other semiconductors (88, 90, 93). TiO_2 can only be excited by UV light because of high recombination of photogenerated electron–hole pairs and a wide band gap; this results in inefficient use of visible light. However, this drawback can be overcome by either encapsulating a noble metal core within a TiO_2 shell or heavy doping with carbon and nitrogen (58, 59, 89, 93, 97). The production of H_2 gas by water splitting using a semiconductor as a heterogeneous photocatalyst is a more attractive technique for H_2 gas generation than methods such as partial oxidation, gasification, and steam reforming (87, 88). Core–shell-nanostructured photocatalysts, e.g. $NiFe_2O_4$@TiO_2 (89), SiO_{2core}@Ta_3N_5 with Pt nanoparticles loaded on the inner shell and IrO_2 or CoO_x loaded on the outer shell (92) and $SrTiO_{3core}$:La/Rh core-shell particle (95) have been proved to have great photocatalytic activity for water splitting reactions.

Yolk–shell-nanostructured photocatalysts have rarely been reported because this is a relatively new concept. To the best of our knowledge, only a few YSNs have been synthesized and tested in photocatalytic water splitting. Nanoparticles consisting of a noble metal core/yolk in a semiconductor shell have distinct advantages. 1. A noble metal core/yolk encapsulated in a semiconductor shell transfers the charges created during light absorption, which helps to prevent aggregation. 2. A noble metal has a very low Fermi energy level, which can extend the catalyst life and improve the

performance. 3. Reduction and oxidation of water occur on the core/yolk and shell, respectively, and this minimizes the possibility of recombination, as shown in Figure 2.6(A) (59, 94).

Multishelled hollow nanoreactors, h-(Pt–TiO_2)/CdS, consisting of hollow TiO_2 and CdS porous double shells with fine Pt nanoparticles deposited on the inner surface of the TiO_2 shell, were synthesized using an in situ growth and deposition method. Carboxyl-modified poly(methyl methacrylate) nanospheres were used as templates, and after deposition of Pt, TiO_2, and CdS, the templates were removed by calcination in air in order to create a hollow structure (87). h-(Pt–TiO_2)/CdS nanospheres of size approximately 318 nm with shells of thickness 25 nm and Pt nanoparticles of diameter 5 nm were tested in water splitting. They showed an excellent catalytic activity of 296 μmol h^{-1}/10 mg and apparent quantum efficiency (QE) of 14.5% at a wavelength of 420 nm (87). Analysis suggests that the specific morphology and the composites contributed to the outstanding catalytic activity. The use of CdS as the outer shell enhanced the reception of visible light and accurately directed photogenerated carriers to the inner TiO_2 shell (active sites); the Pt nanoparticles in the inner layer increased the reaction rate and the porous and hollow structures enabled sufficient transfer of molecules (87).

A composite consisting of Ni metal and ZnO (7–23 nm) enclosed in porous carbon shells, (Ni–ZnO)@C, is an efficient photocatalyst for generating H_2 gas. Ni and ZnO are the main active sites. This yolk–shell structure was formed by partial etching of Ni and ZnO from (Ni–ZnO)@C core–shell nanoparticles (88). The porous carbon shell allows reactants to diffuse freely through the shell. (Ni–ZnO)@C with a Ni/Zn molar ratio of 1 gave the best results, and H_2 gas production from seawater splitting using (Ni–ZnO)@C was approximately 20.8 times higher than that using bare TiO_2 nanoparticles (88).

Wang *et al*. (98) recently employed graphene into yolk-shell nanoreactor composite for photocatalytic application; it was proved that graphene hybridized with TiO_2 could suppress the recombination of electron-hole pairs and enhance light absorption. They reported that graphene hybridized with TiO_2 suppressed recombination of electron–hole pairs and enhanced light absorption. A nanoreactor consisting of Au nanoparticles encapsulated in a hybrid shell consisting of reduced graphene oxide and TiO_2 (Au@r-GO/TiO_2) was prepared using a sol–gel coating process, calcination,

and selective template etching; the nanoreactor showed high water splitting photocatalytic activity, with a H_2 production rate of 462 μmol $h^{-1}g^{-1}$ and an apparent QE of 2.5%. Tests showed that the catalyst had high stability, with no obvious loss of activity after six cycles. Some yolk–shell microreactors also gave excellent catalytic performances in water splitting for H_2 production, such as yolk–shell TiN microparticles (99),yolk-shell MoS_2 microparticles (100) and KNb_3O_8 yolk-shell microspheres (101).

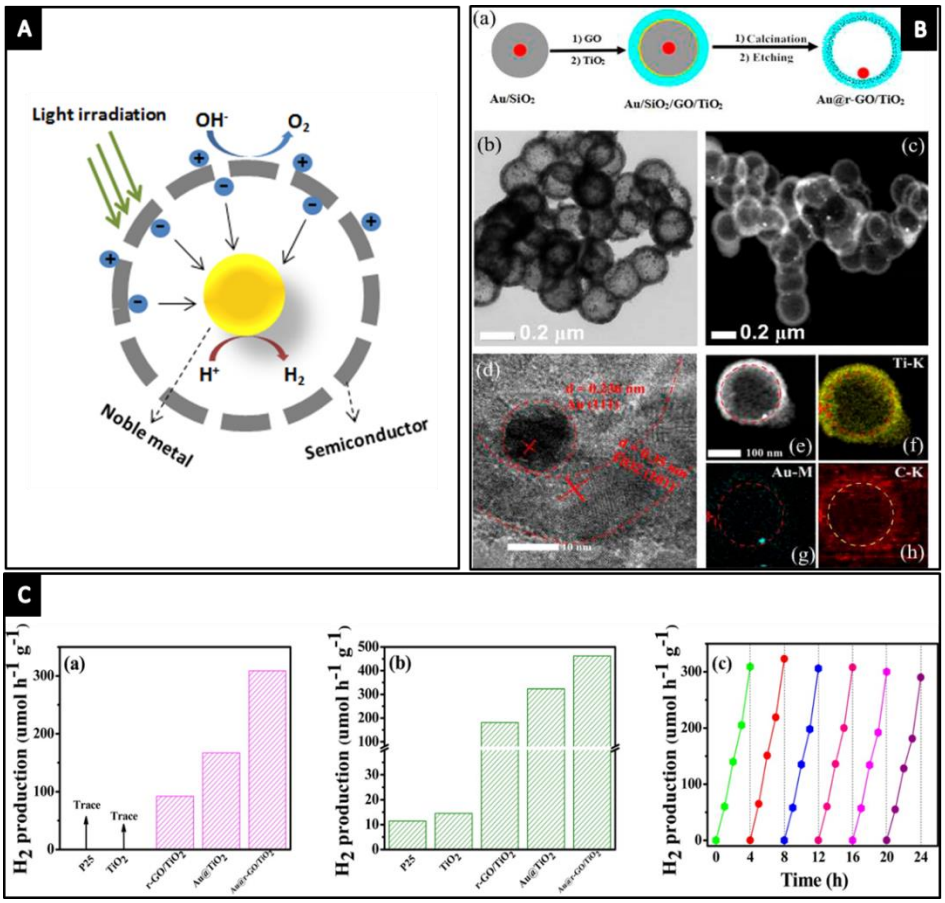

Figure 2.6: A. Schematic diagram of water splitting process mechanism in noble metal@semiconductor YSNs; B. (a) Schematic diagram of Au@r-GO/TiO_2 synthesis steps, (b) TEM image and (d) HRTEM of Au@r-GO/TiO_2, (c) and (e) HAADF-STEM images of Au@r-GO/TiO_2, (f)-(h) EDS mapping images of single Au@r-GO/TiO_2 nanoparticles; C. Comparison of hydrogen production from methanol aqueous solution from different catalysts (a) visible light irradiation (b) simulated daylight irradiation, (c) recyclability of Au@r-GO/TiO_2 nanoparticles in hydrogen production under visible light irradiation. (panels B and C reproduced with permission from ref. (98), Copyright © 2016 American Chemical Society).

Reduction of carbon dioxide, Reduction of CO_2 through light absorption, which mimics natural photosynthesis, converts CO_2 and H_2O to hydrocarbon fuels such as methane, methanol, formaldehyde, ethanol, and formic acid, and O_2 (102-107). The reduction of CO_2, which is abundant, is an attractive sustainable energy production method and also helps to reduce this greenhouse gas in the environment. CO_2 is an extremely stable molecule and is difficult to activate for chemical reactions. In traditional methods, high temperatures and electrical voltages are needed to break CO_2 molecules, and this is unsustainable and costly (103). In 1979, selective reduction of CO_2 was first achieved using a photocatalytic method to produce hydrocarbon fuel (102). So far, a number of semiconductors have been identified as effective photocatalysts for CO_2 reduction in the liquid or gas phase, e.g. TiO_2, CdS, $ZnGa_2O_4$, and $ZnGe_2O_4$ (102, 104, 107-109). TiO_2 is a good semiconductor photocatalyst, but it has low photocatalytic activity under UV irradiation for selective reduction of CO_2. Cocatalysts are therefore needed to obtain better catalytic performances. Noble or coinage metals such as Au, Ag, Pt, Pd, Rh, and Cu are suitable cocatalyst materials (108, 110). The mechanism of photocatalytic reduction involves the formation of H atoms, C–O bond breaking, and C–H and O–H bond formation under UV irradiation with a catalyst, in the presence of H_2O and CO_2 (as shown in Figure 2.7 A) (102, 104).

A combination of mesoporous Au@TiO_2 YSNs and an induced electric field provides an effective catalytic system for reduction of CO_2. Such plasmonic metal/semiconductor hybrid nanoparticles have recently been shown to be good potential candidates for use in many photocatalytic applications. Au@TiO_2 nanoparticles of size 200–250 nm with an average shell thickness of around 50 nm and a Au core of diameter 45 nm were synthesized using a hydrolysis–deposition method. First, carbon was coated on the Au nanoparticle surface before deposition of a TiO_2 layer; the carbon layer acted as a sacrificial template and was removed to create voids between the core and the shell (107). Catalytic tests indicated that Au@TiO_2 YSNs gave a very high photoreduction yield of CO_2, with a CH_4 production rate of 2.52 μmol $h^{-1}g^{-1}$, which is about 3.6 times higher than that achieved using the commercial catalyst P25, and generation of the more valuable high-grade carbon compound C_2H_6 at a rate of 1.67 μmol $h^{-1}g^{-1}$ under UV-vis-light irradiation (107). Analysis suggests that plasmonic metal/semiconductor hybrid

nanoreactors combined with an applied electric field can promote the generation and subsequent separation of electron–hole pairs at catalytic active sites, leading to an improved catalytic performance and production of high-grade carbon species. Titanate nanosheet-assembled yolk–shell microspheres have also been synthesized and tested for photocatalytic CO_2 reduction; they showed excellent catalytic activity (111).

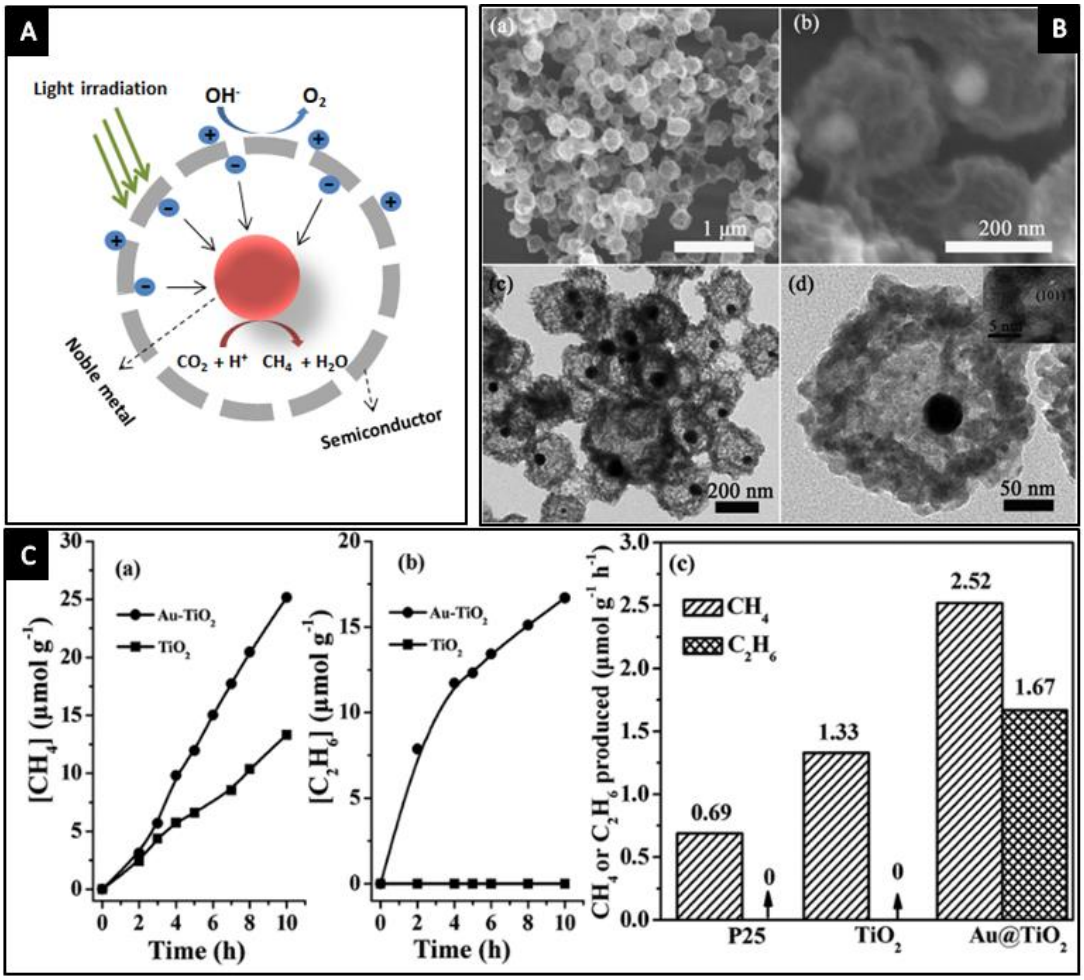

Figure 2.7: A. Schematic diagram of CO_2 reduction mechanism in noble metal@semiconductor YSNs; B. (a and b) SEM images, (c and d) TEM images of Au@TiO_2 YSNs (insert of (d) is the HRTEM image); C. (a) CH_4 (b) C_2H_6 productions catalysed by Au@TiO2 YSNs and bare hollow TiO_2 spheres, (c) comparison of photocatalytic activities of P25, TiO_2 hollow spheres and Au@TiO_2 YSNs. (panels B and C reproduced with permission from ref. (107), Copyright © The Royal Society of Chemistry 2015).

Recently, a yolk–shell catalyst consisting of carbon nanospheres encapsulated in hollow TiO_2 shells (C@TiO_2) was synthesized by coating carbon with a uniform

layer of TiO_2 by hydrolysis and condensation, followed by calcination at 450 °C; the catalyst nanoparticle diameter was approximately 420 nm and the size of the encapsulated yolk was 350 nm (112). Photocatalytic tests were performed in a custom-made Pyrex glass reactor at room temperature and atmospheric pressure under simulated solar light ($\lambda > 200$). A C@TiO_2 sample calcined for 120 min had the best catalytic activity in production of both methane and methanol. The methane production rate achieved with C@TiO_2 (4.22 μmol $h^{-1}g^{-1}$) was about twice that obtained using the commercial catalyst P25 (112). This shows that carbon played a crucial role in boosting the photocatalytic performance in CO_2 reduction.

Not many yolk–shell-nanostructured photocatalysts have been tested in the photocatalytic reduction of CO_2. Here, we introduce a few core–shell nanoreactors. Ni@NiO/$InTaO_4$–N core–shell nanoparticles were synthesized and showed enhanced photocatalytic activity. The production yield achieved from CO_2 reduction was higher than those obtained using $InTaO_4$–N and as-prepared $InTaO_4$ (59, 109). The Ni metal core was encapsulated in two shell layers, consisting of NiO and $InTaO_4$–N. In this photocatalyst, Ni@NiO acts as a cocatalyst, which improves the photocatalytic performance of $InTaO_4$. Cu/Pt/TiO_2 core–shell nanoparticles were also synthesized and tested. This nanoparticle composite gave good selectivity for CO_2 reduction, i.e. 85%, compared with those of Pt@TiO_2 and Cu@TiO_2, which gave selectivities of 41% and 80%, respectively (108). Ag-doped multiwalled carbon nanotubes@TiO_2 (MWCNT@TiO_2) core–shell nanoparticles were fabricated for reduction of CO_2 to methane and ethylene. This nanoreactor gave the best catalytic performance at a Ag weight percentage of 2% (110). It is believed that more yolk–shell-nanostructured photocatalysts for reduction of CO_2 will be developed. The advantages of yolk–shell structures will lead to better catalytic performances.

Degradation of pollutants, another application of photocatalysis, uses visible light and appropriate photocatalysts to effectively remove organic contaminants from wastewater. Semiconductors are again efficient photocatalysts, and combinations of the most popular semiconductor, TiO_2, and cocatalysts have been widely used. Recently, a number of yolk–shell photocatalysts for photocatalytic degradation of pollutants have been reported, some of which are micro-sized nanoparticles, and are briefly introduced here. ZnO hollow spheres with a double-yolk structure, formed by bubble-assisted Ostwald ripening, gave more than 90% degradation of rhodamine B

(RhB) (113). Ti^{3+} self-doped titanium oxide YSNs aggregated into micro-sized spheres to form TiO_2 powders, which gave RhB degradation percentages of 80.3%, 98.2%, and 99.3% in 5, 20, and 30 min, respectively (58). Ag-loaded nitrogen-doped yolk–shell mesoporous TiO_2 hollow microspheres were also investigated and gave good catalytic performances in the photodegradation of both RhB and the antibiotic ciprofloxacin (114). Yolk–shell-structured $Bi_{4-2x}Mo_xO_6$ ($x \leq 1$) microspheres were synthesized; $Bi_{2.38}Mo_{0.81}O_6$ synthesized via a solvothermal method had the best catalytic activity, giving 99% degradation of RhB and 72% degradation of methyl orange after 120 min (115). Yolk–shell $Au@CeO_2$ microspheres showed good catalytic activity and gave 95% decolouration of methylene blue at room temperature in 40 min (116).

A yolk–shell-structured nano-sized catalyst, namely the Au@r-GO/TiO_2 yolk–shell nanoreactor which was also used for water splitting, was investigated for photocatalytic decomposition of RhB. The nanoreactor gave 99.6% RhB degradation in 50 min, with a QE of 3.4%, under simulated daylight; this is much higher than the degradation achieved using the commercial catalyst P25 under the same conditions (98). This nanoreactor had good catalytic stability, although the catalytic activity declined slightly after six runs. The good catalytic performance is attributed to the graphene-hybridized TiO_2 shell, as previously discussed.

$Fe_3O_4@C@TiO_2$ YSNs, which consist of a Fe_3O_4 core coated with a carbon layer and a $Fe_3O_4@C$ yolk encapsulated in a mesoporous TiO_2 shell, were also tested in pollutant degradation. These YSNs were synthesized by self-assembly of poly(acrylic acid) (PAA), which was used as a template, on suspended Fe_2O_3 nanoparticles to form $Fe_2O_3@PAA$ core–shell nanoparticles. The addition of tetrabutyl titanate resulted in aggregation of small amorphous TiO_2 nanoparticles on the PAA layer. A porous TiO_2 shell was formed through formation of anatase nanocrystals from amorphous particles by annealing. Finally, heat treatment of the $Fe_2O_3@PAA@TiO_2$ core–shell nanoparticles reduced the PAA to carbon and Fe_2O_3 to Fe_3O_4, with simultaneous void formation between carbon and TiO_2 (117). This novel method gave an excellent multifunctional photocatalyst with a large surface area and magnetic properties. Experimental results for RhB photodegradation showed that $Fe_3O_4@C@TiO_2$ YSNs had excellent catalytic activity during five

cycles(117). The magnetic cores enabled easy recovery of the catalyst using an external magnetic field.

Joo *et al*. reported fabrication of C@TiO_2 yolk–shell-nanostructured particles with a tuneable size, crystallinity, and phase for pollutant degradation. C@TiO_2 was prepared using a templating method with silica-protected calcination and selective etching, in which the silica layer acted as a protecting layer and helped to maintain the structural integrity of the TiO_2 shells during high-temperature calcination (118). Post-treatments, namely acid treatment and recalcination, were performed to improve the crystallinity of the TiO_2 shells, which was a significant factor in the photocatalytic performance. The catalytic activity in RhB degradation of a sample post-treated and calcined at 750 °C was better than those of samples without post-treatments, with post-treatments but calcined at different temperatures, and commercial P25 TiO_2 (118). It is believed that not only the crystallinity degree of TiO_2 but also the carbon material used in the nanoreactor had positive effects on photocatalysis.

Recently, a nanoreactor consisting of magnetic material, noble metal and semiconductor was synthesized and applied in photocatalytic degradation of pollutants. Without a doubt, such a nanoreactor possessed several distinctive advantages from the compositional perspective; such as combination of noble metal/plasmonic metal with semiconductor could form local surface plasmon resonance (LSPR) adsorption and help in enhancing catalytic activity while magnetic material could assist in separation recyclability of nanoreactor by applying external magnetic field. Sea urchin-like Fe_3O_4@TiO_2@Ag yolk-shell nanoreactor with Ag (4 nm) nanoparticles loaded on both TiO_2 surface and inside the cavity, having Fe_3O_4 as core and nanofiber TiO_2/Fe_3O_4/Ag nano-heterojunctions as shell, prepared by modified hydrothermal method and photochemical reduction technique (Figure 2.8) exhibited excellent photocatalytic ability for degradation of ampicillin (AMP) under both ultraviolet and visible light irradiation (119). The degradation rates reached 98.7% under ultraviolet irradiation and 91.5% under visible light irradiation by using sea urchin-like Fe_3O_4@TiO_2@Ag nanoreactors which showed absolute better catalytic performance in comparison with Fe_3O_4@TiO_2 and Fe_3O_4 particles (119). In terms of recyclability, such yolk–shell nanoreactors can be easily separated by magnetic force and no change in the photocatalytic activity was observed after five cycles. Moreover,

this facile synthetic method enables precise and easy control of the cavity size, shell thickness, and particle size.

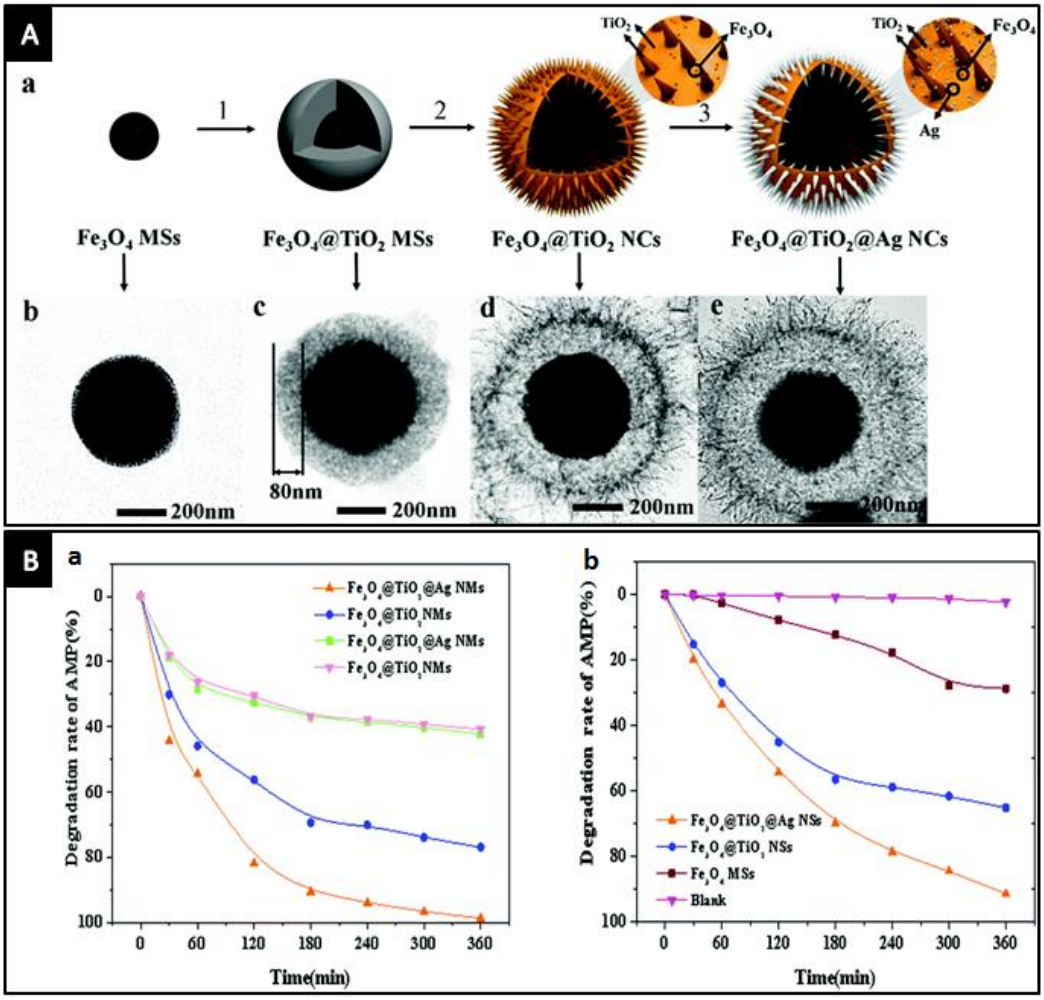

Figure 2.8: A. a: Schematic diagram of synthesis of Fe_3O_4@TiO_2@Ag yolk-shell nanoparticle, and b-e: TEM images at each synthesized step; B. Photodegradation results of AMP under ultraviolet irradiation (left), photodegradation results of AMP under visible light irradiation (right). (panels A and B reproduced with permission from ref. (119), Copyright © The Royal Society of Chemistry 2016)

Table 2.3: Summary of the catalytic performance of nanoreactors applied in photocatalytic water splitting, carbon dioxide reduction and degradation of pollutants applications.

Application	Catalyst		Performance				Ref
	Particle name	**Structure***	**Illumination**	**H_2 production**	**Quantum efficiency**	**Tested time**	
Water splitting $2H_2O \leftrightarrow 2H_2 + O_2$	**$NiFe_2O_4$@TiO_2**	CS	UV-vis light (λ= 365nm)	215.8 μmol h^{-1}/g (calculated)	NA	8 hour	(89)
	Pt-SiO_2@IrO_2-Ti3N5	CS	UV-vis light (λ>420nm)	46 μmol h^{-1}/g (calculated)	NA	NA	(92)
	$SrTiO_3$core:La/Rh	CS	UV-vis light (λ>420nm)	280 μmol h^{-1}/g (calculated)	NA	16 hour	(95)
	h-(pt-TiO2)/CdS	YS	Visible light (λ> 420 nm)	296 μmol h^{-1}/10mg	14.5%	70 hour	(87)
	(Ni-ZnO)@C	YS	UV–vis light	5.01 μmol h^{-1}/g_{cat}	NA	NA	(88)
	Au@r-GO/TiO_2	YS	Visible light (λ< 400 nm)	462 μmol h^{-1}/g	2.5%	24 hour	(98)

Carbon dioxide reduction	**Particle name**	**Structure***	**Illumination**	**Carbon fuel production**	**Chemical reaction**	
	Au@TiO_2	YS	UV-vis light	CH_4 = 6.34 μmol h^{-1}/g C_2H_4= 0.68 μmol h^{-1}/g	$CO_2 + 2H_2O \rightarrow 2O_2 + CH_4$ $2CO_2 + 2H_2O \rightarrow 3O_2 + C_2H_4$ $2CO_2 + 3H_2O \rightarrow 3.5O_2 + C_2H_6$	(107)
	C@TiO_2	YS	Solar light	CH_4 = 4.22 μmol h^{-1}/g		(112)
	Ni@NiO/$InTaO_4$-N	CS	Visible light (λ= 390nm-770 nm)	$CH_4 \approx$ 160 μmol h^{-1}/g (calculated)		(59, 109)
	Cu/Pt/TiO_2	CS	UV-vis light (λ = 320-780 nm)	CH_4 = 33 μmol h^{-1}/g		(108)
	Ag-MWCNT@TiO_2	CS	Visible light	CH_4 = 6.34 μmol h^{-1}/g C_2H_4= 0.68 μmol h^{-1}/g		(110)

Degradation of pollutants $R + OH^- \rightarrow R^- + H_2O$	**Particle name**	**Structure***	**Illumination**	**Pollutant degradation efficiency**	**Quantum efficiency**	**Tested time**	
	Au@r-GO/TiO_2	YS	Visible light (λ=400 nm)	RhB = 99%	3.4%	100 min	(98)
	Fe_3O_4@C@TiO_2	YS	UV light	RhB ≈ 99%	NA	90 min	(117)
	C@TiO_2	YS	UV light (λ=365 nm)	RhB ≈ 99%	NA	30 min	(118)
	Fe_3O_4@TiO_2@Ag	YS	UV and visible lights	AMP = 98.7% (UV) AMP=91.5% (Visible)	NA	360 min	(119)

*CS: Core-shell; YS: Yolk-shell

2.3.3 Electrocatalysis

Fuel cells are energy-conversion devices with low emissions of environmentally hazardous compounds. Fuel cells convert chemical energy to electrical energy via a series of reduction and oxidation reactions at the anode, i.e. the hydrogen evolution/oxidation reaction or methanol oxidation reaction (MOR), and cathode, i.e. oxygen reduction reaction (ORR) or oxygen evolution reaction (OER) (120, 121). Proton exchange membrane fuel cells (PEMFCs) (Equation 2.3) and direct methanol fuel cells (DMFCs) (Equation 2.4) are the two main types of fuel cell. Fuel cells are important for green energy generation and can be used as portable power sources, e.g. in portable electronic devices or batteries. Fuel cell applications have been extensively researched; however, the sluggish kinetics of the ORR at the cathode is still a challenge (122-124). In recent decades, researchers have investigated electrode materials which enhance the performances of fuel cells. The electrocatalyst is the critical factor in the fuel cell performance (125). Pt is the most commonly used electrocatalyst for fuel cells, but a pure Pt electrocatalyst suffers from CO poisoning because of its low CO tolerance, which leads to insufficient catalytic activity, high costs, and low durability. Many alternative metals, metal-free materials, and catalysts with various structures, such as non-precious metals, nitrogen-doped carbons, Pt-based alloys, and core–shell or yolk–shell catalysts, have been therefore been intensively investigated (120-124, 126-131). In terms of current commercial electrocatalysts, Pt loaded on a carbon support (Pt/C) gives excellent catalytic performances (127). A good catalyst can improve fuel cell performance in many ways such as durability, stability and catalytic activity. Therefore, the ideal electrocatalyst should possess the following characters: 1. high surface area; 2. high conductivity; 3. high porosity and pore accessibility; and 4. good electrochemical stability even under harsh reaction condition.

Equation 2.3: PEMFC reactions.

$$Cathode: \frac{1}{2}O_2 + 2H^+ + 2e^- \rightarrow H_2O$$

$$Anode: H_2 \rightarrow 2H^+ + 2e^-$$

$$Overall: \frac{1}{2}O_2 + H_2 \rightarrow H_2O$$

Equation 2.4: DMFCs reactions.

$$Cathode: \frac{3}{2}O_2 + 6H^+ + 6e^- \rightarrow 3H_2O$$
$$Anode: CH_3OH + H_2O \rightarrow CO_2 + 6H^+ + 6e^-$$
$$Overall: CH_3OH + \frac{3}{2}O_2 \rightarrow CO_2 + 2H_2O$$

Methanol oxidation reaction (MOR) is the key reaction at the anode in DMFCs, which are promising power sources for portable electronic devices and electric vehicles. Here, we discuss a few yolk–shell-nanostructured electrocatalysts for the MOR. The MOR activity of a Au@Pt yolk–shell electrocatalyst of diameter approximately 100 nm, which was synthesized using a galvanic displacement method, was investigated (126). The experimental results showed that this electrocatalyst had high CO tolerance, which prolonged the Pt durability, good catalytic activity, and a significantly decreased MOR overpotential. The MOR activity of a Fe_3O_4–polydopamine–graphene–Pt yolk–shell nanocomposite (Fe_3O_4@PDA/RGO/Pt) was also investigated. First, a Fe_3O_4 yolk was coated with PDA to prepare core–shell nanoparticles, and then then RGO, which acted as a shell or support, was formed using a hydrothermal process to immobilize Fe_3O_4@PDA and prevent particle agglomeration. Pt nanoparticles were then distributed on the PDA shell and RGO, and voids were formed between the yolk and shell by partial dissolution of the yolk (129). The catalytic activity of this yolk–shell electrocatalyst was about 2.6 times that of a commercial catalyst because of its smaller size, better distribution of Pt nanoparticles, good catalyst support, and larger number of functional groups. Highly dispersed and porous Au@pPt YSNs (140 nm) with Pt shells of thickness approximately 20 nm, Au yolks of size 15 nm, and pores of size 6 nm were created by Pt deposition and selective etching; a silica layer, which was used as a template, was coated on the Au core surface before the outer Pt shell was removed to form a yolk–shell structure (121). This nanoreactor gave a current density about 1.9 times higher than that obtained using commercial Pt black under acidic conditions, and better catalytic activity and stability under alkaline conditions, as shown in Figure 2.9. Finally, the physical and chemical properties of a micro-sized catalyst, consisting of PtCu alloy yolk–shell cubes prepared via disproportionation and displacement reactions in Cu_2O yolk–shell cubes, differed from those of ordinary

spherical nanoparticles because its crystal planes were different. The PtCu alloy yolk–shell nanocubes had good MOR activity in acidic solution, about 2.5 times better than that of a commercial Pt/C electrocatalyst (127).

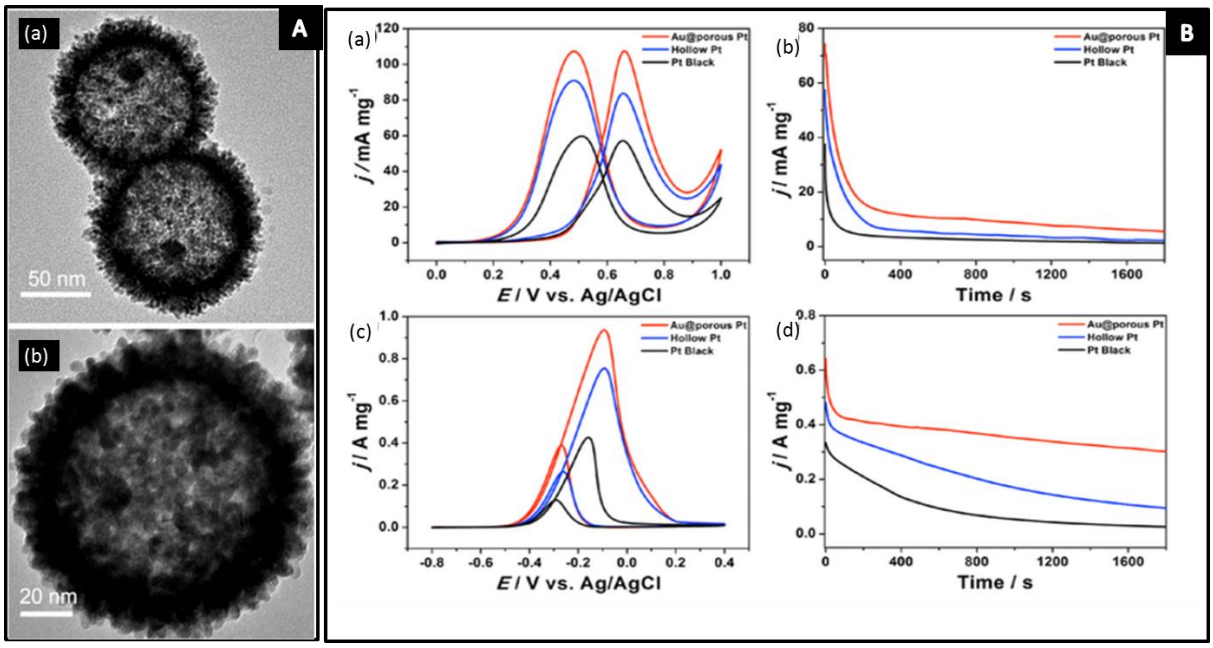

Figure 2.9: A. (a) and (b) TEM images of Au@pPt YSNs; B. (a) Cyclic voltammograms (b) chronoamperometric curves recorded at 0.6V for MOR catalysed by Au@pPt, hollow Pt and Pt black catalysts under acidic condition, (c) Cyclic voltammograms (d) chronoamperometric curves recorded at -0.2V for MOR catalysed by Au@pPt, hollow Pt and Pt black catalysts under alkaline condition. (panels A and B reproduced with permission from ref. (121). Copyright © 2015 WILEY-VCH Verlag GmbH & Co. KGaA, Weinheim)

Oxygen reduction reaction (ORR) occurs at the cathode in both PEMFCs and DMFCs. As already mentioned, the sluggish kinetics of this reaction is a major challenge in fuel cell development. Appropriate electrocatalysts are therefore needed to improve the ORR kinetics. It has been suggested that the ORR kinetics involves two pathways: one is direct four-electron pathway and the other is an indirect (peroxide) pathway (130, 132) Many efficient catalysts have been suggested, but not many of them have nanoscale yolk–shell structures. Here, we present two recent examples of core–shell nanoparticles and yolk–shell-structured nano-electrocatalysts, and some yolk–shell microreactors. Core–shell-structured nanoparticles, namely $Co@Co_3O_4$ core–shell nanoparticles embedded in bamboo-like nitrogen-doped

carbon nanotubes ($Co@Co_3O_4$/BNCNTs), were prepared via thermal treatment and oxidation (124). Tests showed that the Co/BNCNTs did not show effective catalytic activity before oxidation to form $Co@Co_3O_4$/BNCNTs. This suggests that a Co_3O_4 composite provides the active sites for the ORR reaction and the catalytic activity is related to the level of oxidation. These YSNs had moderate catalytic activity, excellent tolerance for methanol molecules, and better catalytic stability than commercial Pt black (124). Recently, highly active and durable PdAg@Pd core–shell nanoparticles were prepared and were shown to be a good potential ORR catalyst. PdAg bimetallic alloy nanoparticles of size approximately 6 nm were prepared via oleylamine reduction of Pd and Ag precursors, and ultrathin Pd shells were formed by electrochemical treatment (100 cycles of electrocatalysis) of the PdAg alloy in an acidic medium (133). The electrocatalytic activity was evaluated by attaching the nanoparticles to active carbon; the nanoparticles showed good catalytic activity and durability in the ORR.

The Au@pPt porous yolk–shell nanoreactor, which, as mentioned above, was used in the MOR, was also tested in the ORR using O_2-saturated 0.1 $molL^{-1}$ KOH. The catalytic activity of this nanoreactor was better than that of hollow Pt and Pt black, and it gave an onset potential of 0.12 V, which is a 30 mV positive shift from the onset potential of hollow Pt and a positive shift double that from the onset potential of Pt black (121). This proves that the Au@pPt catalyst has good catalytic activities in both the MOR and ORR. Iron carbide was also found to play a significant role in improving electrocatalytic performances in the ORR. $Fe_{2.5}C$ buried in a nitrogen-doped carbon shell together with an Fe_3O_4 core ($Fe_3O_4@Fe_{2.5}C$/N-doped C) was fabricated using a templating approach and calcination under a nitrogen flow (122). This yolk–shell nanoreactor with particles of size 400–500 nm, a shell thickness of 40 nm, and a yolk size of 140 nm was tested in the ORR in alkaline solution. The experimental results show that the catalyst had high stability, with only slight decay in the activity after 1000 cycles (122). synthesized $Co_3O_4/NiCO_2O_4$ box-in-box rattle-type double-shelled nanocages using zeolitic imidazolate framework-67/Ni–Co layered double hydroxide YSNs by thermal annealing in air (134). This novel synthetic method is versatile and can be used to produce double-shelled nanocages with various compositions. The catalytic performance of $Co_3O_4/NiCO_2O_4$ nanocages in which both shells were of thickness around 20 nm were investigated in the OER.

The results show that the catalytic activity was better than those of Co_3O_4 and Co_3O_4/Co_3O_4 nanocages and that the catalyst had good stability. Recently, this group of researchers reported the use of a metal–organic framework to form Co-nanoparticle-embedded carbon@Co_9S_8 (Co–C@Co_9S_8) rattle-type double-shelled nanocages via thermal annealing of ZIF-67@a–CoS YSNs, as shown in Figure 2.10(A) (135). The electrocatalytic activity and stability in the ORR were tested. The results showed that the current density at a rotating speed of 1600 $rmin^{-1}$ reached 4.5 mA cm^{-2} at 0.5 V, which is much greater than the values for many other nanoparticles based on Co, Co_3O_4, or carbon, and the current retention was 96% after 5 h, as shown in Figure 2.10(C) (135). Analysis suggests that for a rattle-type hollow double-shelled structure, the high exposure and accessibility of the active sites contribute to the outstanding catalytic performance. Finally, many yolk–shell-structured microparticles have been used in the ORR and shown excellent electrocatalytic activities, e.g. Fe_3O_4@Co_3O_4 yolk–shell microspheres (132), yolk-shell Co and N codoped porous carbon microspheres (136), yolk-shell structured $La_{0.9}Sr_{0.1}$CoO3 perovskite microspheres (137), yolk-shell structured N/P/B ternary-doped biocarbon microparticles (138) and $Ni_{0.69}Co_{0.31}$–P yolk-shelled microspheres (139). In Table 2.4, the catalytic performance of as mentioned core-shell and yolk-shell structured nanoreactors applied in both methanol reduction reaction and oxygen reduction reaction have been summarized.

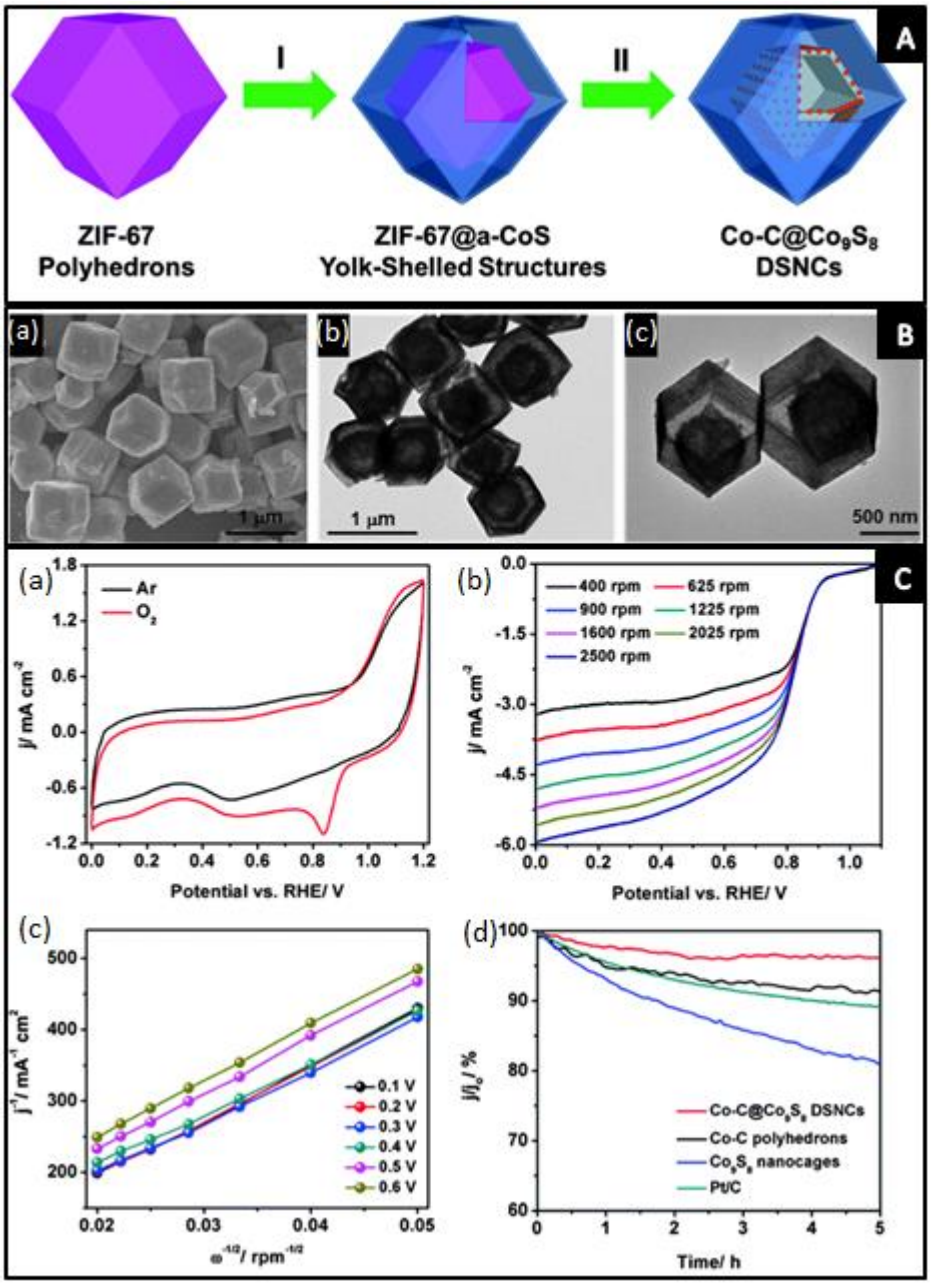

Figure 2.10: A. Schematic illustration of synthesis steps of Co-C@Co_9S_8 double-shelled nanocages; B. (a) FESEM image of Co-C@Co_9S_8, (b) and (c) TEM images of Co-C@Co_9S_8; C. (a) cyclic voltammetry curves of Co-C@Co_9S_8 in an Ar^- or $O2^-$ saturated 0.1M KOH solution at a scan rate of $10mVs^{-1}$, (b) linear sweep voltammograms curves of Co-C@Co_9S_8 at different rotating speed, (c) Koutecky-Levich plots of Co-C@Co_9S_8 at various potentials, (d) stability comparisons between Co-C@Co_9S_8, Co-C, Co_9S_8, and Pt black at 1600rpm rotating speed in $O2^-$ saturated 0.1M KOH solution. (panels A and B reproduced with permission from ref. (135). Copyright ©The Royal Society of Chemistry 2016)

Table 2.4: Summary of catalytic performance of nanoreactors applied in methanol oxidation reaction and oxygen reduction reaction.

Application	Catalyst			Performance			Ref
	Particle name	Structure *	Synthesis method	Testing condition	Catalytic activity	Stability	
Methanol oxidation reaction $CH_3OH + H_2O \rightarrow CO_2 + 6H^+ + 6e^-$	**Au@Pt**	YS	Galvanic displacement	Alkaline solution	mass current density= 86.1 mA mg_{Pt}^{-1}	Stable	(126)
	Fe_3O_4@PDA/RGO/Pt	YS	Hydrothermal method	Acidic solution	mass current density= 385.3 mA mg_{Pt}^{-1} 2.6 times higher than that of the Pt black	Not very stable	(129)
	Au@pPt	YS	Template approach and selective etching	Acidic solution Alkaline solution	Acidic : mass current density= 107.5 mA mg^{-1} catalyst 1.9 times higher than that of the Pt black Alkaline: mass current density= 936.0 mA mg^{-1} catalyst	Stable	(121)
Oxygen reduction reaction $\frac{1}{2}O_2 + 2H^+ + 2e^- \rightarrow H_2O$	**Co@Co_3O_4/BNCNTs**	CS	Thermal treatment and oxidation process	Alkaline solution	Not as good as Pt black	Stable	(124)
	PdAg@Pd	CS	Oleylamine-reduction and electrochemical treatment	Acidic solution	Positive shift of onset potential, similar current density as Pt black	Stable	(133)
	Au@pPt	YS	Template approach and selective etching	Alkaline solution	Better onset potential and current density than Pt black	NA	(121)
	Fe_3O_4@$Fe_{2.5}$C/N-doped C	YS	Template approach and calcination	Alkaline solution	Good activity	Stable	(122)
	Co-C@ Co_9S_8	YS	thermal annealing	Alkaline solution	Close to 20wt% Pt black	Stable	(135)

*CS: Core-shell; YS: Yolk-shell

2.4 Summary and Outlook

In this chapter, we have summarized the general synthetic methods for yolk–shell particles, and their recent use as nanoreactors in energy-conversion applications. Precise tuning of their structures, particle sizes, and functionalities will provide next-generation YSNs with nanoarchitectures that make them attractive catalysts for many important chemical reactions.

Although many different synthetic methods have been developed in the past decade, the development of more universal, effective, environmentally friendly, and low-cost synthetic methods is still a primary research aim. Several methods for YSN synthesis were described and compared; however, a general method for synthesizing more complex YSNs is still needed. Recently, there has been rapid growth in advanced approaches for YSN synthesis (140-143), but much research is still needed to optimize the synthetic parameters. Moreover, the complexity of the synthetic processes and lack of precise control in fabricating YSNs need to be tackled; these are the main issues preventing large-scale YSN production and their commercial use.

YSNs are designed to have significant advantages over conventionally structured catalysts; however, the use of nanoreactors is still new and limited. The components of yolk–shell structures could be selectively functionalized to enable multiple reactions to be performed simultaneously. Multifunctional catalysts are highly desirable for complex chemical reactions such as tandem reactions. Moreover, the porosity of the protective shell could be further tailored to regulate the diffusion rates of reactants to enable better control of the reaction rate, and gain direct control of the catalytic performance. Furthermore, the recyclability of YSNs with protective shells around their active core will benefit their use as nanoreactors. Precisely locating the active sites in YSNs will improve our understanding of the relationship between structure and performance, and enable cooperative catalysis to be achieved. In addition, the use of YSN nanoreactors in many major chemical reactions has not yet been tested, and further research in this area is expected.

We believe that yolk–shell nanoreactors have great potential for improving chemical reactions. Multidisciplinary studies and collaboration are needed to fully realize the potential of yolk–shell nanoreactors. Significant progress has been made in the synthesis and applications of yolk–shell nanoreactors, and research in this area will

continue to be popular in the future. The synthesis and use of optimized yolk–shell nanoreactors for high-value chemical production is the goal.

Reference

1. Toumey C. Plenty of room, plenty of history. Nat Nanotechnol. 2009;4(12):783-4.

2. Ostafin A, Chen Y-C. Nanoreactors. Kirk-Othmer Encyclopedia of Chemical Technology: John Wiley & Sons, Inc.; 2000.

3. Liu J, Qiao SZ, Chen JS, Lou XW, Xing X, Lu GQ. Yolk/shell nanoparticles: new platforms for nanoreactors, drug delivery and lithium-ion batteries. Chem Commun. 2011;47(47):12578-91.

4. Yang Y, Liu X, Li X, Zhao J, Bai S, Liu J, et al. A Yolk–Shell Nanoreactor with a Basic Core and an Acidic Shell for Cascade Reactions. Angew Chem Int Ed. 2012;51(36):9164-8.

5. Zhang H, Huang H, Liu Y, Han X, Ma Z, Zhang L, et al. Porous and hollow metal-layer@SiO2 nanocomposites as stable nanoreactors for hydrocarbon selective oxidation. J Mater Chem. 2012;22(38):20182-5.

6. Pérez-Lorenzo M, Vaz B, Salgueiriño V, Correa-Duarte MA. Hollow-Shelled Nanoreactors Endowed with High Catalytic Activity. Chem Eur J. 2013;19(37):12196-211.

7. Tian H, Li X, Zeng L, Gong J. Recent Advances on the Design of Group VIII Base-Metal Catalysts with Encapsulated Structures. ACS Catal. 2015;5(8):4959-77.

8. Guiet A, Göbel C, Klingan K, Lublow M, Reier T, Vainio U, et al. Hydrophobic Nanoreactor Soft-Templating: A Supramolecular Approach to Yolk@Shell Materials. Adv Funct Mater. 2015;25(39):6228-40.

9. Priebe M, Fromm KM. Nanorattles or Yolk–Shell Nanoparticles—What Are They, How Are They Made, and What Are They Good For? Chem Eur J. 2015;21(10):3854-74.

10. Liu J, Qiao SZ, Hu QH, lu GQM. Magnetic Nanocomposites with Mesoporous Structure: Synthesis and Applications. Small. 2011;7(4):425-43.

11. Jin R, Yang Y, Zou Y, Liu X, Xing Y. A General Route to Hollow Mesoporous Rare-Earth Silicate Nanospheres as a Catalyst Support. Chem Eur J. 2014;20(8):2344-51.

12. Jankiewicz BJ, Jamiola D, Choma J, Jaroniec M. Silica–metal core–shell nanostructures. Adv Colloid Interface Sci. 2012;170(1–2):28-47.

13. Yao T, Cui T, Fang X, Yu J, Cui F, Wu J. Preparation of yolk/shell Fe3O4@polypyrrole composites and their applications as catalyst supports. Chem Eng J. 2013;225(0):230-6.

14. Lin C-H, Liu X, Wu S-H, Liu K-H, Mou C-Y. Corking and Uncorking a Catalytic Yolk-Shell Nanoreactor: Stable Gold Catalyst in Hollow Silica Nanosphere. J Phys Chem Lett. 2011;2(23):2984-8.

15. Li G, Tang Z. Noble metal nanoparticle@metal oxide core/yolk-shell nanostructures as catalysts: recent progress and perspective. Nanoscale. 2014;6(8):3995-4011.

16. Li Z, Li M, Bian Z, Kathiraser Y, Kawi S. Design of highly stable and selective core/yolk–shell nanocatalysts—A review. Appl Catal, B. 2016;188:324-41.

17. Fang Q, Xuan S, Jiang W, Gong X. Yolk-like Micro/Nanoparticles with Superparamagnetic Iron Oxide Cores and Hierarchical Nickel Silicate Shells. Adv Funct Mater. 2011;21(10):1902-9.

18. Chen Z, Cui Z-M, Niu F, Jiang L, Song W-G. Pd nanoparticles in silica hollow spheres with mesoporous walls: a nanoreactor with extremely high activity. Chem Commun. 2010;46(35):6524-6.

19. Fang X, Zhao X, Fang W, Chen C, Zheng N. Self-templating synthesis of hollow mesoporous silica and their applications in catalysis and drug delivery. Nanoscale. 2013;5(6):2205-18.

20. Liu J, Yang HQ, Kleitz F, Chen ZG, Yang T, Strounina E, et al. Yolk–Shell Hybrid Materials with a Periodic Mesoporous Organosilica Shell: Ideal Nanoreactors for Selective Alcohol Oxidation. Adv Funct Mater. 2012;22(3):591-9.

21. Güttel R, Paul M, Galeano C, Schüth F. Au, @ZrO2 yolk–shell catalysts for CO oxidation: Study of particle size effect by ex-post size control of Au cores. J Catal. 2012;289(0):100-4.

22. Shmakov SN, Jia Y, Pinkhassik E. Selectively Initiated Ship-In-A-Bottle Assembly of Yolk–Shell Nanostructures. Chem Mater. 2013;26(2):1126-32.

23. Wu S, Dzubiella J, Kaiser J, Drechsler M, Guo X, Ballauff M, et al. Thermosensitive Au-PNIPA Yolk–Shell Nanoparticles with Tunable Selectivity for Catalysis. Angew Chem Int Ed. 2012;51(9):2229-33.

24. Liu B, Wang Q, Yu S, Zhao T, Han J, Jing P, et al. Double shelled hollow nanospheres with dual noble metal nanoparticle encapsulation for enhanced catalytic application. Nanoscale. 2013;5(20):9747-57.

25. Liang X, Li J, Joo JB, Gutiérrez A, Tillekaratne A, Lee I, et al. Diffusion through the Shells of Yolk–Shell and Core–Shell Nanostructures in the Liquid Phase. Angew Chem Int Ed. 2012;51(32):8034-6.

26. Park J, Song H. Metal@Silica yolk-shell nanostructures as versatile bifunctional nanocatalysts. Nano Res. 2011;4(1):33-49.

27. Purbia R, Paria S. Yolk/shell nanoparticles: classifications, synthesis, properties, and applications. Nanoscale. 2015;7(47):19789-873.

28. Song H. Metal Hybrid Nanoparticles for Catalytic Organic and Photochemical Transformations. Acc Chem Res. 2015;48(3):491-9.

29. Prieto G, Tüysüz H, Duyckaerts N, Knossalla J, Wang G-H, Schüth F. Hollow Nano- and Microstructures as Catalysts. Chem Rev. 2016.

30. Liu J, Qiao SZ, Budi Hartono S, Lu GQ. Monodisperse Yolk–Shell Nanoparticles with a Hierarchical Porous Structure for Delivery Vehicles and Nanoreactors. Angew Chem Int Ed. 2010;49(29):4981-5.

31. Li Z, Kathiraser Y, Kawi S. Facile Synthesis of High Surface Area Yolk–Shell Ni@Ni Embedded SiO2 via Ni Phyllosilicate with Enhanced Performance for CO2 Reforming of CH4. ChemCatChem. 2014:n/a-n/a.

32. Pak J, Yoo H. Synthesis and catalytic performance of multiple gold nanodots core–mesoporous silica shell nanoparticles. Microporous Mesoporous Mater. 2014;185(0):107-12.

33. Liu B, Wang Q, Yu S, Jing P, Liu L, Xu G, et al. Architecture engineering toward highly active palladium integrated titanium dioxide yolk-double-shell nanoreactor for catalytic applications. Nanoscale. 2014;6(20):11887-97.

34. Fang X, Liu S, Zang J, Xu C, Zheng M-S, Dong Q-F, et al. Precisely controlled resorcinol-formaldehyde resin coating for fabricating core-shell, hollow, and yolk-shell carbon nanostructures. Nanoscale. 2013;5(15):6908-16.

35. Zhang Q, Zhang T, Ge J, Yin Y. Permeable Silica Shell through Surface-Protected Etching. Nano Lett. 2008;8(9):2867-71.

36. Li J, Chen LX, Li X, Zhang CC, Zeng FL. Hollow organosilica nanospheres prepared through surface hydrophobic layer protected selective etching. Appl Surf Sci. 2015;340:126-31.

37. Zeng HC. Synthesis and self-assembly of complex hollow materials. J Mater Chem. 2011;21(21):7511-26.

38. Yec CC, Zeng HC. Synthesis of complex nanomaterials via Ostwald ripening. J Mater Chem A. 2014;2(14):4843-51.

39. Lou XW, Yuan C, Rhoades E, Zhang Q, Archer LA. Encapsulation and Ostwald Ripening of Au and Au–Cl Complex Nanostructures in Silica Shells. Adv Funct Mater. 2006;16(13):1679-84.

40. Wang Z, Zhou L, Lou XW. Metal Oxide Hollow Nanostructures for Lithium-ion Batteries. Adv Mater. 2012;24(14):1903-11.

41. Cao L, Chen D, Caruso RA. Surface-Metastable Phase-Initiated Seeding and Ostwald Ripening: A Facile Fluorine-Free Process towards Spherical Fluffy

Core/Shell, Yolk/Shell, and Hollow Anatase Nanostructures. Angew Chem Int Ed. 2013;52(42):10986-91.

42. Qin Z, Sun H, Jiang Z, Jiao X, Chen D. Synthesis of metal sulfide nanoboxes based on Kirkendall effect and Pearson hardness. CrystEngComm. 2013;15(5):897-902.

43. Polavarapu L, Liz-Marzan LM. Growth and galvanic replacement of silver nanocubes in organic media. Nanoscale. 2013;5(10):4355-61.

44. Anderson BD, Tracy JB. Nanoparticle conversion chemistry: Kirkendall effect, galvanic exchange, and anion exchange. Nanoscale. 2014.

45. Pearson A, O'Mullane AP, Bansal V, Bhargava SK. Galvanic replacement mediated transformation of Ag nanospheres into dendritic Au-Ag nanostructures in the ionic liquid [BMIM][BF4]. Chem Commun. 2010;46(5):731-3.

46. Xia X, Wang Y, Ruditskiy A, Xia Y. 25th Anniversary Article: Galvanic Replacement: A Simple and Versatile Route to Hollow Nanostructures with Tunable and Well-Controlled Properties. Adv Mater. 2013;25(44):6313-33.

47. Lee J, Kim SM, Lee IS. Functionalization of hollow nanoparticles for nanoreactor applications. Nano Today. 2014;9(5):631-67.

48. Xu P, Yu R, Ren H, Zong L, Chen J, Xing X. Hierarchical nanoscale multi-shell Au/CeO2 hollow spheres. Chem Sci. 2014;5(11):4221-6.

49. Jin J, Mitome T, Egashira Y, Nishiyama N. Phase control of ordered mesoporous carbon synthesized by a soft-templating method. Colloids Surf, A. 2011;384(1–3):58-61.

50. Mahmoud MA, Narayanan R, El-Sayed MA. Enhancing Colloidal Metallic Nanocatalysis: Sharp Edges and Corners for Solid Nanoparticles and Cage Effect for Hollow Ones. Acc Chem Res. 2013;46(8):1795-805.

51. Chen Y, Chen H, Guo L, He Q, Chen F, Zhou J, et al. Hollow/Rattle-Type Mesoporous Nanostructures by a Structural Difference-Based Selective Etching Strategy. ACS Nano. 2010;4(1):529-39.

52. Wang C, Chen J, Zhou X, Li W, Liu Y, Yue Q, et al. Magnetic yolk-shell structured anatase-based microspheres loaded with Au nanoparticles for heterogeneous catalysis. Nano Res. 2015;8(1):238-45.

53. Zhao ZY, Liu J, Hahn M, Qiao S, Middelberg APJ, He L. Encapsulation of lipase in mesoporous silica yolk-shell spheres with enhanced enzyme stability. RSC Adv. 2013;3(44):22008-13.

54. Kong L, Duan G, Zuo G, Cai W, Cheng Z. Rattle-type Au@TiO2 hollow microspheres with multiple nanocores and porous shells and their structurally enhanced catalysis. Mater Chem Phys. 2010;123(2–3):421-6.

55. Zeng HC. Preparation and integration of nanostructured titanium dioxide. Curr Opin Chem Eng. 2011;1(1):11-7.

56. Pan L, Liu H, Lei X, Huang X, Olson DH, Turro NJ, et al. ℝPM-1: A Recyclable Nanoporous Material Suitable for Ship-In-Bottle Synthesis and Large Hydrocarbon Sorption. Angew Chem Int Ed. 2003;42(5):542-6.

57. Dai C, Zhang A, Li J, Hou K, Liu M, Song C, et al. Synthesis of yolk-shell HPW@Hollow silicalite-1 for esterification reaction. Chem Commun. 2014;50(37):4846-8.

58. Wang S, Yang X, Wang Y, Liu L, Guo Y, Guo H. Morphology-controlled synthesis of Ti3+ self-doped yolk–shell structure titanium oxide with superior photocatalytic activity under visible light. J Solid State Chem. 2014;213(0):98-103.

59. Zhang N, Liu S, Xu Y-J. Recent progress on metal core@semiconductor shell nanocomposites as a promising type of photocatalyst. Nanoscale. 2012;4(7):2227-38.

60. Liu B, Zeng HC. Symmetric and Asymmetric Ostwald Ripening in the Fabrication of Homogeneous Core–Shell Semiconductors. Small. 2005;1(5):566-71.

61. Xie S, Jin M, Tao J, Wang Y, Xie Z, Zhu Y, et al. Synthesis and Characterization of Pd@MxCu1−x (M=Au, Pd, and Pt) Nanocages with Porous Walls and a Yolk–Shell Structure through Galvanic Replacement Reactions. Chem Eur J. 2012;18(47):14974-80.

62. Niu W, Zhang L, Xu G. Seed-mediated growth of noble metal nanocrystals: crystal growth and shape control. Nanoscale. 2013;5(8):3172-81.

63. Yeo KM, Shin J, Lee IS. Reductive dissolution of Fe3O4 facilitated by the Au domain of an Fe3O4/Au hybrid nanocrystal: formation of a nanorattle structure composed of a hollow porous silica nanoshell and entrapped Au nanocrystal. Chem Commun. 2010;46(1):64-6.

64. Jeong K, Kim SM, Lee IS. Seed-engineering Approach toward Hollow Nanoreactor Suitable for the Confined Synthesis of Less-noble Ni-based Nanocrystals. Chem Commun. 2014.

65. Rosario-Amorin D, Wang X, Gaboyard M, Clérac R, Nlate S, Heuzé K. Dendron-Functionalized Core–Shell Superparamagnetic Nanoparticles: Magnetically Recoverable and Reusable Catalysts for Suzuki C□C Cross-Coupling Reactions. Chem Eur J. 2009;15(46):12636-43.

66. Majewski AJ, Wood J, Bujalski W. Nickel–silica core@shell catalyst for methane reforming. Int J Hydrogen Energy. 2013;38(34):14531-41.

67. Mirzaei F, Rezaei M, Meshkani F. Coprecipitated Ni-Co Bimetallic Nanocatalysts for Methane Dry Reforming. Chem Eng Technol. 2014:n/a-n/a.

68. Ligthart DAJM, van Santen RA, Hensen EJM. Influence of particle size on the activity and stability in steam methane reforming of supported Rh nanoparticles. J Catal. 2011;280(2):206-20.

69. Zhao X, Li H, Zhang J, Shi L, Zhang D. Design and synthesis of NiCe@m-SiO2 yolk-shell framework catalysts with improved coke- and sintering-resistance in dry reforming of methane. Int J Hydrogen Energy. 2016;41(4):2447-56.

70. Lim Z-Y, Wu C, Wang WG, Choy K-L, Yin H. A novel and anti-agglomerating Ni@yolk-ZrO2 structure with sub-10 nm Ni core for high performance steam reforming of methane. RSC Adv. 2015;5(76):61925-32.

71. Bian Z, Suryawinata IY, Kawi S. Highly carbon resistant multicore-shell catalyst derived from Ni-Mg phyllosilicate nanotubes@silica for dry reforming of methane. Appl Catal, B. 2016;195:1-8.

72. Park JC, Bang JU, Lee J, Ko CH, Song H. Ni@SiO2 yolk-shell nanoreactor catalysts: High temperature stability and recyclability. J Mater Chem. 2010;20(7):1239-46.

73. Li L, He S, Song Y, Zhao J, Ji W, Au C-T. Fine-tunable Ni@porous silica core–shell nanocatalysts: Synthesis, characterization, and catalytic properties in partial oxidation of methane to syngas. J Catal. 2012;288(0):54-64.

74. Kim H-W, Kang K-M, Kwak H-Y, Kim JH. Preparation of supported Ni catalysts on various metal oxides with core/shell structures and their tests for the steam reforming of methane. Chem Eng J. 2011;168(2):775-83.

75. Ding C, Ai G, Zhang K, Yuan Q, Han Y, Ma X, et al. Coking resistant Ni/ZrO2@SiO2 catalyst for the partial oxidation of methane to synthesis gas. Int J Hydrogen Energy. 2015;40(21):6835-43.

76. Hajjaji N, Pons M-N, Houas A, Renaudin V. Exergy analysis: An efficient tool for understanding and improving hydrogen production via the steam methane reforming process. Energy Policy. 2012;42(0):392-9.

77. Gould TD, Izar A, Weimer AW, Falconer JL, Medlin JW. Stabilizing Ni Catalysts by Molecular Layer Deposition for Harsh, Dry Reforming Conditions. ACS Catal. 2014;4(8):2714-7.

78. Zheng X, Tan S, Dong L, Li S, Chen H. LaNiO3@SiO2 core–shell nano-particles for the dry reforming of CH4 in the dielectric barrier discharge plasma. Int J Hydrogen Energy. 2014;39(22):11360-7.

79. Kang K-M, Kim H-W, Shim I-W, Kwak H-Y. Catalytic test of supported Ni catalysts with core/shell structure for dry reforming of methane. Fuel Process Technol. 2011;92(6):1236-43.

80. Li Z, Mo L, Kathiraser Y, Kawi S. Yolk–Satellite–Shell Structured Ni–Yolk@Ni@SiO2 Nanocomposite: Superb Catalyst toward Methane CO2 Reforming Reaction. ACS Catal. 2014;4(5):1526-36.

81. Yang W, Liu H, Li Y, Zhang J, Wu H, He D. Properties of yolk–shell structured Ni@SiO2 nanocatalyst and its catalytic performance in carbon dioxide reforming of methane to syngas. Catal Today. 2016;259, Part 2:438-45.

82. Bharadwaj SS, Schmidt LD. Catalytic partial oxidation of natural gas to syngas. Fuel Process Technol. 1995;42(2–3):109-27.

83. Kim HW, Kang KM, Kwak H-Y. Preparation of supported Ni catalysts with a core/shell structure and their catalytic tests of partial oxidation of methane. Int J Hydrogen Energy. 2009;34(8):3351-9.

84. Li L, Yao Y, Sun B, Fei Z, Xia H, Zhao J, et al. Highly Active and Stable Lanthanum-doped Core–Shell-structured Ni@SiO2 Catalysts for the Partial Oxidation of Methane to Syngas. ChemCatChem. 2013;5(12):3781-7.

85. Matsuoka M, Kitano M, Takeuchi M, Tsujimaru K, Anpo M, Thomas JM. Photocatalysis for new energy production: Recent advances in photocatalytic water splitting reactions for hydrogen production. Catal Today. 2007;122(1–2):51-61.

86. Paramasivam I, Singh S, Moll M, Hauser C, Meyer K, Schmuki P. Photocatalysis vs. anodic-breakdown catalysis on TiO2 layers. Electrochim Acta. 2012;66(0):7-11.

87. Cui X, Jiang G, Zhu M, Zhao Z, Du L, Weng Y, et al. TiO2/CdS composite hollow spheres with controlled synthesis of platinum on the internal wall for the efficient hydrogen evolution. Int J Hydrogen Energy. 2013;38(22):9065-73.

88. Yang TC, Chang FC, Wang HP, Wei YL, Jou CJ. Photocatalytic splitting of seawater effected by (Ni–ZnO)@C nanoreactors. Mar Pollut Bull. 2014(0).

89. Kim HS, Kim D, Kwak BS, Han GB, Um M-H, Kang M. Synthesis of magnetically separable core@shell structured NiFe2O4@TiO2 nanomaterial and its

use for photocatalytic hydrogen production by methanol/water splitting. Chem Eng J. 2014;243(0):272-9.

90. Ismail AA, Bahnemann DW. Photochemical splitting of water for hydrogen production by photocatalysis: A review. Sol Energy Mater Sol Cells. 2014;128(0):85-101.

91. Li X, Liu J, Masters AF, Pareek VK, Maschmeyer T. Hollow micro/nanomaterials as nanoreactors for photocatalysis. APL Mater. 2013;1(4):-.

92. Wang D, Hisatomi T, Takata T, Pan C, Katayama M, Kubota J, et al. Core/Shell Photocatalyst with Spatially Separated Co-Catalysts for Efficient Reduction and Oxidation of Water. Angew Chem Int Ed. 2013;52(43):11252-6.

93. Hernández S, Cauda V, Hidalgo D, Farías Rivera V, Manfredi D, Chiodoni A, et al. Fast and low-cost synthesis of 1D ZnO–TiO2 core–shell nanoarrays: Characterization and enhanced photo-electrochemical performance for water splitting. J Alloys Compd. 2014;615, Supplement 1(0):S530-S7.

94. Lee I, Albiter MA, Zhang Q, Ge J, Yin Y, Zaera F. New nanostructured heterogeneous catalysts with increased selectivity and stability. PCCP. 2011;13(7):2449-56.

95. Wang Q, Hisatomi T, Ma SSK, Li Y, Domen K. Core/Shell Structured La- and Rh-Codoped SrTiO3 as a Hydrogen Evolution Photocatalyst in Z-Scheme Overall Water Splitting under Visible Light Irradiation. Chem Mater. 2014;26(14):4144-50.

96. Maeda K, Teramura K, Lu D, Saito N, Inoue Y, Domen K. Noble-Metal/Cr2O3 Core/Shell Nanoparticles as a Cocatalyst for Photocatalytic Overall Water Splitting. Angew Chem Int Ed. 2006;45(46):7806-9.

97. Pihosh Y, Turkevych I, Mawatari K, Fukuda N, Ohta R, Tosa M, et al. Ubiquitous element approach to plasmonic enhanced photocatalytic water splitting: the case of Ti@TiO 2 core-shell nanostructure. Nanotechnology. 2014;25(31):315402.

98. Wang M, Han J, Xiong H, Guo R. Yolk@Shell Nanoarchitecture of Au@r-GO/TiO2 Hybrids as Powerful Visible Light Photocatalysts. Langmuir. 2015;31(22):6220-8.

99. Li G, Zhang P, Bian Z, Zhu J, Wu L, Li H. Mesoporous TiN Microspheres with Hierarchical Chambers and Enhanced Visible Light-Driven Hydrogen Evolution. ChemSusChem. 2013;6(8):1461-6.

100. Zhang Q, Bai H, Zhang Q, Ma Q, Li Y, Wan C, et al. MoS2 yolk–shell microspheres with a hierarchical porous structure for efficient hydrogen evolution. Nano Res. 2016:1-10.

101. Liang B, Zhang N, Chen C, Liu X, Ma R, Tong S, et al. Hierarchical yolk-shell layered potassium niobate for tuned pH-dependent photocatalytic H2 evolution. Catal Sci Technol. 2017;7(4):1000-5.

102. Yu J, Wang K, Xiao W, Cheng B. Photocatalytic reduction of CO2 into hydrocarbon solar fuels over g-C3N4-Pt nanocomposite photocatalysts. PCCP. 2014;16(23):11492-501.

103. Das S, Wan Daud WMA. Photocatalytic CO2 transformation into fuel: A review on advances in photocatalyst and photoreactor. Renewable Sustainable Energy Rev. 2014;39(0):765-805.

104. Adachi K, Ohta K, Mizuno T. Photocatalytic reduction of carbon dioxide to hydrocarbon using copper-loaded titanium dioxide. Solar Energy. 1994;53(2):187-90.

105. de_Richter RK, Ming T, Caillol S. Fighting global warming by photocatalytic reduction of CO2 using giant photocatalytic reactors. Renewable Sustainable Energy Rev. 2013;19(0):82-106.

106. Baeissa ES. Green synthesis of methanol by photocatalytic reduction of CO2 under visible light using a graphene and tourmaline co-doped titania nanocomposites. Ceram Int. 2014;40(8, Part A):12431-8.

107. Tu W, Zhou Y, Li H, Li P, Zou Z. Au@TiO2 yolk-shell hollow spheres for plasmon-induced photocatalytic reduction of CO2 to solar fuel via a local electromagnetic field. Nanoscale. 2015;7(34):14232-6.

108. Zhai Q, Xie S, Fan W, Zhang Q, Wang Y, Deng W, et al. Photocatalytic Conversion of Carbon Dioxide with Water into Methane: Platinum and Copper(I) Oxide Co-catalysts with a Core–Shell Structure. Angew Chem Int Ed. 2013;52(22):5776-9.

109. Tsai C-W, Chen HM, Liu R-S, Asakura K, Chan T-S. Ni@NiO Core–Shell Structure-Modified Nitrogen-Doped InTaO4 for Solar-Driven Highly Efficient CO2 Reduction to Methanol. The Journal of Physical Chemistry C. 2011;115(20):10180-6.

110. Gui MM, Wong WMP, Chai S-P, Mohamed AR. One-pot synthesis of Ag-MWCNT@TiO2 core–shell nanocomposites for photocatalytic reduction of CO2 with water under visible light irradiation. Chem Eng J. 2014(0).

111. Liu S, Xia J, Yu J. Amine-Functionalized Titanate Nanosheet-Assembled Yolk@Shell Microspheres for Efficient Cocatalyst-Free Visible-Light Photocatalytic CO2 Reduction. ACS Appl Mater Interfaces. 2015;7(15):8166-75.

112. Wang W, Xu D, Cheng B, Yu J, Jiang C. Hybrid carbon@TiO2 hollow spheres with enhanced photocatalytic CO2 reduction activity. J Mater Chem A. 2017.

113. Wang X, Liao M, Zhong Y, Zheng JY, Tian W, Zhai T, et al. ZnO Hollow Spheres with Double-Yolk Egg Structure for High-Performance Photocatalysts and Photodetectors. Adv Mater. 2012;24(25):3421-5.

114. Jiang Z, Wei W, Mao D, Chen C, Shi Y, Lv X, et al. Silver-loaded nitrogen-doped yolk-shell mesoporous TiO2 hollow microspheres with enhanced visible light photocatalytic activity. Nanoscale. 2015;7(2):784-97.

115. Li J, Liu X, Sun Z, Sun Y, Pan L. Novel yolk–shell structure bismuth-rich bismuth molybdate microspheres for enhanced visible light photocatalysis. J Colloid Interface Sci. 2015;452:109-15.

116. Zhou J, Xu L, Sun J, He D, Jiao H. Yolk–shell Au@CeO2 microspheres: Synthesis and application in the photocatalytic degradation of methylene blue dye. Surf Coat Technol. 2015;271:119-26.

117. Chen L, Li L, Wang T, Zhang L, Xing S, Wang C, et al. A novel strategy to fabricate multifunctional Fe3O4@C@TiO2 yolk-shell structures as magnetically recyclable photocatalysts. Nanoscale. 2014;6(12):6603-8.

118. Joo JB, Liu H, Lee YJ, Dahl M, Yu H, Zaera F, et al. Tailored synthesis of C@TiO2 yolk–shell nanostructures for highly efficient photocatalysis. Catal Today. 2016;264:261-9.

119. Zhao Y, Tao C, Xiao G, Wei G, Li L, Liu C, et al. Controlled synthesis and photocatalysis of sea urchin-like Fe3O4@TiO2@Ag nanocomposites. Nanoscale. 2016;8(9):5313-26.

120. Tang J, Liu J, Torad NL, Kimura T, Yamauchi Y. Tailored design of functional nanoporous carbon materials toward fuel cell applications. Nano Today. 2014(0).

121. Zhang H, Wang H, Eid K, Wang L. Nanoparticle in Nanocage: Au@Porous Pt Yolk-Shell Nanoelectrocatalysts. Part Part Syst Charact. 2015;32(9):863-8.

122. Gu L, Jiang L, Jin J, Liu J, Sun G. Yolk–shell structured iron carbide/N-doped carbon composite as highly efficient and stable oxygen reduction reaction electrocatalyst. Carbon. 2015;82(0):572-8.

123. Selvakumar K, Senthil Kumar SM, Thangamuthu R, Kruthika G, Murugan P. Development of shape-engineered α-MnO2 materials as bi-functional catalysts for oxygen evolution reaction and oxygen reduction reaction in alkaline medium. Int J Hydrogen Energy. 2014;39(36):21024-36.

124. Xiao J, Chen C, Xi J, Xu Y, Xiao F, Wang S, et al. Core-shell Co@Co3O4 nanoparticle-embedded bamboo-like nitrogen-doped carbon nanotubes (BNCNTs) as a highly active electrocatalyst for the oxygen reduction reaction. Nanoscale. 2015;7(16):7056-64.

125. Liu J, Su F, Guo W, Tian X, Zhao XS, Zhou Z. Template Approaches to Preparing Porous Carbon. Chemistry & Physics of Carbon. Chemistry and Physics of Carbon: CRC Press; 2007. p. 63-128.

126. Kuai L, Wang S, Geng B. Gold-platinum yolk-shell structure: a facile galvanic displacement synthesis and highly active electrocatalytic properties for methanol oxidation with super CO-tolerance. Chem Commun. 2011;47(21):6093-5.

127. Ye S-H, He X-J, Ding L-X, Pan Z-W, Tong Y-X, Wu M, et al. Cu2O template synthesis of high-performance PtCu alloy yolk-shell cube catalysts for direct methanol fuel cells. Chem Commun. 2014;50(82):12337-40.

128. Long NV, Yang Y, Minh Thi C, Minh NV, Cao Y, Nogami M. The development of mixture, alloy, and core-shell nanocatalysts with nanomaterial supports for energy conversion in low-temperature fuel cells. Nano Energy. 2013;2(5):636-76.

129. Huang Y, Liu Y, Yang Z, Jia J, Li X, Luo Y, et al. Synthesis of yolk/shell Fe3O4–polydopamine–graphene–Pt nanocomposite with high electrocatalytic activity for fuel cells. J Power Sources. 2014;246(0):868-75.

130. Li X, Liu G, Popov BN. Activity and stability of non-precious metal catalysts for oxygen reduction in acid and alkaline electrolytes. J Power Sources. 2010;195(19):6373-8.

131. Shi Q, Zhang P, Li Y, Xia H, Wang D, Tao X. Synthesis of open-mouthed, yolk-shell Au@AgPd nanoparticles with access to interior surfaces for enhanced electrocatalysis. Chem Sci. 2015;6(7):4350-7.

132. Ye Y, Kuai L, Geng B. A template-free route to a Fe3O4-Co3O4 yolk-shell nanostructure as a noble-metal free electrocatalyst for ORR in alkaline media. J Mater Chem. 2012;22(36):19132-8.

133. Lu Y, Jiang Y, Gao X, Wang X, Chen W. Highly Active and Durable PdAg@Pd Core–Shell Nanoparticles as Fuel-Cell Electrocatalysts for the Oxygen Reduction Reaction. Part Part Syst Charact. 2016;33(8):560-8.

134. Hu H, Guan B, Xia B, Lou XW. Designed Formation of Co3O4/NiCo2O4 Double-Shelled Nanocages with Enhanced Pseudocapacitive and Electrocatalytic Properties. J Am Chem Soc. 2015;137(16):5590-5.

135. Hu H, Han L, Yu M, Wang Z, Lou XW. Metal-organic-framework-engaged formation of Co nanoparticle-embedded carbon@Co9S8 double-shelled nanocages for efficient oxygen reduction. Energy Environ Sci. 2016;9(1):107-11.

136. Chao S, Cui Q, Wang K, Bai Z, Yang L, Qiao J. Template-free synthesis of hierarchical yolk-shell Co and N codoped porous carbon microspheres with enhanced performance for oxygen reduction reaction. J Power Sources. 2015;288:128-35.

137. Bie S, Zhu Y, Su J, Jin C, Liu S, Yang R, et al. One-pot fabrication of yolk-shell structured La0.9Sr0.1CoO3 perovskite microspheres with enhanced catalytic activities for oxygen reduction and evolution reactions. J Mater Chem A. 2015;3(44):22448-53.

138. Zheng X, Cao X, Wu J, Tian J, Jin C, Yang R. Yolk-shell N/P/B ternary-doped biocarbon derived from yeast cells for enhanced oxygen reduction reaction. Carbon. 2016;107:907-16.

139. Yin Z, Zhu C, Li C, Zhang S, Zhang X, Chen Y. Hierarchical nickel-cobalt phosphide yolk-shell spheres as highly active and stable bifunctional electrocatalysts for overall water splitting. Nanoscale. 2016;8(45):19129-38.

140. Tian H, Wang S, Zhang C, Veder J-P, Pan J, Jaroniec M, et al. Design and synthesis of porous ZnTiO3/TiO2 nanocages with heterojunctions for enhanced photocatalytic H2 production. J Mater Chem A. 2017;5(23):11615-22.

141. Hao Y, Jiao X, Zou H, Yang Hq, Liu J. Growing a Hydrophilic Nanoporous Shell on a Hydrophobic Catalyst Interface for Aqueous Reactions with High Reaction Efficiency and in situ Catalyst Recycling. J Mater Chem A. 2017;5(31):16162-70.

142. Wang Z, Liu Y, Yang T, Deng J, Xie S, Dai H. Catalytic performance of cobalt oxide-supported gold-palladium nanocatalysts for the removal of toluene and o-xylene. Chinese Journal of Catalysis. 2017;38(2):207-16.

143. Mortazavi-Derazkola S, Salavati-Niasari M, Amiri O, Abbasi A. Fabrication and characterization of Fe3O4@SiO2@TiO2@Ho nanostructures as a novel and highly efficient photocatalyst for degradation of organic pollution. Journal of Energy Chemistry. 2017;26(1):17-23.

Chapter 3: Brush-like copper oxide encapsulated within mesoporous silica shell yolk-shell nanoparticles

Abstract

Copper oxide (CuO), Resorcinol-formaldehyde (RF) and Silica (SiO_2) are selected as the materials for studying effects of synthetic parameters in fabricating yolk-shell structured nanoparticles. A basic selective etching method via calcination is employed to create the final product using RF as the sacrificing template. Calcination temperature and shell thickness are proved having significant impacts in resulting a successful yolk-shell structure. Such study is believed to lead a good understanding of design yolk-shell particle synthesis method at the beginning of research study.

3.1 Introduction

The investigation of yolk-shell structured nanocatalyst is dominating the current research direction in nanoparticle synthesis due to its advantageous and versatile catalytic possibility for various applications. As mentioned in the Chapter 2, although yolk-shell structure has many merits, the difficulty in synthesizing challenges the progress of such catalysts being produced commercially. Most of synthesis methods for fabricating yolk-shell structure involve hazardous chemicals or harsh reaction environment resulting economic and environmental infeasibility. Therefore, it has put great hope in designing a facile and cheap synthesis method to produce high quality yolk-shell structured nanocatalysts.

Copper oxides (CuO), P-type semiconductor, is one of the many popular transition metal oxides owning an excellent ability in activing oxygen molecules for fuel cell reactions, electrochemical CO_2 reduction reactions and also photocatalytic reactions; it stand out by the advantages of natural abundant and low in cost (1-6). Copper is a polyvalent metal, apart from CuO, cuprous oxide (Cu_2O) is also one of the favourite materials and intensively involved in solar energy conversion applications (1, 7), also because its polyvalent ability, the transformation between CuO and Cu_2O is reversible, and CuO is usually as the base template for fabricating Cu_2O or Cu nanocatalysts. Selecting a right shell material is as important a suitable active yolk. The shell of a well-designed yolk-shell nanoparticle contributes an important part of resulting good catalytic activity. Inorganic or polymer materials are usually the

common ones, and among them silica and carbon are the most popular due to their high biocompatibility, simple functionality, easy to synthesize and rich resources (8-11). Shell provides protection to active yolk from deactivation and aggregation while allowing a sufficient accessibility for reactants and products flow in and out. With the advancement of yolk-shell nanoparticle design, recently, more and more functionalized shell with active yolk catalysts have been produced to carry out cascade catalytic reactions.

This chapter presents a practice to fabricate CuO@mSiO_2 yolk-shell nanoparticles via some of the most basic methods as a study to understand the principles behind yolk-shell structured creation and how the synthetic parameters could affect the formation of yolk-shell structure. It is believed to be invaluable for the prospective research works later on. Here, CuO@mSiO_2 yolk-shell particles were prepared by removing Resorcinol-Formaldehyde (RF) templates under gentle calcination in air while removing pore-directing reagents to form mesoporous silica shell, as shown in Scheme 3.1.

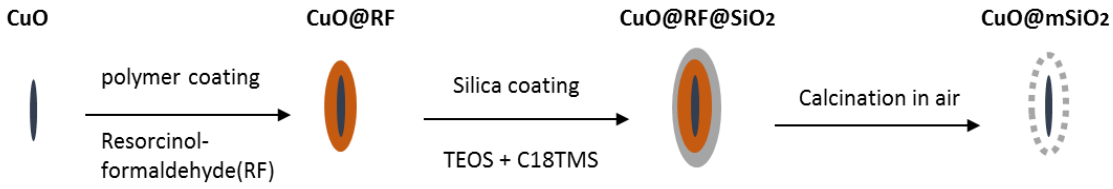

Scheme 3.1: Schematic illustration of synthesis of CuO@mSiO_2 yolk-shell particles.

3.2 Materials and Methods

3.2.1 Chemicals and reagents

Copper (II) nitrate trihydrate (98%-103%), Polyvinylpyrolidone PVP-40 (MW=40000), formaldehyde (36.5%-38%), Tetraethylortosilicate TEOS (98%), Trimethoxy(octadecyl)silane C18TMS (90%) were purchased from Sigma-Aldrich and used as supplied. Cetyltrimethylammonium bromide CTAB solution (0.1M in D.I water) was made by using Cetyltrimethylammonium bromide CTAB (≥99%) purchased from Sigma-Aldrich as well. Sodium hydroxide NaOH solution (1M in D.I water) was made by using pure sodium hydroxide anhydrous purchased from Chem-supply PTY LTD Ammonia solution (25%) was purchased from VWR

International PTY LTD. Water was purified by a Milli Q system and had an electrical resistance of 18 MΩ•cm.

3.2.2 Preparation of copper oxide nanoparticles

10 mL of CTAB solution (in water, 0.1 M) and 0.25 g of PVP-40 were dissolved in 100 mL alcohol solution (water/ethanol V/V=7/3) before 0.1 mole of copper (II) nitrate trihydrate was added into the clear solution, which was placed in a water bath at 80 °C and stirred magnetically at 500 rpm. After 5 min stirring, 3.8 mL of 1 M NaOH solution was injected into the mixture, which was kept stirring for 2 h before it was removed from the water bath.

3.2.3 Preparation of copper oxide nanoparticles with resorcinol-formaldehyde coating CuO@RF

30 mL of absolute ethanol was added into as-synthesised CuO colloid solution in order to make up the ethanol loss during the previous reaction at 80 °C. Then, the colloid solution underwent ultrasonic treatment for 20 min before being placed back onto magnetic stirring heating plate, and then 0.25 mL of ammonia solution and 0.264 g of resorcinol were added to the solution. Subsequently, after 30 min stirring, 0.375 mL of formaldehyde was added into the mixture, which was kept stirring at 35 °C and 500 rpm. After 20 h, the produced CuO@RF core-shell particles were centrifuged and washed with water and ethanol solutions before being dried at 75 °C for at least 10 h in an electrical oven.

3.2.4 Preparation of CuO@RF coated with silica shell to form CuO@RF@SiO_2 double-shell core-shell nanoparticles

Washed precipitates from previous step were dispersed into 63.4 ml absolute ethanol with 20 ml D.I water mixture, and 20 min ultrasonic treatment was carried out to ensure well dispersion of CuO@RF nanoparticles. Then, 2ml of CTAB solution (in water, 0.1M) was added into colloid solution while it was stirring magnetically at 600 rpm and at room temperature. 0.6 ml of ammonia solution and mixture of 0.3 ml TEOS with 0.15 ml C_{18}TMS were put into colloid solution to deposit silica coating outside RF shell. After 2 hour stirring, products were centrifuged and washed with ethanol and water three times before drying in an electrical oven at 75°C for at least 12 hours.

3.2.5 Synthesis of CuO@meso-SiO_2 yolk-shell nanoparticles

Dried CuO@RF@SiO_2 nanoparticles were calcined at 450°C for 5 hours under air with temperature increment at 5°C/min in order to remove RF layer and C_{18}TMS structure directing agent completely and forming copper oxide at mesoporous silica shell yolk-shell structured nanoparticles.

3.2.6 Characterization

The characterizations of samples were conducted using transmission electron microscope (TEM, FEI Titan G2 80-200 TEM/STEM with ChemiSTEM Technology) and scanning electron microscope (SEM, Zeiss Neon). In addition, High Angle Annular Dark Field Scanning Transmission Electron Microscopy (HAADF-STEM) imaging and Energy-dispersive X-ray spectroscopy element mapping were also carried out using TEM (FEI Titan G2 80-200 TEM/STEM with ChemiSTEM Technology) with operating voltage at 200 kV. The preparation for SEM and TEM measurements was to suspend sample powders in absolute ethanol and undergo at least 20 min ultrasonic treatment, then dropped such suspension onto Aluminium Stub and carbon coated copper grip, respectively. Moreover, in regard to the elemental analysis, Energy-dispersive X-ray spectroscopy element mapping operation condition on FEI Titan was with a probe size approximately 1nm probe current at about 0.4nA. The nitrogen adsorption and desorption isotherms were obtained from sample testing on Micromeritics Tristar II Surface Area and Porosity Analyser. The measurements of particles surface areas were calculated using Brunauer-Emmett-Teller (BET) method from nitrogen adsorption isotherms within relative pressure range of 0.05 – 0.20, and pore sizes and total pore volumes were calculated using Nonlocal Density Functional Theory (NLDFT) method based on the amount of nitrogen adsorbed at relative pressure at 0.99. In additional, prior to nitrogen-sorption measurements, samples were degassed at 200°C for at least 12 hours. XRD measurements were obtained using a Bruker-AXS D8 Advance Diffractometer with Cu Kα radiation (40 KV, 40 mA) and a LynxEye position sensitive detector. Information on crystalline phases was confirmed against the database of JCPDS files.

3.3 Results and Discussion

3.3.1 Synthesis of CuO@RF particles

As illustrated in Scheme 3.1, template particles, copper oxide (CuO), were synthesised through a chemical reaction between copper (II) nitrate trihydrate and sodium hydroxide. A clear blue copper precursor solution changed to black immediately after sodium hydroxide (NaOH) solution was added, indicating the instant formation of copper oxide particles. The sodium hydroxide to copper ion ratio (NaOH/ Cu2+) at 1.9 was designed to be slightly less than stoichiometric ratio 2 in order to minimize aggregation, as increase in pH could result decline of surface charge of oxide nanoparticles to form large assemblages (12). Moreover, cetyltrimethylammonium bromide (CTAB) and polyvinylpyrolidone (PVP-40) were used as double capping agents to protect the products from severe aggregation (13). As shown in Figure 3.1(a), TEM image shows the brush like copper oxide templates with a length of approximately 170 - 220 nm and diameter/width around 50 nm. The majority of the particles are relatively uniform in size, with a small percentage of particles having lengths less than 100 nm. Figure 3.1(b) clearly depicts the polymer RF layer (about 30 nm thick) deposited outside the copper oxide particle and SEM image (Figure 3.1(c)) provides the surface morphology of CuO@RF particles. HAADF-STEM imaging and EDS mapping (Figure 3.1(d)) confirm the elemental composition of the CuO@RF particles.

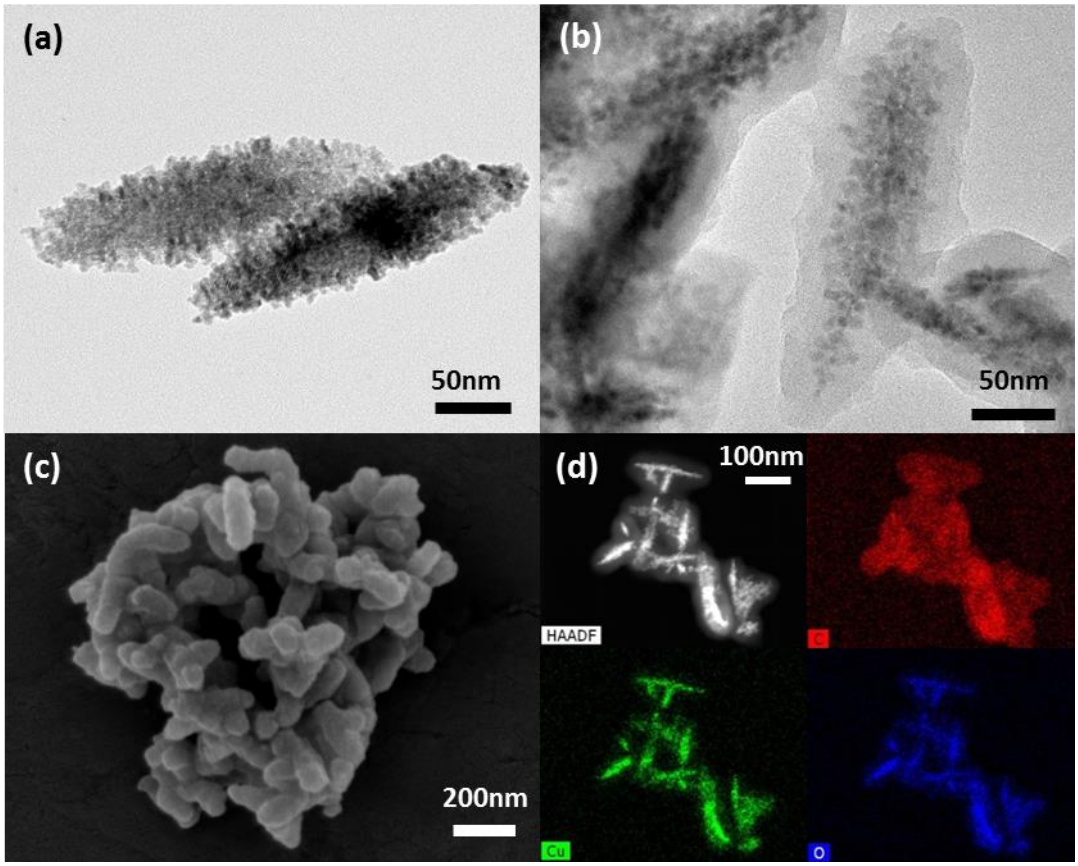

Figure 3.1: a) TEM image of brush like CuO particles; (b) TEM image of CuO@RF core-shell particles; (c) SEM image of CuO@RF core-shell particles; (d) STEM image and EDS mapping of CuO@RF core-shell particles.

TEM image in Figure 3.2 (a) show that some of CuO@RF particles possess multi-core with a single shell structure (Figure 3.2), suggesting the RF shell grew outside the inter-connected CuO templates. This phenomenon typically happened to the smaller sized CuO particles. However, such a problem might be solved by reducing the mass of CuO templates and increasing the volume of solvent during the RF coating process. It can be clearly seen that copper and oxygen are present in the brush like templates, and the polymer shell formed outside metal oxide. XRD pattern (Figure 3.2 (b)) further confirmed that CuO was the only crystalline compound existing in the CuO@RF samples. During the fine tuning process of CuO@RF fabrication, CTAB and PVP-40 were proved to have a great impact on the formation of CuO particles in terms of morphology. With lower amounts of CTAB and PVP-40 added into solution, the CuO particles changed to smooth, long and narrow wire-like shape, as shown in Figure 3.2 (c) and (d), and reduction in capping agent concentrations resulted in very severe aggregation of the particles.

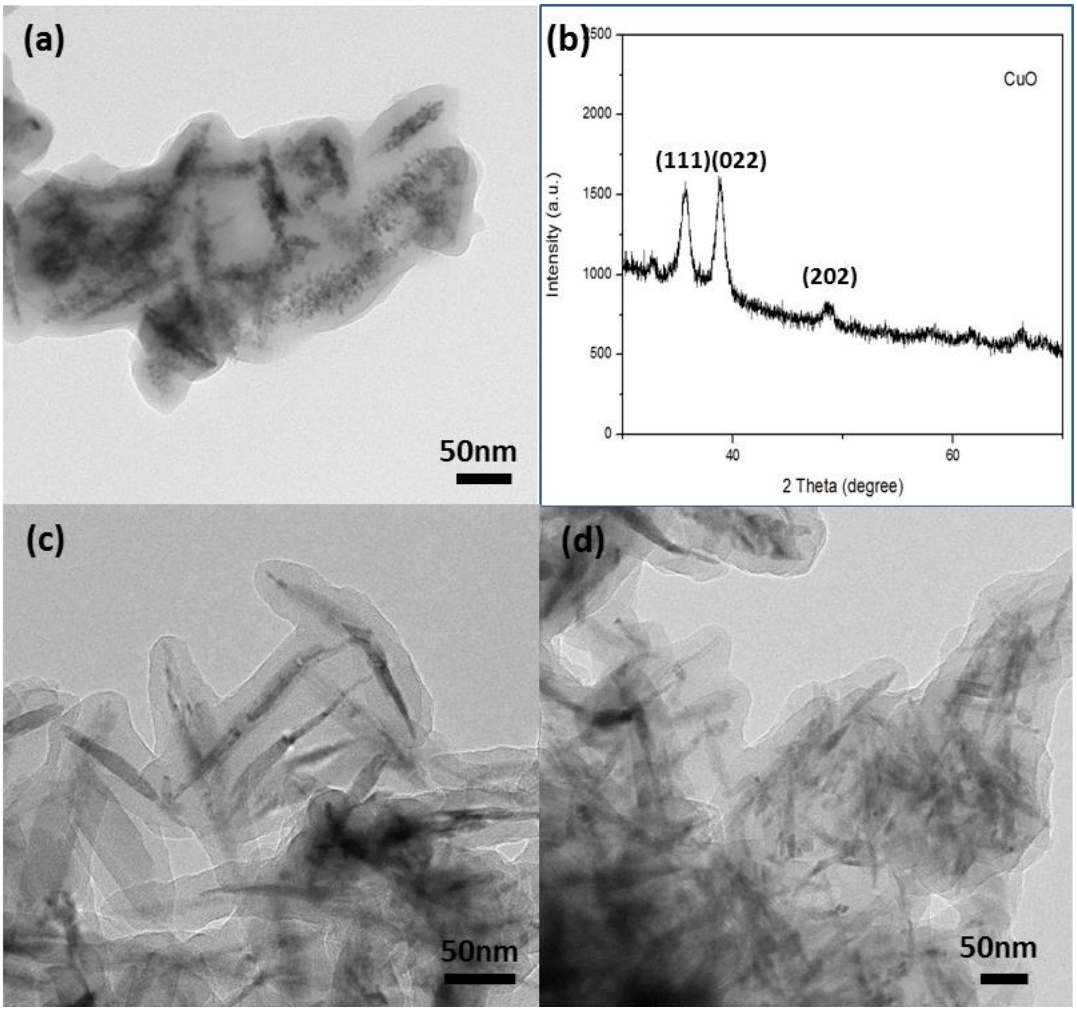

Figure 3.2: (a): TEM image of CuO@RF particle aggregate; (b) XRD pattern of CuO@RF particles; (c) and (d): TEM images of CuO@RF core-shell particles which CuO formed with less amounts of CTAB and PVP-40.

3.3.2 Synthesis of CuO@RF@SiO_2 double shell particles and CuO@mSiO_2 yolk-shell particles

CuO@RF particles were further coated with a layer of SiO_2 via surface templating sol-gel process, and C_{18}TMS was selected as structure directing agent to create porous silica shell with hierarchical pore sizes (14). The TEM and SEM images in Figure 3.3 show the interior and exterior morphologies of CuO@RF@SiO_2 double shell particles. As RF and SiO_2 layers have similar chemical property, there is no obvious layer boundary showing in the TEM image (Figure 3.3 (a)). However, the successful deposition of SiO_2 layer could be seen by the increase thickness of shell and the roughness at the shell surface in compare to the particles before silica coating. Moreover, silica tends to form silica spheres when excess silica precursor is added,

as shown in Figure 3.3 (b). Therefore, controlling the precursor amount is one of the critical factors for fabricating a good yolk-shell nanoparticle, thick shell could decrease the accessibility of reactants in contact with active yolk within shell, thin shell may break during calcination at high temperature, and forming of excessive silica spheres could lower the active metal loading percentage in a unit mass.

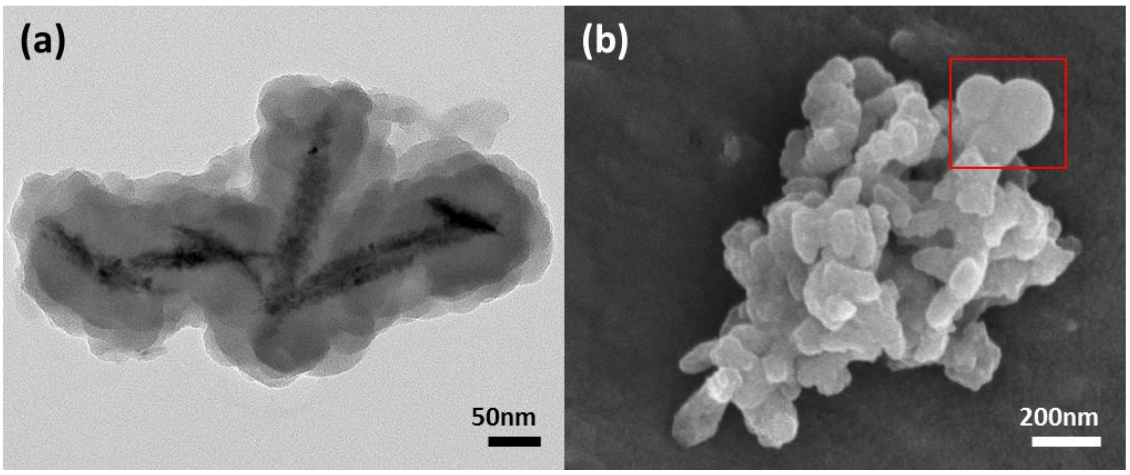

Figure 3.3: (a) TEM image of CuO@RF@SiO_2 double shell particles; (b) SEM image of CuO@RF@SiO_2 double shell particles.

To remove the RF templates and pore-directing reagents, CuO@RF@SiO_2 particles were calcined at 450°C under air. The TEM image in Figure 3.4 (a) clearly shows that RF template had been removed completely forming void in between CuO yolk and SiO_2 shell, and CuO yolk remained brush-like structure. The SiO_2 shell thickness is approximately 40 nm. The compositional information of such sample was confirmed by XRD measurement (Figure 3.4 (b)); only CuO peaks appear in the XRD proving the unchanged composition. BET measurements were carried out to identify the porous structure and calculate the surface area of CuO@mSiO_2 yolk-shell particles. The adsorption-desorption isotherm in Figure 3.4 (c) indicates a type IV adsorption-desorption hysteresis, exhibiting the presence of well-defined mesopores. The sharp pore size distribution diagram (Figure 3.4 (d)) also proving the existence of well-defined mesopores. Base on the calculation of adsorption branch of nitrogen isotherm with BJH method, the pore size is 4.1 nm, and surface area of samples is 616.2 m^2/g.

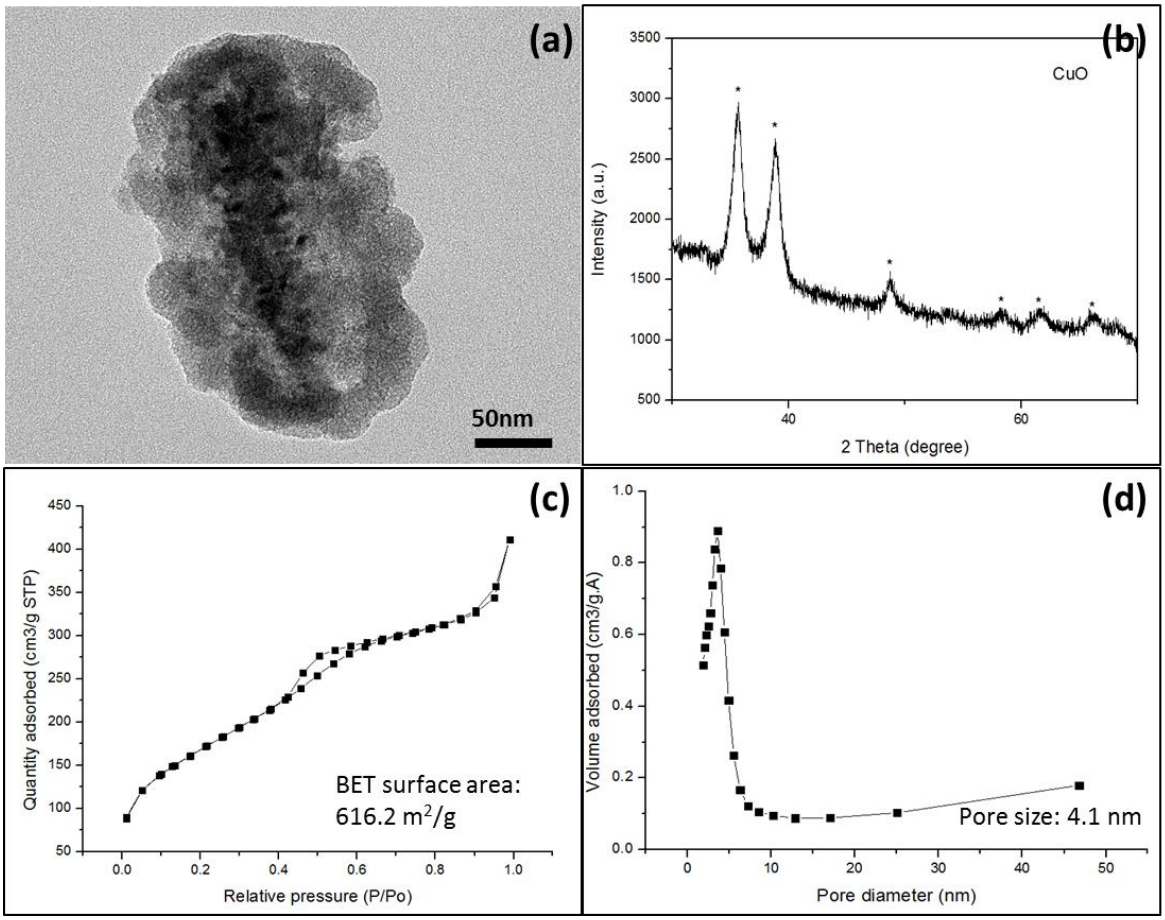

Figure 3.4: (a) TEM image of $CuO@mSiO_2$ yolk-shell particle; (b) XRD measurement of $CuO@mSiO_2$ yolk-shell particles; (c) Adsorption and desorption isotherm of $CuO@mSiO_2$ yolk-shell particles; (d) Pore size distribution of $CuO@mSiO_2$ yolk-shell particles.

To further investigate the synthetic effect of calcination temperature, a testing of annealing temperature at 550°C was conducted. In contrast with 450°C, the brush-like CuO yolk deformed into tiny spherical nanoparticles, as seen in Figure 3.5 (a). Therefore, it could be said that brush-like yolk is formed by tiny CuO clusters, and higher temperature break the connection resulting scattered CuO nanoparticles within mesoporous silica shell. Moreover, silica shell thickness also plays an important role in forming yolk-shell structure. As seen in Figure 3.5 (b), by reducing 50% of silica precursor amount, silica shell shrinks after removing RF template leaving no visible void between shell and core; and such thin shell also breaks when mesopores forms after calcination, the thickness is not sufficient to support itself resulting broken shell and core-shell structure particles.

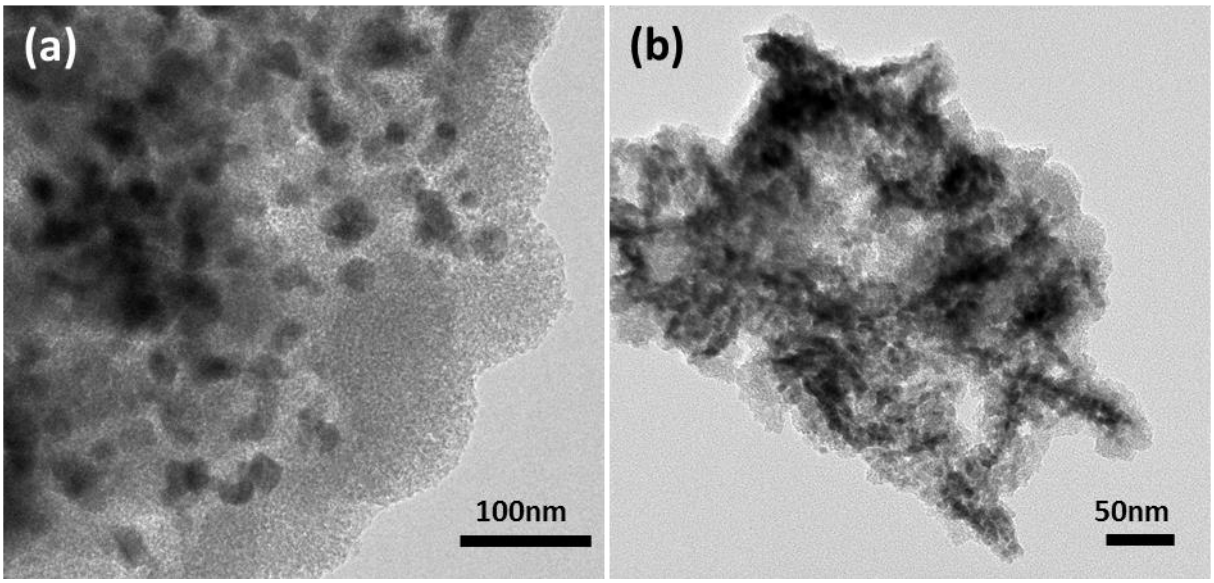

Figure 3.5: (a) TEM image of CuO-mSiO_2 yolk-shell sample calcined under higher temperature under air; (b) TEM image of CuO@mSiO_2 yolk-shell sample with thinner SiO2 shell.

3.4 Conclusion

Brush-like CuO yolk SiO2 mesoporous shell yolk-shell particle were prepared via facile synthesis method using RF as sacrificing template and C_{18}TMS as pore-directing reagent. Copper (II) nitrate trihydrate was chosen as the copper precursor and CuO formed by mixing with common alkaline NaOH solution. Copping agents, CTAB and PVP, not only help in preventing aggregation of CuO nanoparticles, they also have significant influence on the structure and size of CuO nanoparticles. A uniform layer of RF was deposited outside brush-like CuO nanoparticles before coating SiO_2 layer forming core-double shell particles. Calcination under air flow resulted yolk-shell structure and also mesoporous silica shell. Both calcination temperature and thickness of SiO_2 possess great impact on forming brush-like CuO yolk SiO2 mesoporous shell yolk-shell particle. This study gives a good understanding in synthesizing yolk-shell structure nanoparticles and will lead to more creative design of synthesis method in the following chapters.

References

1. Andana T, Piumetti M, Bensaid S, Veyre L, Thieuleux C, Russo N, et al. CuO nanoparticles supported by ceria for NOx-assisted soot oxidation: insight into catalytic activity and sintering. Appl Catal, B. 2017;216:41-58.

2. Tang Y, Liu Q, Jiang Z, Yang X, Wei M, Zhang M. Nonenzymatic glucose sensor based on icosahedron AuPd@CuO core shell nanoparticles and MWCNT. Sensors and Actuators B: Chemical. 2017;251:1096-103.

3. Elbasuney S, Gaber Zaky M, Radwan M, Mostafa SF. Stabilized super-thermite colloids: A new generation of advanced highly energetic materials. Appl Surf Sci. 2017;419:328-36.

4. Jiang L-C, Zhang W-D. A highly sensitive nonenzymatic glucose sensor based on CuO nanoparticles-modified carbon nanotube electrode. Biosens Bioelectron. 2010;25(6):1402-7.

5. Wang H, Xu J-Z, Zhu J-J, Chen H-Y. Preparation of CuO nanoparticles by microwave irradiation. J Cryst Growth. 2002;244(1):88-94.

6. Chang Y, Teo JJ, Zeng HC. Formation of Colloidal CuO Nanocrystallites and Their Spherical Aggregation and Reductive Transformation to Hollow Cu2O Nanospheres. Langmuir. 2005;21(3):1074-9.

7. Yin M, Wu C-K, Lou Y, Burda C, Koberstein JT, Zhu Y, et al. Copper Oxide Nanocrystals. J Am Chem Soc. 2005;127(26):9506-11.

8. Priebe M, Fromm KM. Nanorattles or Yolk–Shell Nanoparticles—What Are They, How Are They Made, and What Are They Good For? Chem Eur J. 2015;21(10):3854-74.

9. Liu J, Qiao SZ, Chen JS, Lou XW, Xing X, Lu GQ. Yolk/shell nanoparticles: new platforms for nanoreactors, drug delivery and lithium-ion batteries. Chem Commun. 2011;47(47):12578-91.

10. Jankiewicz BJ, Jamiola D, Choma J, Jaroniec M. Silica–metal core–shell nanostructures. Adv Colloid Interface Sci. 2012;170(1–2):28-47.

11. Jin R, Yang Y, Zou Y, Liu X, Xing Y. A General Route to Hollow Mesoporous Rare-Earth Silicate Nanospheres as a Catalyst Support. Chem Eur J. 2014;20(8):2344-51.

12. Kobayashi Y, Abe Y, Maeda T, Yasuda Y, Morita T. A metal–metal bonding process using metallic copper nanoparticles produced by reduction of copper oxide nanoparticles. Journal of Materials Research and Technology. 2014;3(2):114-21.

13. Deng D, Cheng Y, Jin Y, Qi T, Xiao F. Antioxidative effect of lactic acid-stabilized copper nanoparticles prepared in aqueous solution. J Mater Chem. 2012;22(45):23989-95.

14. Chen Y, Chen H, Ma M, Chen F, Guo L, Zhang L, et al. Double mesoporous silica shelled spherical/ellipsoidal nanostructures: Synthesis and hydrophilic/hydrophobic anticancer drug delivery. J Mater Chem. 2011;21(14):5290-8.

Chapter 4: Yolk-shell structured Fe@ɣ-Fe_2O_3 nanoparticles loaded graphitic porous carbon for efficient oxygen reduction reaction

Abstract

Core-shell Cu/ɣ-Fe_2O_3@C and yolk-shell structured Cu/Fe@ɣ-Fe_2O_3@C particles have been prepared by a facile synthesis method using copper oxide (CuO) as template particles, resorcinol-formaldehyde (RF) as the carbon precursor and iron nitrate solution as the iron source via pyrolysis. With increasing carbonization temperature and time, solid ɣ-Fe_2O_3 cores were formed and then transformed into Fe@ɣ-Fe_2O_3 yolk-shell structured particles via Ostwald ripening under nitrogen gas flow. The composition variations are studied and the formation mechanism is proposed for the generation of the hollow and yolk-shell structured metal and metal oxides. Moreover, highly graphitic carbons can be obtained by etching the metal and metal oxide nanoparticles through an acid treatment. The electrocatalytic activity for oxygen reduction reaction (ORR) is investigated on Cu/ɣ-Fe_2O_3@C, Cu/Fe@ɣ-Fe_2O_3@C and graphitic carbons, indicating comparable or even superior performance to other Fe-based nanocatalysts.

4.1 Introduction

Development of new energy materials for efficient energy storage and conversion has attracted intensive attentions in the last decade. It is urgently seeking more sustainable and efficient energy options to meet the ever-increasing demand due to the severe environmental consequences of traditional combustion of fossil fuels and the depletion of these resources. Renewable energy has the potential to replace conventional fuels but still faces challenges such as low efficiency, high capital and maintenance costs and environmental dependent behaviour. Therefore, scientists and engineers are beginning to concentrate their attention to clean energy production and utilisation.

Fuel cells, one of the main streams in clean energy devices, convert chemicals into electrical energy which is believed to have a significant contribution in sustainable energy conversions. The oxygen reduction reaction (ORR), a crucial cathode reaction in a fuel cell system, has sluggish kinetic behaviour in nature which diminishes the

energy converting efficiency (1-8). Thus, seeking cheaper, efficient and durable catalysts has become the major goal for ORR. Nano-scaled catalysts are more favourable than those in micro-size range as the nanocatalysts possess some advantages in larger surface area to volume ratio and longer lifespan. So far, Pt-based electrocatalysts are the most effective nanocatalysts for ORR, serving as a reference for positing the performance of other electrocatalysts. However, due to the poor catalytic durability, high cost and scarcity of Pt resources, an ultimate goal has been set to investigate abundant and cheap alternatives with a better catalytic stability (1-4, 7-18). Therefore, enormous research efforts have been dedicated to synthesizing non-precious metal catalysts. Iron and cobalt based carbon particles and metal free nitrogen doped carbon materials are dominating the investigation in efficient ORR catalysts. Examples of these systems which possess excellent performance towards ORR include Fe_3C@nitrogen-doped vesicle-like graphitized carbon (2), nitrogen and phosphorus doped carbon nanotube and graphene hybrid nanopsheres (1), Fe_3O_4/N-doped mesoporous carbon spheres (13), sheet like Fe−N/C (18), Fe/N co-doped graphitic carbon (19), and Co nanoparticle-embedded carbon@Co_9S_8 rattle type double-shelled nanocages (20). Moreover, modified metal free carbon based materials, through either structural design or incorporation of doping heteroatoms, have also attracted much attention as potential electrochemical catalysts for fuel cell applications (16, 21-23).

Maghemite (ɣ-Fe_2O_3), one of the most common forms of iron oxide besides magnetite (Fe_3O_4) and hematite (α-Fe_2O_3) exists in nature (24), is the allotropic form of Fe_3O_4 possessing either a cubic or tetragonal crystal structure with 1/6 of the positions of interstices unoccupied by Fe^{3+} ions. It has an excellent ability in accelerating electron movement and increasing the catalytic active sites for electrochemical reactions (25, 26). Iron oxides are transition metal oxides with good natural abundance, low toxicity, chemical inertness and biocompatibility (24, 27, 28). ɣ-Fe_2O_3 has a high theoretical capacity of 1007 mA h g^{-1} and is widely used as anode electrocatalysts for lithium-ion batteries.(26, 28-31) Recently, increasing attention on ɣ-Fe_2O_3 has made this material the target of extensive investigations for many other applications, such as supercapacitors and ORR. With the advancement of research in complex structural nanoparticles, ɣ-Fe_2O_3 as the active site is more likely to be encapsulated within a protection shell forming core-shell or yolk-shell nanocatalysts.

At the same time, the functional shell could help in enhancing catalytic activity and stability.

Core-shell and yolk-shell structured nanoparticles are very popular nanostructures, providing unique properties to improve the performance. From the catalytic perspective, these nanoparticles possess many characteristic merits such as tunable physical and chemical properties of core and shell, and a protective shell preventing the aggregation and deactivation of active core/cores (32-34). Despite the investigation of the most suitable materials for specific catalytic reactions, structural design of nanocatalysts is believed to be one of the most effective ways to improve the catalytic ability and stability. However, it is very challenging to synthesise complex structural nanoparticles, especially yolk-shell structured metal oxides. Generally, fabrication of yolk-shelled metal oxide nanoparticles involves multiple steps and often uses a combination of multiple synthesis methods. Hard templating is the most common method for creating yolk-shell structures, however, it also has distinctive drawbacks as a requisite step is needed to remove the templates, which always uses calcination in air or hazardous chemicals, and the removal step often causes a damage to the nanoparticles to some extent (35). Therefore, a facile and "green" process is highly desired to fabricate metal oxide yolk-shell nanoparticles.

In this chapter, we present a facile approach to synthesise core-shell Cu/ɣ-Fe_2O_3@C and yolk-shell structured Cu/Fe@ɣ-Fe_2O_3@C particles having multiple ɣ-Fe_2O_3 or Fe@ɣ-Fe_2O_3 and Cu nanocores encapsulated within a graphitic nanoporous carbon shell as a low cost catalyst for ORR. Metal free graphitic nanoporous carbons can be obtained by etching of the metal and metal oxides (Scheme 4.1). Moreover, we propose a possible formation mechanism of the particles from solid ɣ-Fe_2O_3 to hollow ɣ-Fe_2O_3 then to yolk-shell Fe@ɣ-Fe_2O_3 and finally solid Fe nanoparticles. The ORR activity of these catalysts in an alkaline medium has been tested, suggesting an excellent catalytic performance. The unique morphology and catalytic activity are believed to be invaluable for future fabrication of metal or metal oxide yolk-shell structured nanoparticles and also represents a possible candidate to replace precious metal nanocatalysts for fuel cell applications.

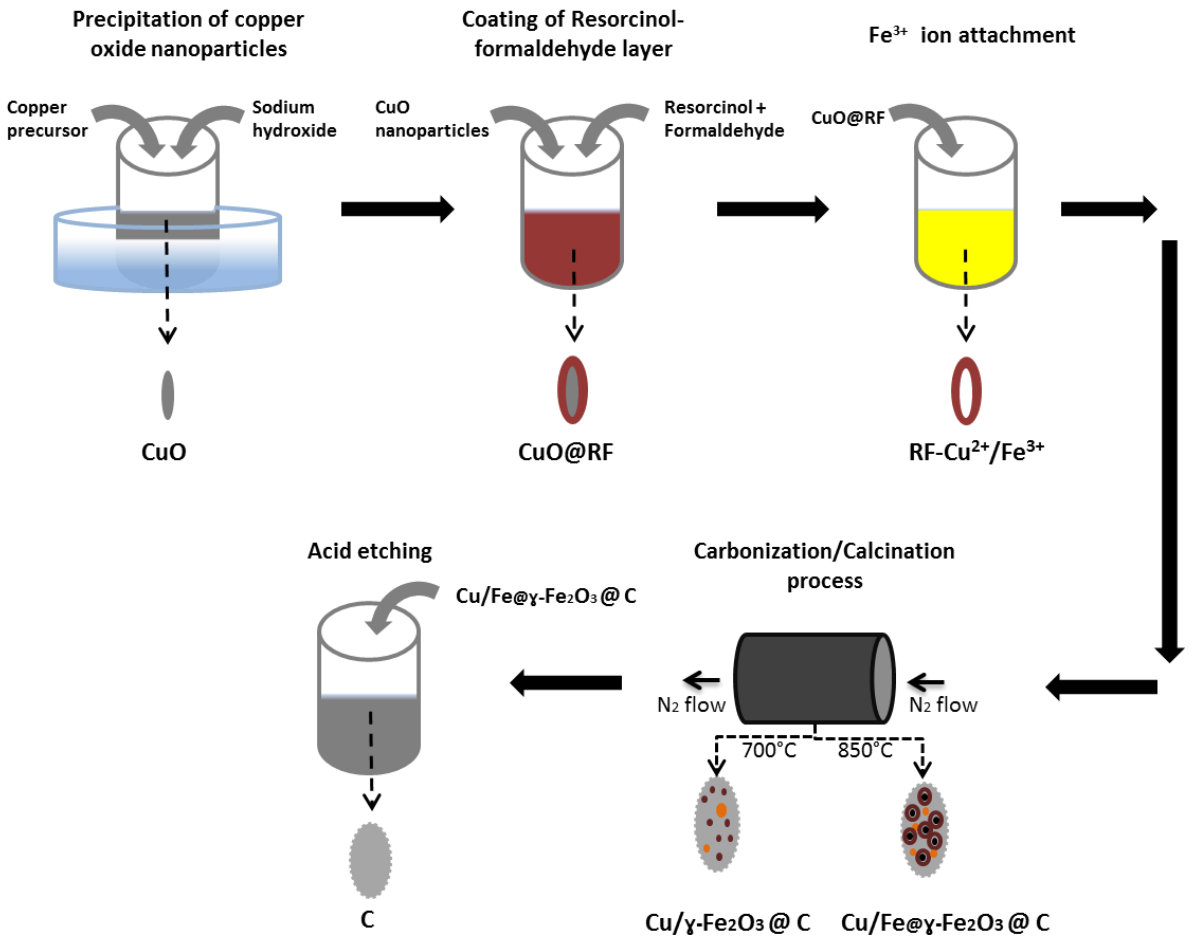

Scheme 4.1: Schematic illustration of synthesis steps of Cu/Fe@ɣ-Fe2O3 @ C core-shell nanoparticles and porous graphitic carbon nanoparticles.

4.2 Experimental Section

4.2.1 Chemicals and reagents

Resorcinol (99%), ammonium hydroxide solution (25%), formaldehyde aqueous solution (37%), copper (II) nitrate trihydrate (98%-103%), polyvinylpyrolidone PVP-40 (MW=40000), formaldehyde (36.5%-38%), iron (III) nitrate nonahydrate (98%), potassium hydroxide (KOH), absolute ethanol, hydrochloric acid (HCl) were purchased from Sigma-Aldrich company and used as supplied. Cetyltrimethylammonium bromide (CTAB) solution (0.1 M in D.I water) was made by using Cetyltrimethylammonium bromide CTAB (≥ 99%) purchased from Sigma-Aldrich as well. Sodium hydroxide NaOH solution (1 M in D.I water) was made by using pure sodium hydroxide anhydrous purchased from Chem-supply PTY LTD.

Ammonia solution (25%) was purchased from VWR Internatiaonl PTY LTD. Water was purified by a Milli Q system and had an electrical resistance of 18 MΩ•cm.

4.2.2 Synthesis of copper and gamma iron (III) oxide @ graphitic carbon (Cu/ɣ-Fe_2O_3 @ C) AND copper and iron@gamma iron (III) oxide @ graphitic carbon (Cu/Fe@ɣ-Fe_2O_3 @ C) core-shell particles

0.2 g of as-prepared CuO@RF core-shell nanoparticles were dispersed into 50 mL of 0.2 M iron (III) nitrate nonahydrate aqueous solution under sonication. Then suspension was placed on magnetic stirring heating plate and stirred for 20 h at room temperature. Subsequently, the Fe^{3+} coordinated CuO@RF nanoparticles were centrifuged and washed with water before dried in an electrical oven overnight. In order to create Cu/ɣ-Fe_2O_3 @ graphitic C and Cu/Fe@ɣ-Fe_2O_3 @ graphitic C core-shell nanoparticles, about 0.1 g such dried Fe^{3+} coordinated nanoparticles were calcined under nitrogen flow in a tube furnace with a heating rate of 1 °C min^{-1} up to 350 °C, dwelling for 2 h, and resuming heating rate at 1 °C min^{-1} up to 700 or 850 °C, respectively, and then dwelling for 4 h.

4.2.3 Synthesis of metal free graphitic carbon particles

50 mg of as-synthesized Cu/ɣ-Fe_2O_3 @ C or Cu/Fe@ɣ-Fe_2O_3 @ C nanoparticles were dispersed into 50 mL of 4 M HCl solution under sonication then transferred the suspension to 60 °C heating plate and left particles simmered overnight without stirring. Finally, final products were centrifuged and washed with water before drying at 75 °C for in an electrical oven. The metal free graphitic carbon samples are named as C-a, where “a” indicates the carbonization temperature.

4.2.4 Characterisation

Transmission electron microscopy (TEM) images were acquired with a JEOL 2100 microscope operated at 120 KV. High Angle Annular Dark Field Scanning Transmission Electron Microscopy (HAADF-STEM) images and element mapping were obtained using a FEI Titan G2 80-200 TEM/STEM with ChemiSTEM Technology operated at 200 KV. Scanning electron microscopy (SEM) images were taken with a Zeiss 1555 VP-FESEM at an operating voltage of 3 KV. Samples for the above measurements were prepared by suspending fine powder products in 100% ethanol under sonication and placing a drop of the suspension onto a carbon coated

gold grid for TEM and an aluminium stub for SEM, and allowing the ethanol to evaporate naturally before analysis. The measurements of nitrogen adsorption and desorption isotherms were performed using a Micromeritics TriStar II surface area and porosity analyser. Samples were degassed at 150 °C for at least 10 h before the measurements were carried out. The specific surface areas were calculated by the Brunauer-Emmett-Teller (BET) method from the adsorption isotherms. XRD measurements were obtained using a Bruker-AXS D8 Advance Diffractometer with Cu Kα radiation (40 KV, 40 mA) and a LynxEye position sensitive detector. Information on crystalline phases was confirmed against the database of JCPDS files.

4.2.5 Electrochemical measurements

The performance evaluations of oxygen reduction reaction (ORR) on all prepared catalysts were carried out in a standard three-electrode electrochemical cell with O2-saturated KOH electrolyte (0.1 M) using a catalyst-coated glassy carbon rotating disk electrode (GC-RDE, 0.196 cm2, Pine Research Instrumentation), a platinum wire and Ag/AgCl (4 M KCl filled) as a working electrode, a counter electrode and a reference electrode, respectively. The catalyst-coated working electrode was prepared by a controlled drop-casting approach as described elsewhere (36). First, a homogeneous catalyst ink was prepared by ultrasonically dispersing 10 mg of catalyst in a solution containing 1 mL of absolute ethanol and 0.1 mL of 5 wt% Nafion solutions, and then 5 μL of the catalyst ink was pipetted onto the surface of the GC-RDE, leading to a catalyst loading of ~0.232 mg cm^{-2}_{disk}. Finally, it was dried in air at room temperature to form the catalyst-modified working electrode. All the electrochemical data were recorded on a CHI 760E bipotentiostat. Cyclic voltammograms (CVs) were conducted at a scan rate of 100 mV s^{-1}, and linear sweep voltammograms (LSVs) were obtained at a scan rate of 5 mV s^{-1} using the RDE at 1600 rpm. All the measured potential values vs. Ag/AgCl were calibrated to the reversible hydrogen electrode (RHE) according to the following equation: $E_{RHE} = E_{Ag/AgCl} + 0.948$, which was determined by a calibrated measurement in a H_2-saturated electrolyte with platinum RDE as the working electrode.

4.3 Results and Discussion

4.3.1 Synthesis and characterisations of Cu/ɣ-Fe_2O_3@C and Cu/Fe@ɣ-Fe_2O_3@C core-shell nanoparticles and graphitic C nanoparticles

As illustrated in Scheme 4.1, CuO@RF particles as synthesized in Chapter 3 were used as the base particles for Fe ion attachment. TEM images of RF-Cu^{2+}/Fe^{3+} particles in Figure 4.1 show a hollow structured morphology where brush like CuO templates were removed during the Fe^{3+} attachment process leaving empty chambers inside RF. It is obvious that 0.2 M of iron (III) nitrate nonahydrate was strong enough to dissolve all of the stable CuO templates. EDS mapping on the selected area of the RF-Cu^{2+}/Fe^{3+} sample (Figure 4.1(c)) shows the signals of iron and copper. As no metal solid was observed anywhere in the sample, it could be determined that ionic copper and iron existed within the RF layer. In addition, this discovery of a CuO dissolution phenomenon is crucial to understanding the formation of ɣ-Fe2O3 and Fe@ɣ-Fe2O3 nanoparticles in the following discussion.

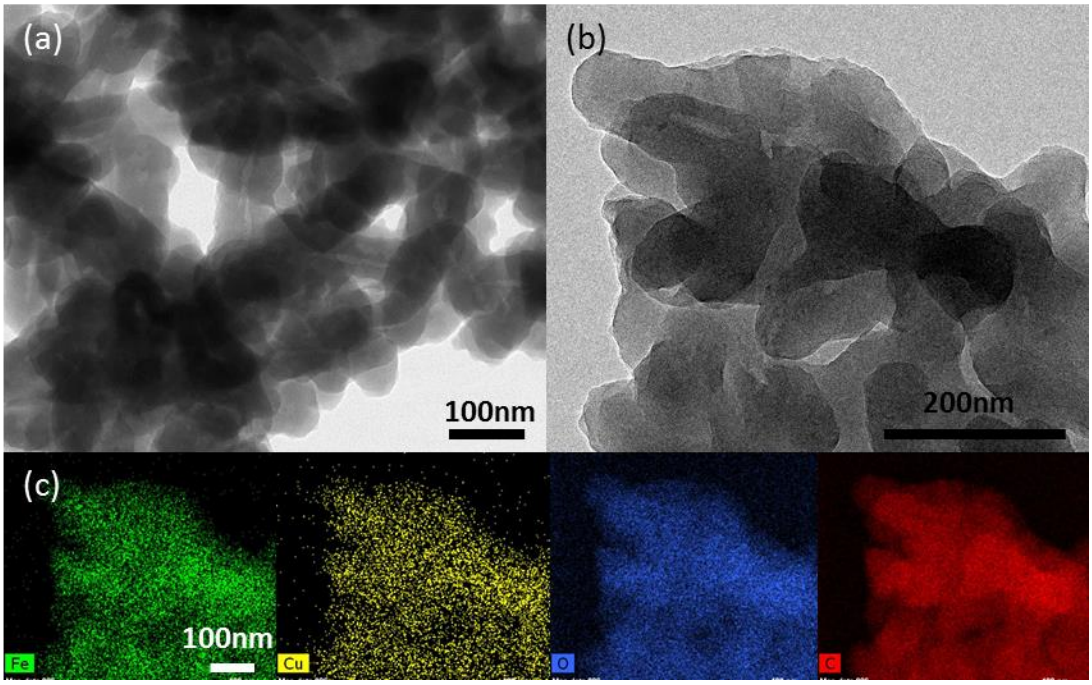

Figure 4.1: (a) and (b) TEM images of RF-Cu^{2+}/Fe^{3+} particles; (c) EDS mapping of RF-Cu^{2+}/Fe^{3+} particles.

RF-Cu^{2+}/Fe^{3+} hollow structured particles turned into Cu/ɣ-Fe_2O_3@C multi-core shell particles through a carbonization process under nitrogen gas. The morphology and composition of the Cu/ɣ-Fe_2O_3@C sample were investigated by SEM, TEM and EDS, as shown in Figure 4.2. It can be observed from SEM image (Figure 4.2(a)) that the rod shaped particles possess a relatively smooth and undamaged carbon shell. Although some very tiny patches (highlighted by arrows) exist on the shell surface, they could be the formation of ɣ-Fe_2O_3 nanoparticles or Cu nanoparticles at the outer surface of the graphitic carbon layer. Figure 4.2(b) shows a typical TEM image of a Cu/ɣ-Fe_2O_3@C multi-core/shell particle having ɣ-Fe_2O_3 core sizes in the diameter range from 10 to 15 nm and a Cu core around 50 nm. As mentioned, copper ions co-existed with iron ions in the RF shell after the Fe^{3+} attachment process. Iron ions combined with oxygen to form ɣ-Fe_2O_3 nanoparticles, and copper ions gathered into metallic Cu nanoparticles during annealing. Most of the cores formed within the carbon shell, with a few at the outer shell surface. Due to the carbonization from RF to carbon, and graphitization from amorphous carbon to graphitic carbon, the shell material became thinner and very small void spaces formed at the interface between the metal oxide and carbon shell. EDS mapping (Figure 4.2(c)) gives the element distribution and composition of this sample. It is clear that iron and oxygen exist in the small nano-core areas, and a strong copper signal appears at the large and dark nanoparticle. A weak copper signal is observed outside the primary copper particle, which is suspected to be from small amounts of copper being doped outside the ɣ-Fe2O3 cores. The corresponding XRD pattern will confirm the presence of Cu and ɣ-Fe2O3 as shown in the following section.

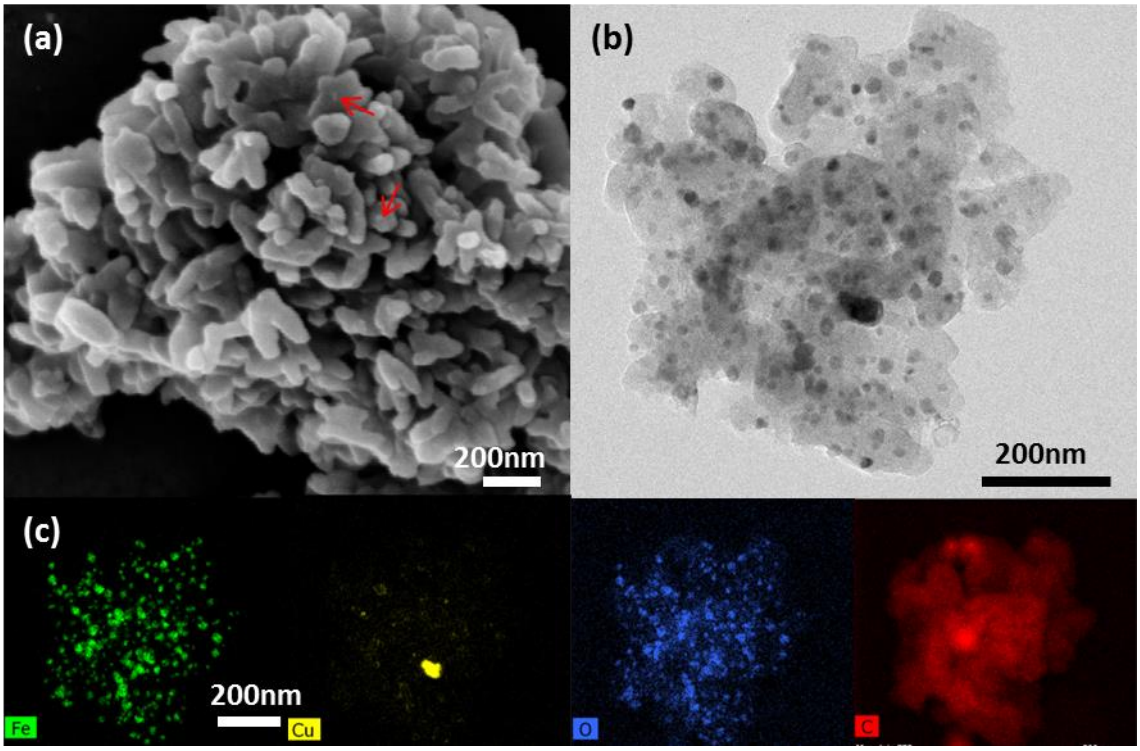

Figure 4.2: (a) SEM image of Cu/ɣ-Fe_2O_3@C core-shell particles; (b) TEM image of Cu/ɣ-Fe_2O_3@C core-shell particles; (c) EDS mapping of Cu/ɣ-Fe_2O_3@C core-shell particles.

Figure 4.3 presents the morphology and EDS mapping of Cu/Fe@ɣ-Fe_2O_3@C calcined under nitrogen at 850 °C. In contrast to the Cu/ɣ-Fe_2O_3@C sample (Figure 4.2), Cu/Fe@ɣ-Fe_2O_3@C has more broken carbon shell as seen in Figure 4.3(a), and core-shell, yolk-shell and hollow structured cores formed as shown in Figure 4.3(b). The thinner and more broken carbon layer is due to the higher graphitic degree of the carbon material and also the consumption of the carbon material for the reduction reaction between the metal oxide and carbon shell. When the calcination temperature was increased to 850 °C, core nanoparticles grew to around 50 nm in size. Most of the nanocores are in a yolk-shell structure, and the three-dimensional structure was further confirmed by the tilted (-30°, 0° and 30°) STEM images of Cu/Fe@ɣ-Fe_2O_3@C as seen in Figure 4.4. The EDS mapping (Figure 4.3(c)) provides the element distribution, indicating that iron is present in the entire core regardless of the structure, oxygen seems only to appear in the shell of the cores, and copper scatters over all cores without showing any intense signal. Furthermore, the structure of the yolk-shell cores can be further confirmed using HRTEM imaging (Figure 4.3(d)).

The HRTEM image at selected area 1 indicates a typical ɣ-Fe_2O_3 lattice spacing of 0.25 nm which corresponds to the (311) lattice planes. In addition, the lattice spacing at selected area 2 is 0.2 nm which corresponds to the (110) lattice plane of metallic Fe.

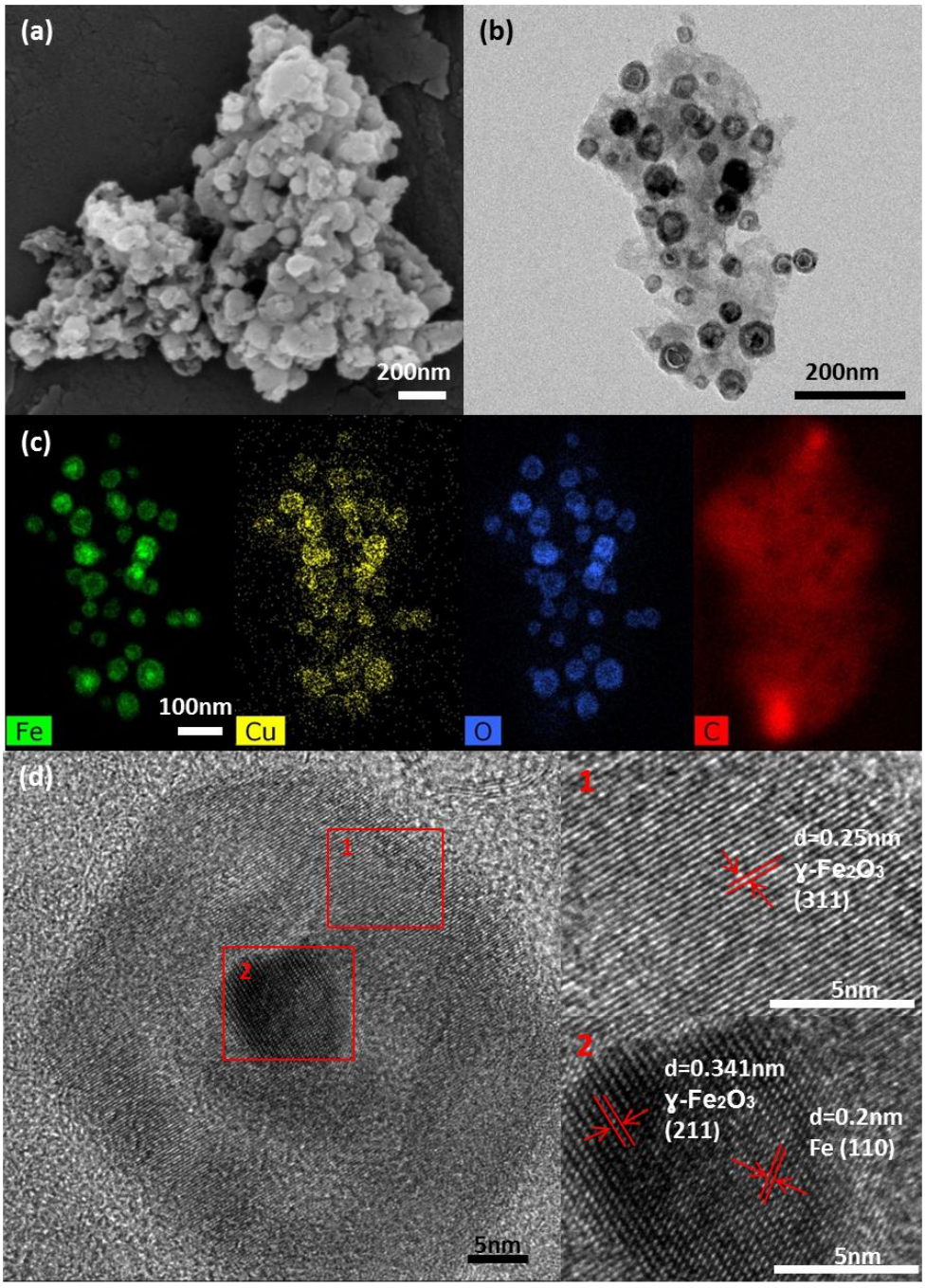

Figure 4.3: (a) SEM image of Cu/Fe@ɣ-Fe_2O_3@C core-shell particles; (b) TEM image of Cu/Fe@ɣ-Fe_2O_3@C core-shell particles; (c) EDS mapping of Cu/Fe@ɣ-Fe_2O_3@C core-shell particles; (d) HRTEM image of Fe@ɣ-Fe_2O_3 yolk-shell structured nanocore.

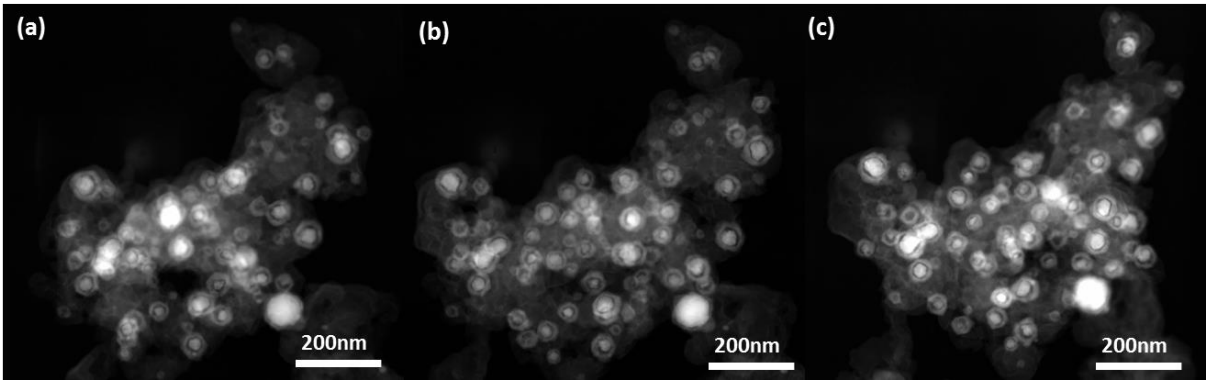

Figure 4.4: Tilted STEM images of Cu/Fe@ɣ-Fe_2O_3@C particle at (a) -30°; (b) 0° and (c) 30°.

Cu/ɣ-Fe_2O_3@C and Cu/Fe@ɣ-Fe_2O_3@C samples were washed with 4M hydrochloric acid to remove metal and metal oxide nanoparticles in order to obtain metal free graphitic carbons, C-700 and C-850, respectively. As shown in Figure 4.5**(**a), the surface morphology of the carbon layer in the C-700 sample remained unchanged after acid washing, suggesting that the tiny cores can be etched out through the porous shell without breaking the carbon layer. In contrast, the SEM image of C-850 (Figure 4.5(d)) shows highly broken carbon particles, which may be attributed to the fact that the carbon shell had become so fragile that the etching and centrifugation steps broke the thin layers further. The HRTEM images in Figure 4.5(c) and 4.5(f) clearly demonstrate that C-850 possesses a much higher graphitic degree than C-700, as shown by the nicely ordered graphite layers. However, not all metal cores could be removed via this acid washing. The TEM images in Figure 4.6 show that a very small percentage of both carbon samples have some tiny metal oxide cores remaining encapsulated in the well-formed graphitic carbon layers where the acid was unable to reach.

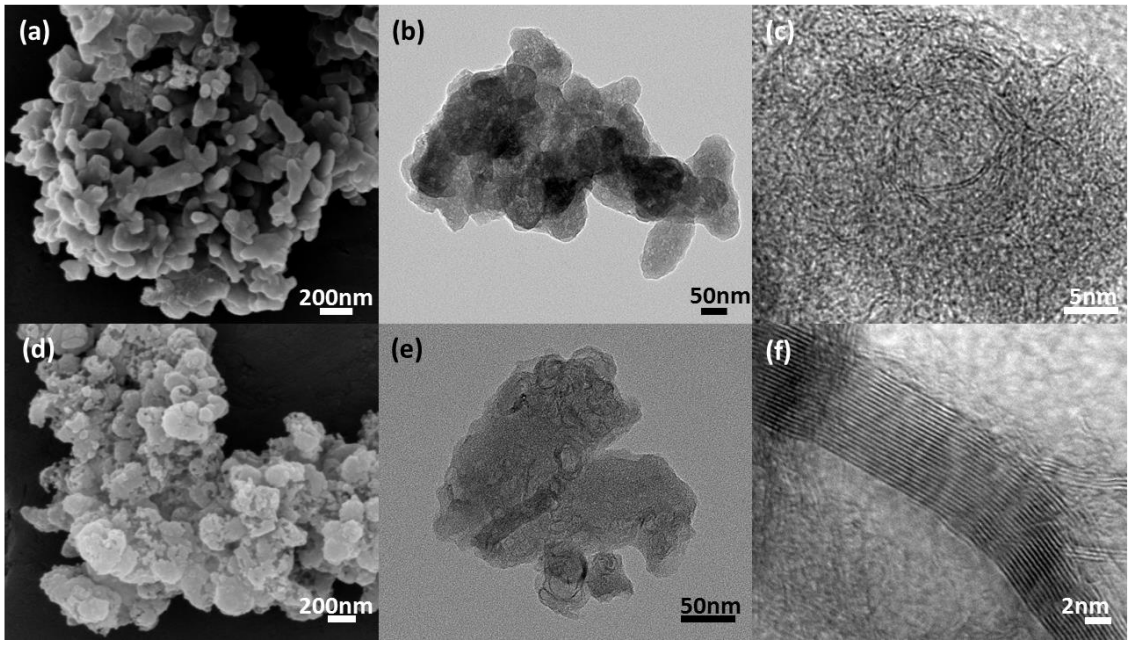

Figure 4.5: (a) SEM image of C-700; (b) TEM image of C-700; (c) HRTEM image of C-700; (d) SEM image of C-850; (e) TEM image of C-850; (f) HRTEM image of C-850.

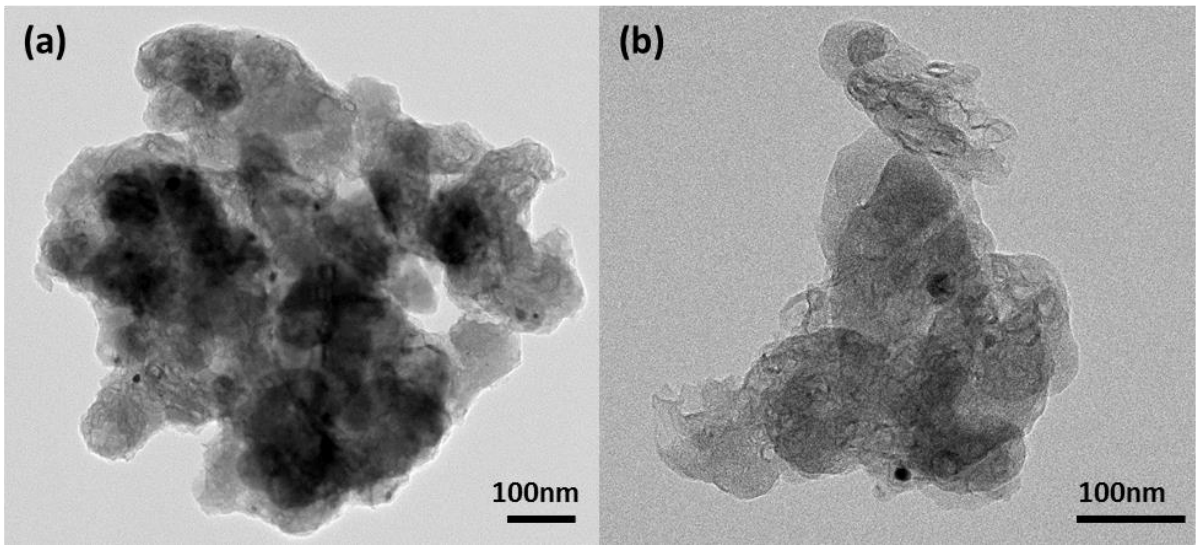

Figure 4.6: (a) TEM image of C-700; (b) TEM image of C-850.

The surface areas of all samples were determined by the BET method from nitrogen adsorption and desorption isotherms. From Figure 4.7 it can be clearly seen that these isotherms are typical type IV isotherms with hysteresis loops (relative pressure ranges from 0.45 to 0.95) revealing the mesoporous property. Cu/ɣ-Fe_2O_3@C possesses the highest BET surface area of 485 m^2/g, while Cu/Fe@ɣ-Fe_2O_3@C has a

surface area of 422 m^2/g. Furthermore, there are also very narrow hysteresis loops at lower relative pressure ranges, 0 to 0.35, for both carbon samples, C-700 (Figure 4.7(c)) and C-800 (Figure 4.7(d)). These loops indicate that very small amounts of micropores are present in the samples. These micropores were most probably caused by the removal of metal nanoparticles formed at the shell surface.

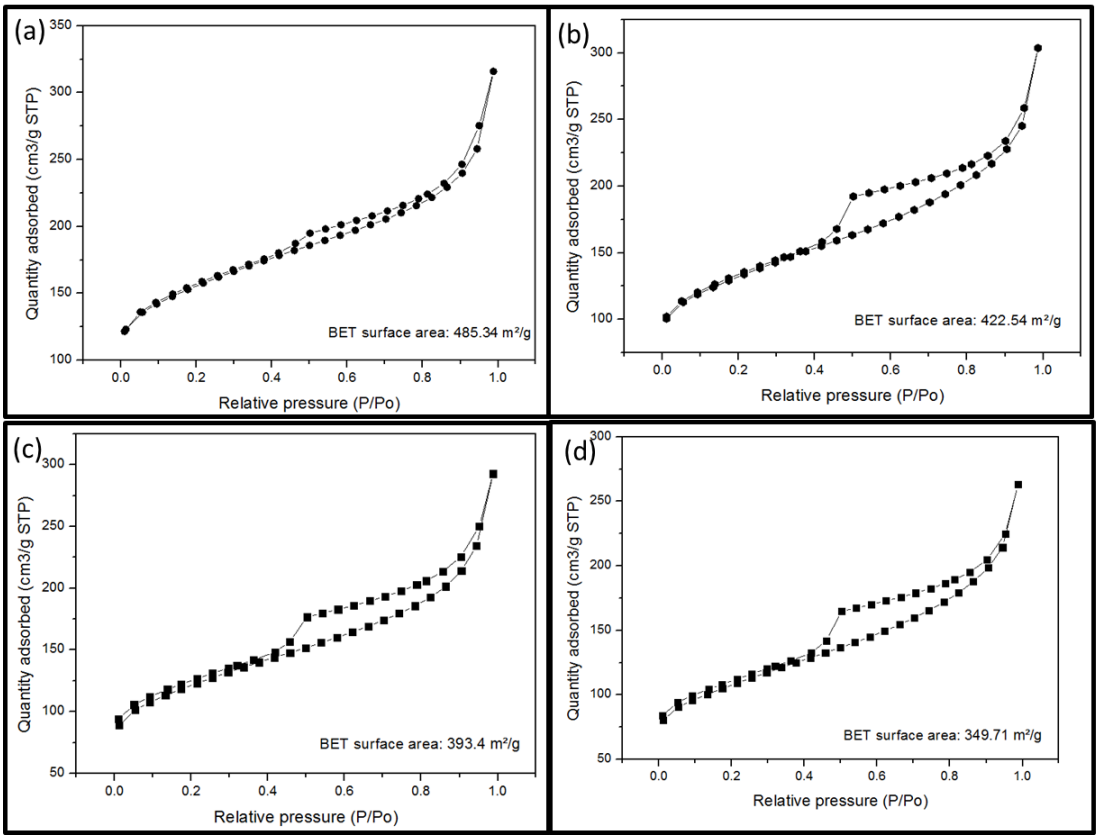

Figure 4.7: N_2 adsorption isotherms for (a): Cu/ɣ-Fe_2O_3@C core-shell particles; (b): Cu/Fe@ɣ-Fe_2O_3@C core-shell particles; (c): C-700 particles; (d): C-850 particles.

4.3.2 Composition analysis and proposed formation mechanisms of Cu/ɣ-Fe_2O_3@C and Cu/Fe@ɣ-Fe_2O_3@C core-shell particles

Interestingly, the composition and structure of the metal compounds changed throughout the various synthesis steps, which make it fascinating to analyse further to elucidate the formation mechanisms of metal and metal oxides. XRD patterns shown in Figure 4.8 confirm the presence of Cu, ɣ-Fe_2O_3, Fe and graphitic C where the XRD peaks match perfectly with the data obtained from JCPDS files (no. 04-0836, no. 39-1346, no. 06-0696, no. 26-1079), respectively. Together with EDS

mapping from Figures 4.2 and 4.3 and EDS spectra from Figure 4.9 and Figure 4.10, we can obtain a clear picture of the composition changes and formation mechanism of metal and metal oxide nanoparticles at different calcination temperatures. Firstly, at 700 °C, the iron ions existing in the RF shell after the Fe^{3+} attachment step, the elemental oxygen from the dissolved CuO templates and RF shell combined into very small sized ɣ-Fe_2O_3 nanoparticles. However, copper ions did not combine with iron and oxygen, forming into metallic Cu instead of an alloy or alloy oxide or copper oxide. The EDS mapping in Figure 4.2(c) indicates that no iron or oxygen signals were detected where a very strong copper signal appeared. In addition, the selected area 1 spectrum (Figure 4.9(b)) at the intense copper signal area on the EDS mapping (Figure 4.9(a)) gave three high peaks for copper with negligible oxygen and iron peaks, and those weak oxygen and iron peaks are likely background signals from the ɣ-Fe_2O_3 nanoparticles existing near the metallic Cu nanoparticle. Moreover, both EDS mapping (Figure 4.2(c)) and the EDS spectrum of selected area 2 (Figure 4.9(c)) confirm that only trace levels of copper are detected outside the main copper particles. Furthermore, the metallic Fe peak from the XRD pattern for the Cu/ɣ-Fe_2O_3@C sample is believed to be attributed to the small amount of Fe@ɣ-Fe_2O_3 nanoparticles, which was mentioned in the previous part. Subsequently, with the increment of calcination temperature up to 850 °C, all tiny solid ɣ-Fe_2O_3 nanoparticles coalesced and formed larger nanoparticles possessing hollow or yolk-shell structures. According to the EDS mapping (Figure 4.3(c)), XRD pattern (Figure 4.8(b)) and EDS spectra (Figure 4.10(b), (c)) of Cu/Fe@ɣ-Fe_2O_3@C, it can be easily identified that the hollow structured nanoparticles are ɣ-Fe_2O_3 and the yolk-shell structured nanoparticles consist of a Fe yolk and ɣ-Fe_2O_3 shell. Moreover, the copper content in Cu/Fe@ɣ-Fe_2O_3@C is similar to Cu/ɣ-Fe_2O_3@C, and the copper did not participate in forming a metal oxide but doped onto the iron oxide surface and also formed into metallic copper. In samples containing Cu particles, the high signal from the particles dominates the maps, making it difficult to see the weaker signal from the surrounding material, and it is only by extracting spectra from these regions that the weak Cu peaks become visible. In contrast, when the Cu particles are not present, the Cu maps reveal the weaker background signal more easily despite the peaks in the spectrum remaining very small. In addition, a small number of large metallic Fe

nanoparticles formed in the Cu/Fe@ɣ-Fe_2O_3@C sample, which was believed to be the final product if the calcination temperature rose further.

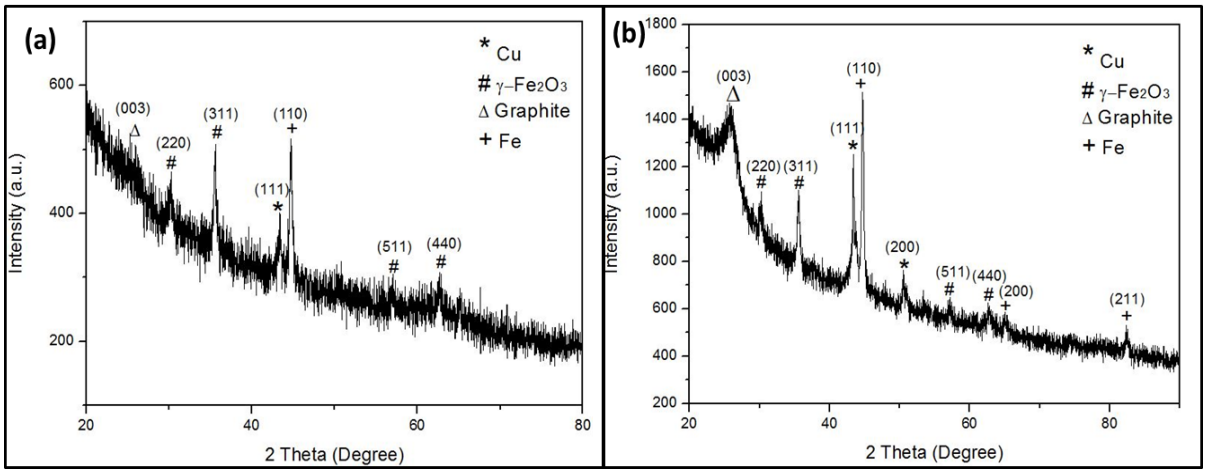

Figure 4.8: XRD patterns of (a): Cu/ɣ-Fe_2O_3@C particles; (b): Cu/Fe@ɣ-Fe_2O_3@C core-shell particles

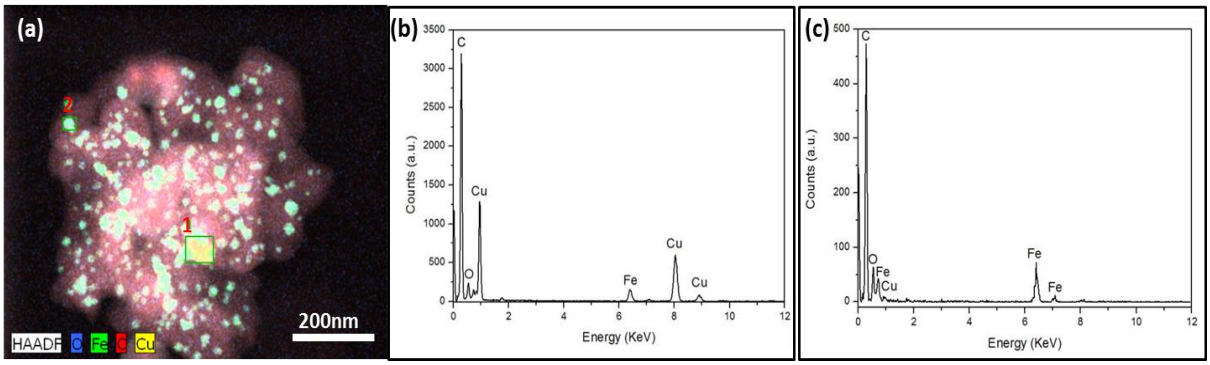

Figure 4.9: (a) EDS element distribution map of Cu/ɣ-Fe2O3@C; (b) EDS spectrum of selected area 1 of Cu/ɣ-Fe2O3@C; (c) EDS spectrum of selected area 2 of Cu/ɣ-Fe2O3@C.

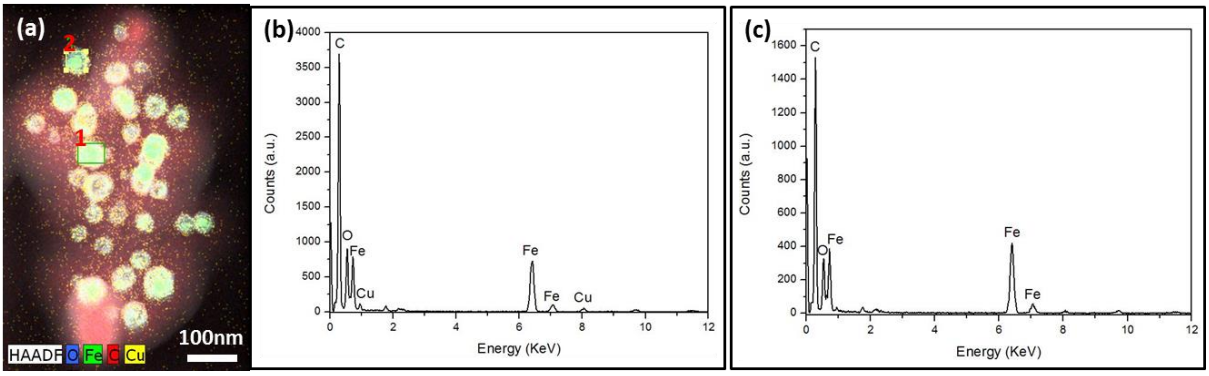

Figure 4.10: (a) EDS mapping element distribution map of Cu/Fe@ɣ-Fe2O3@C; (b) EDS spectrum of selected area 1 of Cu/Fe@ɣ-Fe2O3@C; (c) EDS spectrum of selected area 2 of Cu/Fe@ɣ-Fe2O3@C.

Furthermore, the role of CuO as a template has been investigated. Experiments were done by using RF nanospheres only, without involving CuO, and with the same synthesis procedures and experimental parameters. Results (Figure 4.11) proved that involving copper oxide was essential in forming Fe@ɣ-Fe_2O_3 yolk-shell structure nanocores. When copper was absent in the whole synthesis, only solid nanocores appeared after the carbonization process.

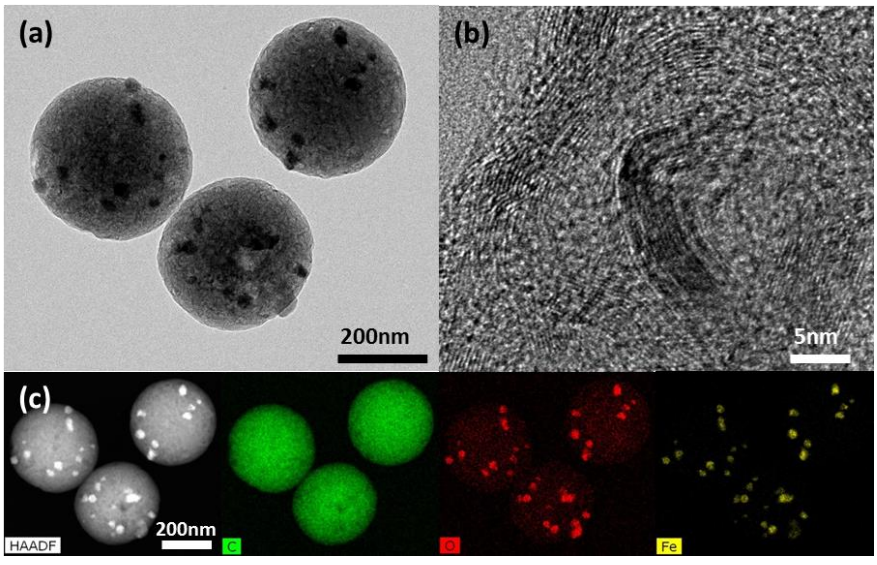

Figure 4.11: (a) TEM image Fe_2O_3@C core-shell particles calcined at 850°C; (b) HRTEM image of graphitic carbon layer; (c) HAADF and EDS mapping of Fe_2O_3@C core-shell particles.

The formation mechanisms of the metal and metal oxide nanoparticles are proposed at this stage according to all data given from the various measurements. Scheme 4.2 presents visual information of the changing process. It is believed that tiny ɣ-Fe2O3 nanoparticles formed and aggregated when the temperature increased, and transferred from solid to a hollow structure with increasing calcination time at a certain calcination temperature via the Ostwald ripening process. When the calcination temperature rose further, the aggregation and hollowing continued but in the meantime carbon shell acted as a reducing agent and started to reduce ɣ-Fe2O3 to metallic Fe, which appeared as the yolk in the hollow ɣ-Fe2O3 nanoparticle under inert gas environment. This yolk-shell structure formation mechanism is proposed to be the inward diffusion of the Kirkendall effect (37). The C layer has consumed the oxygen element from the hollow Fe_2O_3 sphere at the contacting sides and the oxygen transferred from inside outwardly forming reduced Fe core in the middle and the void - at the same time. Increasing the temperature further continued the aggregation and reduction processes to form the huge metallic Fe nanoparticles with a very thin carbon layer support (as seen in Scheme 4.2.

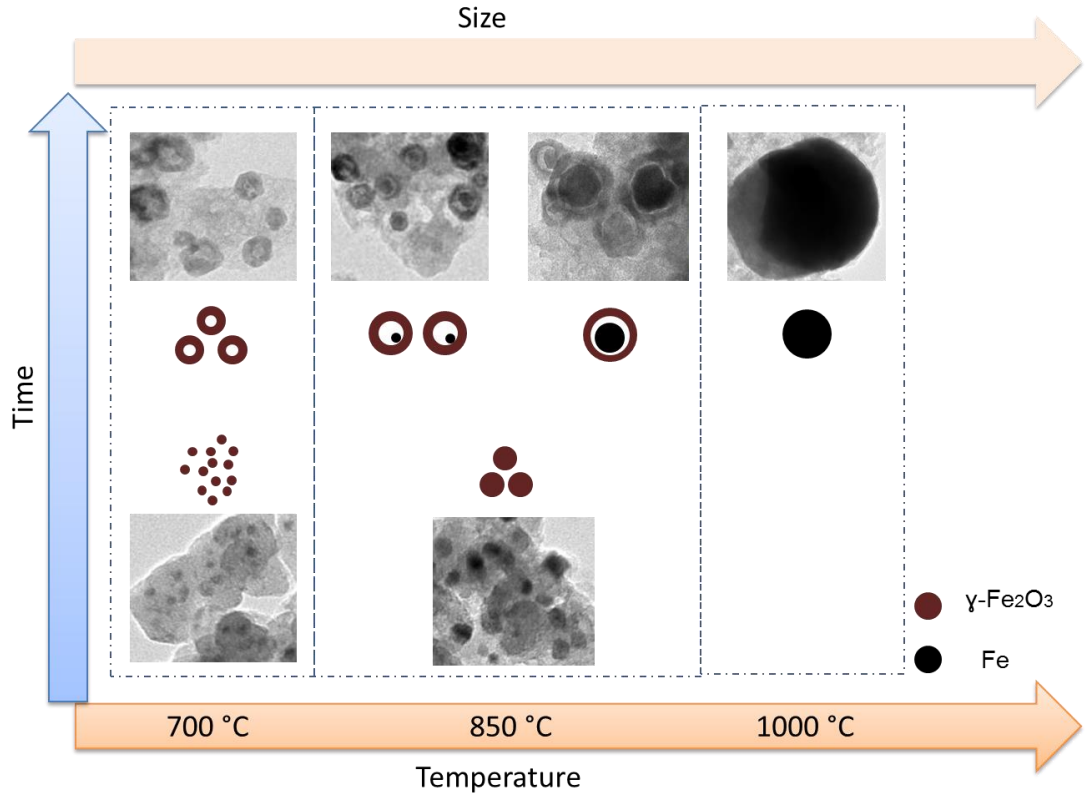

Scheme 4.2: Schematic illustration of formation process of solid, hollow and yolk-shell structured Fe and ɣ-Fe2O3 nanoparticles.

4.3.3 Electrocatalytic performance of the catalysts for the ORR

The ORR performance of the as-prepared Cu/ɣ-Fe_2O_3@C, Cu/Fe@ɣ-Fe_2O_3@C, C-700 and C-850 in alkaline solution was initially evaluated by conducting cyclic voltammetry (CV) measurements. As shown in Figure 4.12, it is obvious that all samples have an electrocatalytic activity towards ORR as there is a notable cathodic peak in each CV curve. As compared to C-700 and C-850 samples, the oxygen-reduction peaks of Cu/ɣ-Fe_2O_3@C and Cu/Fe@ɣ-Fe_2O_3@C present more positive potentials of 0.67 and 0.66 V (vs. reversible hydrogen electrode (RHE)), respectively. It indicates that the as-developed core-shell structured nanocatalysts possess a better catalytic ability for ORR. To further verify the excellent ORR catalytic ability of core-shell nanocatalysts, linear sweep voltammetry (LSV) measurements were carried out in a standard three-electrode system at a scan rate of 5 mV s^{-1} using a rotating disk electrode (RDE) technique. Figure 4.13 displays a comparison of LSV curves of all the electrocatalysts performed at 1600 rpm and LSV measurements of Cu/ɣ-Fe_2O_3@C at various rotation rates. The onset potentials of Cu/ɣ-Fe_2O_3@C, Cu/Fe@ɣ-Fe_2O_3@C, C-850 and C-700 are around 0.86, 0.85, 0.82 and 0.80 V, respectively. Besides the most positive onset potential, Cu/ɣ-Fe_2O_3@C also delivered the highest half-wave potential of 0.69 V as well as the highest limiting current density of 5.1 mA cm^{-2}. Moreover, a wide current plateau was observed, implying a diffusion-dominated process corresponding to an efficient four-electron ORR pathway, which has been further demonstrated by a Koutecky-Levich (K-L) plot (Figure 4.13 (b)). The calculated electron-transfer number (n) in the ORR is 3.97 for the Cu/ɣ-Fe_2O_3@C catalyst. Therefore, according to both CV and LSV measurements, it can be clearly seen that Cu/ɣ-Fe_2O_3@C has the best electrocatalytic performance for the ORR, and the activity of the other catalysts decreases in the order of Cu/Fe@ɣ-Fe_2O_3@C > C-850 > C-700. It is believed that the better catalytic performance of Cu/ɣ-Fe_2O_3@C could be reasonably attributed to the smaller particle size of metal and metal oxide cores, the synergetic effects from the core-shell architecture, and the better interactions between conductive carbon shells and Fe_2O_3 cores (38). The much smaller nanocores within the carbon shell provide larger catalytic contacting area which leads to more numerous active sites for ORR. Compared with the metal-containing samples, the metal-free counter parts showed very low ORR catalytic activities, because most of the active Cu or Fe (oxide)

species on them have been removed after the acid etching treatments. In addition, the higher graphitic level of the carbon materials also possesses slightly better activity towards fuel cell reactions than less graphitic ones (39). Furthermore, as shown in Table 4.1, in comparison with other similar composition particles, Cu/ɣ-Fe_2O_3@C has better performance for ORR than ɣ-Fe_2O_3/C, Fe-N-C nanoparticles (40) and ɣ-Fe_2O_3/N-CNTs nanoparticles (25).

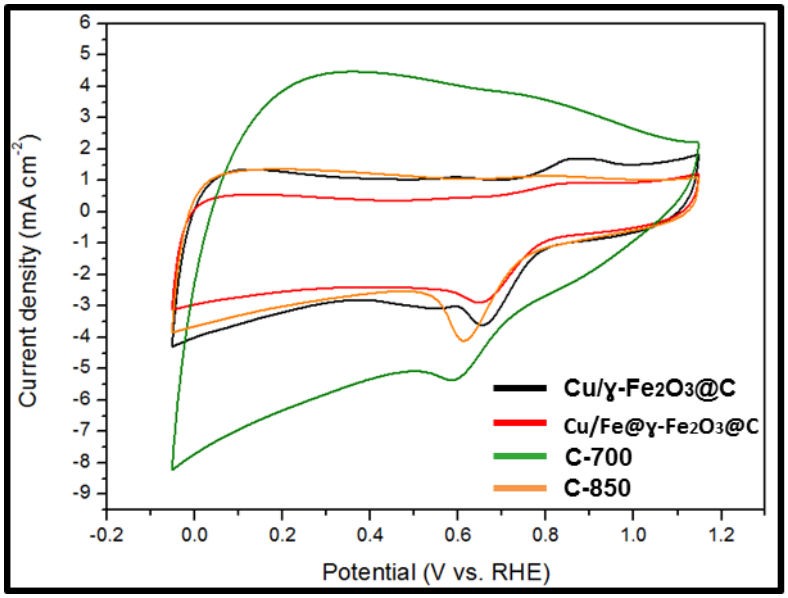

Figure 4.12: CV curves of Cu/ɣ-Fe2O3@C, Cu/Fe@ɣ-Fe2O3@C, C-700 and C-850 in O2-saturated 0.1 M KOH solution at a scan rate of 100 mV s-1.

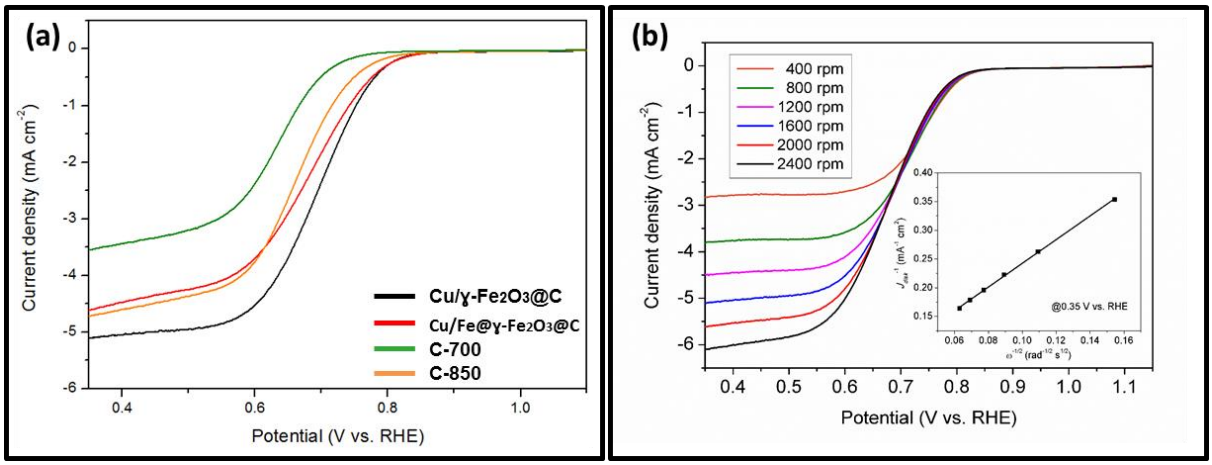

Figure 4.13: (a) LSV curves of Cu/ɣ-Fe_2O_3@C, Cu/Fe@ɣ-Fe_2O_3@C, C-700 and C-850 on the RDE at 1600 rpm in O_2-saturated 0.1 M KOH solution at a scan rate of 5 mV s^{-1}. (b) LSV curves of Cu/ɣ-Fe_2O_3@C in O_2-saturated 0.1 M KOH electrolyte at different rotation rates from 400 to 2400 rpm. Inset: K–L plot at 0.35 V for Cu/ɣ-Fe_2O_3@C on the basis of the RDE data in (b).

Table 4.1: Catalytic activity of Cu/ɣ-Fe_2O_3@C compared to the results from other literatures.

Catalyst	Performance		Ref.
Particle name	Onset potentials (V)	Cathodic ORR peak (V)	
Cu/ɣ-Fe_2O_3@C	0.86 (RHE)	0.67 (RHE)	This study
Fe-N-C	0.8 (RHE)	≈ 0.62 (RHE)	(40)
ɣ-Fe_2O_3/C	No activity	No activity	(40)
ɣ-Fe2O3/N-CNTs	-0.28 (vs. Ag/AgCl)	-0.33 (vs. Ag/AgCl)	(25)

4. Conclusions

Cu/ɣ-Fe_2O_3@C, Cu/Fe@ɣ-Fe_2O_3@C core-shell particles and highly graphitic carbon particles have been successfully prepared by a facile process. The CuO templates played an essential role in forming metallic Cu and also Cu-doped Fe@ɣ-Fe_2O_3 yolk-shell nanoparticles. It is believed that such a mechanism may be beneficial for further study in synthesising yolk-shell structured metal or metal oxide nanoparticles without employing the traditional templating methods. Finally, the ORR activity evaluation was performed for all as-prepared samples. Due to the synergistic effect of Cu and ɣ-Fe_2O_3, Cu/ɣ-Fe_2O_3@C particles possess the best electrocatalytic activity in an alkaline medium, which is comparable or even superior to other reported nanocatalysts having similar composition. Taking into account the unique morphology and simple synthesis method and reasonably good electrocatalytic performance, with some modifications to the carbon shell (such as nitrogen or sulphur doping), the core-shell Cu/ɣ-Fe_2O_3@C particles could be a promising candidate for electrocatalytic applications.

Reference

1. Yang J, Sun H, Liang H, Ji H, Song L, Gao C, et al. A Highly Efficient Metal-Free Oxygen Reduction Electrocatalyst Assembled from Carbon Nanotubes and Graphene. Adv Mater. 2016;28(23):4606-13.

2. Li Q, Wan G, Zhao H, Pan L, Wang N, Zhao W, et al. Nitrogen-Doped Carbon Vesicles with Dual Iron-Based Sites for Efficient Oxygen Reduction. ChemSusChem. 2017;10(3):499-505.

3. Wang D-W, Su D. Heterogeneous nanocarbon materials for oxygen reduction reaction. Energy Environ Sci. 2014;7(2):576-91.

4. Gu L, Jiang L, Jin J, Liu J, Sun G. Yolk–shell structured iron carbide/N-doped carbon composite as highly efficient and stable oxygen reduction reaction electrocatalyst. Carbon. 2015;82:572-8.

5. Xiao J, Chen C, Xi J, Xu Y, Xiao F, Wang S, et al. Core-shell Co@Co3O4 nanoparticle-embedded bamboo-like nitrogen-doped carbon nanotubes (BNCNTs) as a highly active electrocatalyst for the oxygen reduction reaction. Nanoscale. 2015;7(16):7056-64.

6. Su C, Yang T, Zhou W, Wang W, Xu X, Shao Z. Pt/C-LiCoO2 composites with ultralow Pt loadings as synergistic bifunctional electrocatalysts for oxygen reduction and evolution reactions. J Mater Chem A. 2016;4(12):4516-24.

7. Jee S-W, Choi W, Ahn CH, Yang G, Cho HK, Lee J-H, et al. Enhanced oxygen reduction and evolution by in situ decoration of hematite nanoparticles on carbon nanotube cathodes for high-capacity nonaqueous lithium-oxygen batteries. J Mater Chem A. 2015;3(26):13767-75.

8. Zheng Y, Jiao Y, Jaroniec M, Jin Y, Qiao SZ. Nanostructured Metal-Free Electrochemical Catalysts for Highly Efficient Oxygen Reduction. Small. 2012;8(23):3550-66.

9. Dai L, Xue Y, Qu L, Choi H-J, Baek J-B. Metal-Free Catalysts for Oxygen Reduction Reaction. Chem Rev. 2015;115(11):4823-92.

10. Li Y, Zhou W, Wang H, Xie L, Liang Y, Wei F, et al. An oxygen reduction electrocatalyst based on carbon nanotube-graphene complexes. Nat Nanotechnol. 2012;7(6):394-400.

11. Wen Z, Ci S, Zhang F, Feng X, Cui S, Mao S, et al. Nitrogen-Enriched Core-Shell Structured Fe/Fe3C-C Nanorods as Advanced Electrocatalysts for Oxygen Reduction Reaction. Adv Mater. 2012;24(11):1399-404.

12. Wu Z-Y, Xu X-X, Hu B-C, Liang H-W, Lin Y, Chen L-F, et al. Iron Carbide Nanoparticles Encapsulated in Mesoporous Fe-N-Doped Carbon Nanofibers for Efficient Electrocatalysis. Angew Chem Int Ed. 2015;54(28):8179-83.

13. Wang H, Wang W, Gui M, Asif M, Wang Z, Yu Y, et al. Uniform Fe3O4/Nitrogen-Doped Mesoporous Carbon Spheres Derived from Ferric Citrate-Bonded Melamine Resin as an Efficient Synergistic Catalyst for Oxygen Reduction. ACS Appl Mater Interfaces. 2017;9(1):335-44.

14. Yan X, Jia Y, Odedairo T, Zhao X, Jin Z, Zhu Z, et al. Activated carbon becomes active for oxygen reduction and hydrogen evolution reactions. Chem Commun. 2016;52(52):8156-9.

15. Seh ZW, Kibsgaard J, Dickens CF, Chorkendorff I, Nørskov JK, Jaramillo TF. Combining theory and experiment in electrocatalysis: Insights into materials design. Science. 2017;355(6321).

16. Liu J, Wickramaratne NP, Qiao SZ, Jaroniec M. Molecular-based design and emerging applications of nanoporous carbon spheres. Nat Mater. 2015;14(8):763-74.

17. Liu B, Huo L, Si R, Liu J, Zhang J. A General Method for Constructing Two-Dimensional Layered Mesoporous Mono- and Binary-Transition-Metal Nitride/Graphene as an Ultra-Efficient Support to Enhance Its Catalytic Activity and Durability for Electrocatalytic Application. ACS Appl Mater Interfaces. 2016;8(29):18770-87.

18. Yang ZK, Lin L, Xu A-W. 2D Nanoporous Fe−N/C Nanosheets as Highly Efficient Non-Platinum Electrocatalysts for Oxygen Reduction Reaction in Zn-Air Battery. Small. 2016;12(41):5710-9.

19. Zhou R, Qiao SZ. An Fe/N co-doped graphitic carbon bulb for high-performance oxygen reduction reaction. Chem Commun. 2015;51(35):7516-9.

20. Hu H, Han L, Yu M, Wang Z, Lou XW. Metal-organic-framework-engaged formation of Co nanoparticle-embedded carbon@Co9S8 double-shelled nanocages for efficient oxygen reduction. Energy Environ Sci. 2016;9(1):107-11.

21. Jiao Y, Zheng Y, Davey K, Qiao S-Z. Activity origin and catalyst design principles for electrocatalytic hydrogen evolution on heteroatom-doped graphene. Nat Energy. 2016;1:16130.

22. Yang T, Liu J, Zhou R, Chen Z, Xu H, Qiao SZ, et al. N-doped mesoporous carbon spheres as the oxygen reduction reaction catalysts. J Mater Chem A. 2014;2(42):18139-46.

23. Dai L, Chang DW, Baek J-B, Lu W. Carbon Nanomaterials for Advanced Energy Conversion and Storage. Small. 2012;8(8):1130-66.

24. Xu P, Zeng GM, Huang DL, Feng CL, Hu S, Zhao MH, et al. Use of iron oxide nanomaterials in wastewater treatment: A review. Sci Total Environ. 2012;424:1-10.

25. Sun M, Zhang G, Liu H, Liu Y, Li J. α- and γ-Fe2O3 nanoparticle/nitrogen doped carbon nanotube catalysts for high-performance oxygen reduction reaction. Sci China Mater. 2015;58(9):683-92.

26. Kim IT, Magasinski A, Jacob K, Yushin G, Tannenbaum R. Synthesis and electrochemical performance of reduced graphene oxide/maghemite composite anode for lithium ion batteries. Carbon. 2013;52:56-64.

27. Li N, Zhang J, Tian Y, Zhao J, Zhang J, Zuo W. Precisely controlled fabrication of magnetic 3D γ-Fe2O3@ZnO core-shell photocatalyst with enhanced activity: Ciprofloxacin degradation and mechanism insight. Chem Eng J. 2017;308:377-85.

28. Hu J, Li W, Liu C, Tang H, Liu T, Guo H, et al. The formation and mechanism of nano-monocrystalline [gamma]-Fe2O3 with graphene-shell for high-performance lithium ion batteries. RSC Advances. 2016;6(57):51777-82.

29. Son MY, Hong YJ, Lee J-K, Chan Kang Y. One-pot synthesis of Fe2O3 yolk-shell particles with two, three, and four shells for application as an anode material in lithium-ion batteries. Nanoscale. 2013;5(23):11592-7.

30. Du N, Chen Y, Zhai C, Zhang H, Yang D. Layer-by-layer synthesis of [gamma]-Fe2O3@SnO2@C porous core-shell nanorods with high reversible capacity in lithium-ion batteries. Nanoscale. 2013;5(11):4744-50.

31. Zhang M, Liu E, Cao T, Wang H, Shi C, Li J, et al. Sandwiched graphene inserted with graphene-encapsulated yolk-shell [gamma]-Fe2O3 nanoparticles for efficient lithium ion storage. J Mater Chem A. 2017;5(15):7035-42.

32. Gawande MB, Goswami A, Asefa T, Guo H, Biradar AV, Peng D-L, et al. Core-shell nanoparticles: synthesis and applications in catalysis and electrocatalysis. Chem Soc Rev. 2015;44(21):7540-90.

33. Sun Q, Zhang X-Q, Wang Y, Lu A-H. Recent progress on core-shell nanocatalysts. Chin J Catal. 2015;36(5):683-91.

34. Li Z, Li M, Bian Z, Kathiraser Y, Kawi S. Design of highly stable and selective core/yolk–shell nanocatalysts—A review. Appl Catal, B. 2016;188:324-41.

35. Boyjoo Y, Wang M, Pareek VK, Liu J, Jaroniec M. Synthesis and applications of porous non-silica metal oxide submicrospheres. Chem Soc Rev. 2016;45(21):6013-47.

36. Su C, Wang W, Chen Y, Yang G, Xu X, Tadé MO, et al. SrCo0.9Ti0.1O3−δ As a New Electrocatalyst for the Oxygen Evolution Reaction in Alkaline Electrolyte with Stable Performance. ACS Appl Mater Interfaces. 2015;7(32):17663-70.

37. Anderson BD, Tracy JB. Nanoparticle conversion chemistry: Kirkendall effect, galvanic exchange, and anion exchange. Nanoscale. 2014;6(21):12195-216.

38. Deng D, Yu L, Chen X, Wang G, Jin L, Pan X, et al. Iron Encapsulated within Pod-like Carbon Nanotubes for Oxygen Reduction Reaction. Angew Chem Int Ed. 2013;52(1):371-5.

39. Wu X, Yu X, Lin Z, Huang J, Cao L, Zhang B, et al. Nitrogen doped graphitic carbon ribbons from cellulose as non noble metal catalyst for oxygen reduction reaction. Int J Hydrogen Energy. 2016;41(32):14111-22.

40. Choi CH, Lee SY, Park SH, Woo SI. Highly active N-doped-CNTs grafted on Fe/C prepared by pyrolysis of dicyandiamide on Fe2O3/C for electrochemical oxygen reduction reaction. Appl Catal, B. 2011;103(3–4):362-8.

Chapter 5: Ni and Co attached Cu/Cu_2O@C core-shell nanoparticles

Abstract

Core-shell structured metal cores encapsulated within carbon shell Ni-Cu/Cu_2O@C and Co-Cu/Cu_2O@C particles are successfully synthesized via a simple fabrication method using copper oxide (CuO) as the base particles. Resorcinol-formaldehyde (RF) layer is deposited uniformly outside base particles and converted into carbon during annealing process under nitrogen gas flow. Nickel nitrate and cobalt nitrate solutions are used to attach Ni and Co ions onto RF layer via pyrolysis, respectively. CuO particles are reduced at elevated temperature to Cu/Cu_2O particles via the redox reaction between CuO and carbon shell and further reduce to Metallic Cu cores by increasing the calcination temperature. Electrochemcial examinations show that both Ni-Cu/Cu2O@C and Co-Cu/Cu2O@C particles exhibit relatively good catalytic activities towards ORR; however, in comparison, Co-Cu/Cu2O@C is even more active due to the co-existing ultra-fine Co_3O_4 nanoparticles.

5.1 Introduction

Modernization of living has put a great deal on the consumption of energy; due to limitation of fuel resources and bad environmental consequences of traditional energy production methods, mankind urges for a more sustainable and efficient way to generate energy to meet the ever-increasing demand. In recent years, scientists have paid enormous efforts in investigating the generation of clean energy. Although renewable energy has contributed in providing power to some extent, however it is far inadequate in amount and high in capital and maintenance costs. Thus, fuel cell as a form of energy conversion media which converts chemical energy into electricity has caught overwhelming attentions in the scientific community (1, 2). Oxygen reduction reaction (ORR) is the crucial oxygen electrode reaction in an eletrocatalytic fuel cell system acting as a limiting reaction due to its sluggish kinetics (1-10). Catalyst, a medium to boost the reaction rate of a process, is very crucial in a fuel cell system. Noble metals were intensively investigated for ORR

process, especially platinum (Pt) and Pt based alloy. By far, Pt is still the most efficient catalyst towards electrochemical reactions; however, the drawbacks of instability, scarcity and high in cost are the main challenges for commercialization of such energy conversation technology (2, 6, 11-16). Therefore, researchers started seeking alternatives to reduce the percentages of Pt participating in the catalysts or replace Pt based catalysts with non-noble metals.

Transition metals, such as Fe, Cu, Ni, Co, Mn, show promising electrocatalytic abilities towards reduction of O_2 process in both acidic and alkaline solutions (9, 15, 17-20). Recently, many research works have been done in fabricating such nanoparticles for fuel cell reactions and proved to exhibit excellent electrocatalytic activities, such as Cu doped Fe@Fe_2O_3 yolk-shell nanocores encapsulated within carbon shell (Cu-Fe@Fe2O3@C) (8), Cu loaded on nitrogen on carbon materials (Cu–N–C) (21), transition metal ion-chelating ordered mesoporous carbon/multi-walled carbon nanotube (TM-OMC/CNT) (22), Co nanoparticle-embedded carbon@Co_9S_8 rattle type double-shelled nanocages (23), Co_3O_4 nanoparticles assembled on a polypyrrole/graphene oxide electrocatalyst (Co_3O_4/Ppy/GO) (24), and Fe, Cu-doped bamboo-like carbon nanotubes (Fe-Cu-N/C) (25). In addition, bimetallic particles in nano-scale are extremely favourable by owning the potential of being bifunctional catalysts in energy conversion and storage systems.

Rational architecture design of nanoparticles has been found to be equivalently important as material selection for improving catalytic performance. Over last decade, core-shell and yolk-shell structured nanocatalysts are the popular ones investigated in a wide range of applications. These structures have many indubitable advantages for catalysing, such as shell protects active cores from deactivation and agglomeration; controllable diffusion rate through tailoring the porosity of shell; and attach functional groups onto shell or core for achieving cascade reactions (2, 26-28). The usual core-shell and yolk-shell nanocatalyst consists one or multiple active cores within an inert or functionalized shell. Carbon is a popular shell material especially for electrode reactions. Carbon shell possesses ability in promoting synergistic effects between itself and active metal or metal oxide cores to accelerate the reduction process (29).

Herein, in this study we present a facile synthesis method to fabricate Ni-Cu/Cu_2O@C and Co-Cu/Cu_2O@C core-shell metal cores encapsulated within carbon

shell as a potential catalysts applying in electrode reactions for fuel cell system. CuO particles were firstly synthesized as base template coated with a layer of resorcinol-formaldehyde and transferred into Cu/Cu_2O core-shell structured cores via carbonization under nitrogen gas flow, as shown in Scheme 5.1. The electrochemical catalytic activity towards oxygen reduction process of all as-prepared catalysts were evaluated in alkaline medium, exhibiting excellent catalytic performances. The simple fabrication process and abundant raw materials make these catalysts possible to be produced commercially in large scale; with further modifications, it is believed to have potential to replace precious metal nanoparticles for energy related applications.

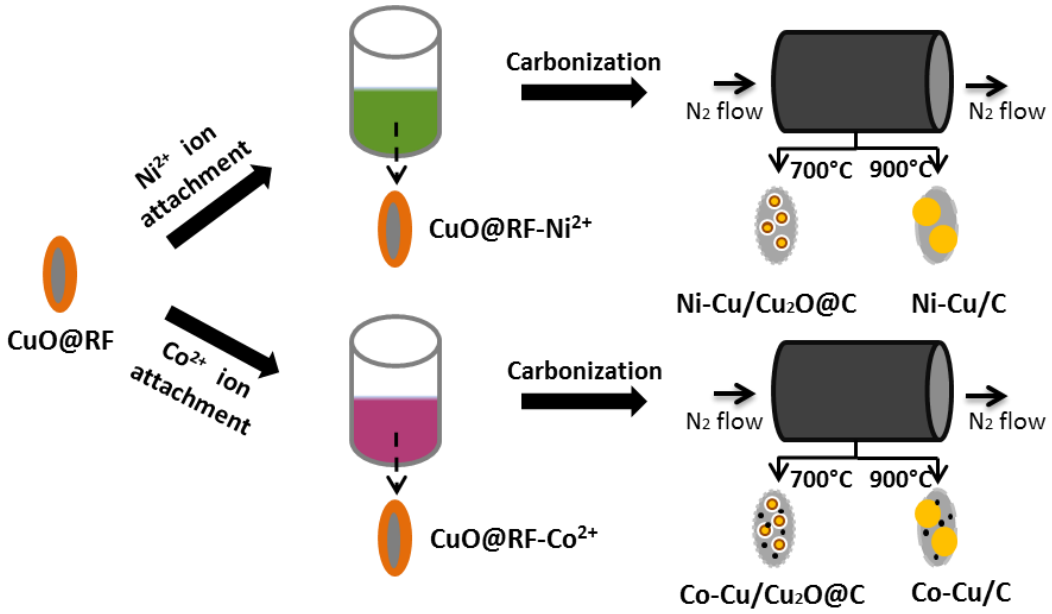

Scheme 5.1: Schematic illustration of synthesis of Ni-Cu/Cu_2O@C and Ni-Cu/C, Co-Cu/Cu_2O@C and Co-Cu/C particles.

5.2 Materials and Methods

5.2.1 Chemicals and reagents

Nickel (II) acetate tetrahydrate (99.99%), cobalt (II) acetate tetrahydrate (99.99%) were purchased from Sigma-Aldrich Company and used as supplied. Water was purified by a Milli Q system and had an electrical resistance of 18 MΩ•cm.

5.2.2 Preparation of Ni-Cu/Cu_2O@C and Ni-Cu/C, Co-Cu/Cu_2O@C and Co-Cu/C particles

Rod-shaped copper oxide encapsulated within resorcinol-formaldehyde shell (CuO@RF) core-shell particles were synthesized according to our previous work.(8) As-prepared 0.2g of CuO@RF particles were dispersed into 50 ml of nickel (II) acetate tetrahydrate solution (0.1 mole L^{-1}) under sonication. Then such mixture was magnetically stirred at room temperature for at least 10 hour. Ni^{2+} attached particles (CuO@RF-Ni^{2+}) were washed three times with water and collected through centrifugations, and dried at 70 °C in an electrical oven. The dried CuO@RF-Ni2+ particles were calcined in a tube furnace at 700 °C and 900 °C under nitrogen gas flow to produce Ni-Cu/Cu2O@C and Ni-Cu/C, respectively. The preparation procedures of Co-Cu/Cu_2O@C and Co-Cu/C particles are identical to nickel samples above, only replace the nickel (II) acetate tetrahydrate solution (0.1 mole L^{-1}) with cobalt (II) acetate tetrahydrate solution (0.1 mole L^{-1}).

5.2.3 Characterisation

The High Resolution Transmission Electron Microscopy (HRTEM) images were obtained with a JEOL 2100 microscopy operated at 120 KV. Transmission Electron Microscopy (TEM) images, High Angle Annular Dark Field Scanning Transmission Electron Microscopy (HAADF-STEM) images and Energy-dispersive x-ray Spectroscopy (EDS) element mappings and spectrums were acquired using a FEI Titan G2 80-200 TEM/STEM with ChemiSTEM Technology operated at 200 KV. Scanning Electron Microscopy (SEM) images were taken with a Zeiss 1555 VP-FESEM at an operating voltage at 3 KV. Sample for above measurements was prepared by dispersing particles into absolute ethanol under ultrasonic treatment and placing a drop of such suspension onto a carbon coated gold grid for TEM and an

aluminium stub for SEM, then allow the ethanol to evaporate naturally before carrying out the measurements. Micromeritics TriStar (II) surface area and porosity analyser was used to measure the nitrogen adsorption and desorption isotherms. The specific surface areas of samples were calculated by Brunauer-Emmett-Teller (BET) method from the adsorption isotherms. The samples were degassed at 160 °C overnight before such analysis was performed. X-ray diffraction (XRD) measurements were obtained using a Briker-AXS D8 Advance Diffractometer with Cu Kα radiation (40 KV, 40 mA) and a LynxEye position sensitive detector. Information on crystalline phases was confirmed against the database of Joint Committee on Powder Diffraction Standards (JCPDS) files.

5.2.4 Electrochemical catalytic measurements

The electrochemical measurements of oxygen reduction reaction (ORR) on all synthesized catalysts were conducted in 0.1 M KOH electrolyte saturated with O_2 in a three-electrode system controlled by a Gamry electrochemical workstation (Reference 3000) with a glassy carbon rotating disk electrode (RDE, Pine Instrument Company, USA). An Ag/AgCl (KCl sat.) and a Pt wire were used as the counter electrode and the reference electrode, respectively. The detail preparation method of catalyst-coated electrode was descripted elsewhere.(30) 2 mg of catalyst was dispersed into mixture of Nafion® 117 solution and isopropanol via ultrasonic treatment. Then such homogeneous catalyst ink was droped onto RDE (5.0 mm in diameter) and dried naturally. All measured potentials against the Ag/AgCl electrode were calibrated to the reversible hydrogen electrode (RHE) readings according to the Equation (5.1):

$$E_{RHE} = E_{Ag/AgCl} + 0.059\,pH + 0.197 \quad (5.1)$$

The electrochemical testing of cyclic voltammetry (CV) measurements were performed at a scan rate of of 50 mV s^{-1} and linear sweep voltammetry (LSV) measurements were conducted at a sweep rate of 10 mV s^{-1} with rotating speeds from 400 to 2500 rpm. The overall electron transfer numbers per oxygen molecule in a typical ORR process were measured using the slopes of the linear fit lines in Kouteckey-Levich (K-L) plots (J^{-1} vs $\omega^{-1/2}$) based on the following Equations (5.2):

$$1/J = 1/J_K + 1/B\omega^{1/2} \quad (5.2)$$

Where J is the measured current density, J_k is the kinetic current density; ω is the electrode rotating speed in rpm and B is the reciprocal slopes of K-L plots. B value can be calculated using Equation (3) where n is the transferred electro number per oxygen molecule, F is Faraday constant (96485 C mol^{-1}) and C_0 is the bulk concentration of O_2. The constant value 0.2 was used when disk rotating speed is in rpm.

$$B = 0.2nFC_0D_0^{2/3}\nu^{-1/6} \quad (5.3)$$

The OER activity was evaluated using the stable LSV measurements after iR correction on a rotating disk electrode with rotating speed at 1600 rpm and scan rate 10 mV s^{-1}.

5.3 Results and Discussion

5.3.1 Characterisations of Ni-Cu/Cu_2O@C, Ni-Cu/C, Co-Cu/Cu_2O@C and Co-Cu/C particles

The brush-liked CuO particles encapsulated within resorcinol formaldehyde (RF) layer were synthesized using a simple synthesis method as descripted in our previous work.(8) Through simple annealing step under nitrogen gas environment brush-liked CuO nanoparticles were transformed into spherical nano-cores. Figure 5.1 indicates the morphological and compositional information of Ni-Cu/Cu_2O@C. The SEM image (Figure 5.1 (a)) shows that Ni-Cu/Cu_2O@C particles possess relatively smooth shell surface, and most of the carbon shells are in excellent condition despite only few small holes. The appearance of these tiny holes is believed to be that a few core nanoparticles formed at the place very close to carbon outer surface and escaped to aggregate into bigger metal particles during calcination. TEM image (Figure 5.1 (b)) provides the morphology inside the carbon shell; the core nanoparticles are very uniform in size, approximately 50 nm in diameter and the thickness of carbon shell is about 20 nm. The composition of Ni-Cu/Cu_2O@C is determined using the XRD result in Figure 5.9 (a) and EDS mapping in Figure 5.1 (c). The XRD measurement indicates that Cu and Cu_2O peaks are detected, and Cu has higher intensity than Cu_2O. EDS mapping images depict that copper element dominates the core

nanoparticles and nickel element appears at the surface of cores with a patch showing stronger nickel signal on each core. Moreover, oxygen element can be only seen at the outer area of copper cores which confirms the existence of Cu_2O at outer part of nano-cores. None nickel related peak is shown in XRD result could be because that nickel amount present in the sample is too small. This can be approved by the EDS spectrum of selected area showing in Figure 5.2, the nickel peak presents in the spectrum is almost negligible in contrast with other elements. Therefore, the compositional structure of a core is that metallic Cu presents in the centre with a layer of Cu2O outside, and small amount of Ni doped on the particle with tiny patch on the core surface.

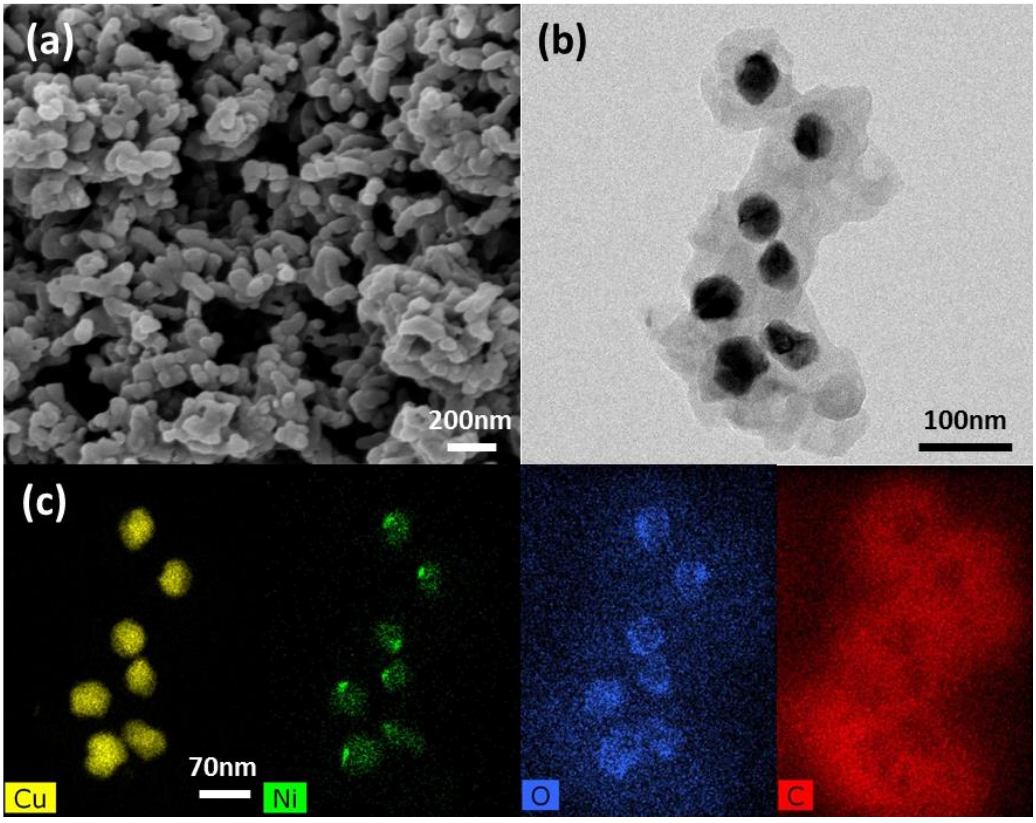

Figure 5.1**:** (a) SEM image of Ni-Cu/Cu_2O@C core-shell particles; (b) TEM image of Ni-Cu/Cu_2O@C core-shell particles; (c) EDS mapping of Ni-Cu/Cu_2O@C core-shell particles.

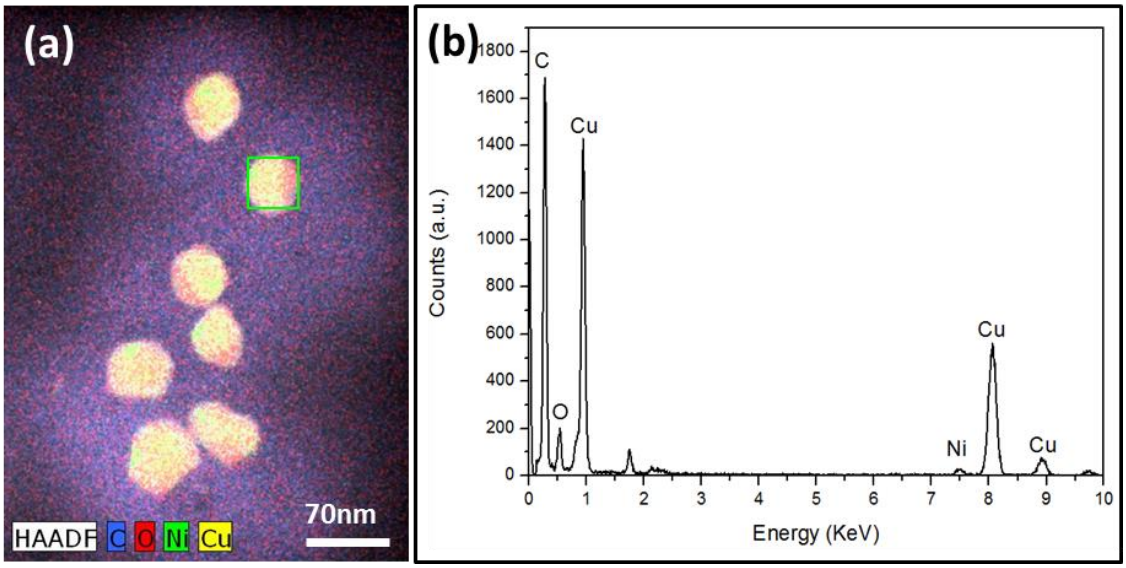

Figure 5.2: (a) EDS element distribution map of Ni-Cu/Cu2O@C; (b) EDS spectrum of selected area of Ni-Cu/Cu2O@C.

The morphology of sample altered when the carbonization temperature rose to 900 °C as seen in Figure 5.3. In contrast with Ni-Cu/Cu_2O@C, the architecture of samples changed from metal nano-cores carbon shell core-shell structure to metal particles with carbon support structure. In Figure 5.3 (a), the SEM image clearly shows that large metal particles formed and co-exist with very broken carbon particles. These large metal particles are approximate 200 nm in diameter as seen in the TEM image (Figure 5.3 (b)). The formation of this morphology is expect to be that when carbonization temperature increases further, nano-cores aggregate within the shell and at the same time the carbon shell become thinner due to the consumption of oxygen from Cu_2O layer, then the cores break the carbon shells and aggregate further into very large metal particles leaving hollow carbon particles aside. The EDS mapping in Figure 5.3 (c) shows similar elemental distribution information to Ni-Cu/Cu_2O@C. However, the XRD result in Figure 5.9 (b) indicates that Cu dominates the sample with very high intensity and only two low peaks reflecting Cu_2O. Therefore, the amount of Cu_2O could be considered as very few in comparison to metallic Cu. This statement can also be confirmed by the EDS spectrum of core particle showing in Figure 5.4, the oxygen peak is very low in counts almost to an extent to be omitted. Therefore, it can be said that the metal particles appearing in Ni-Cu/C are mainly metallic Cu. Moreover, the nickel patches aggregate too as

copper cores assemble. The HRTEM indicates that these nickel patches are NiO having lattice spacing of 0.24 nm against the (111) planes.

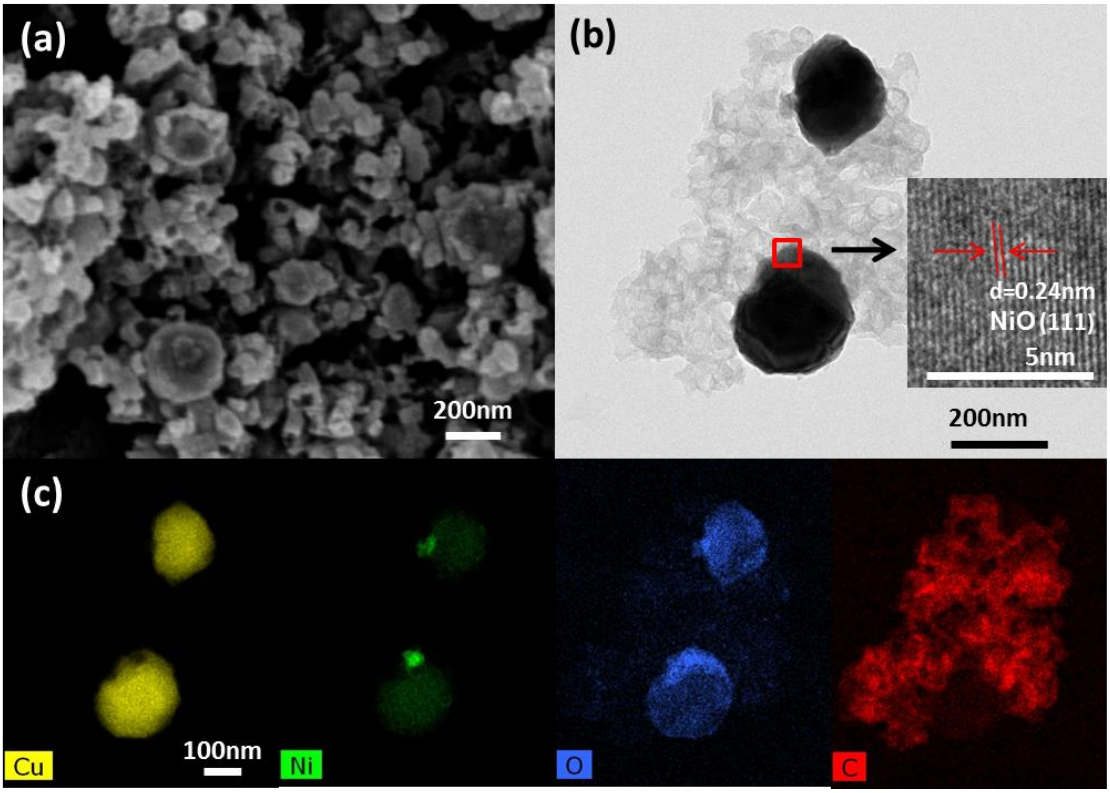

Figure 5.3: (a) SEM image of Ni-Cu/C particles; (b) TEM image of Ni-Cu/C particles with insert of HRTEM image of NiO; (c) EDS mapping of Ni-Cu/C particles.

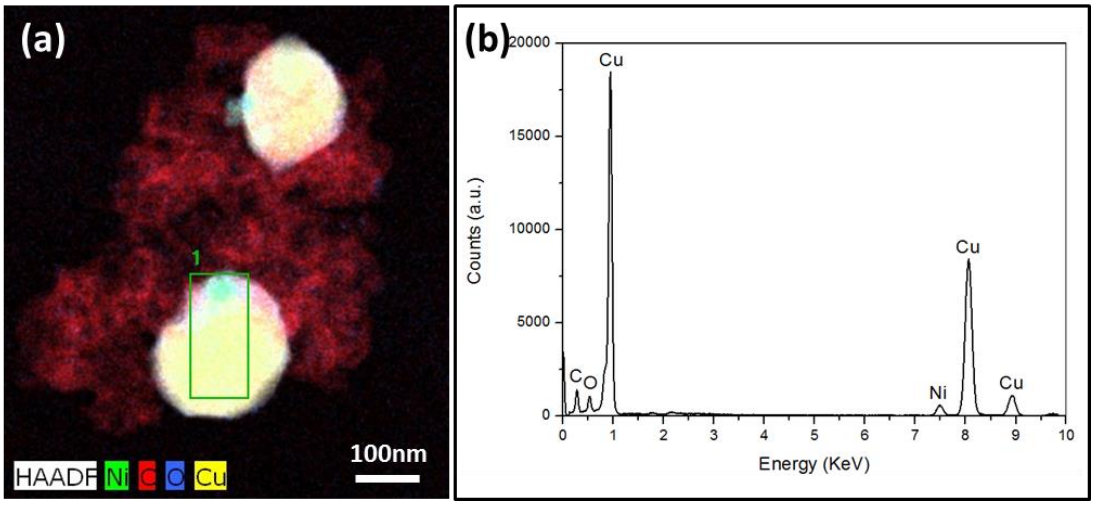

Figure 5.4: (a) EDS element distribution map of Ni-Cu/C; (b) EDS spectrum of selected area of Ni-Cu@C.

CuO@RF-Co sample was calcined under nitrogen flow as well to produce Co attached Cu, Cu2O and C catalysts (Co-Cu/Cu_2O@C). As seen in Figure 5.5 (b), at 700 °C carbonization temperature, nano-cores in a size range from 50 – 80 nm formed together with some very tiny ones within the carbon shell. Moreover, the carbon shell is much thinner and more broken comparing with Ni-Cu/Cu_2O@C sample. This fact is also clearly shown in the SEM image (Figure 5.5 (a)); more and bigger holes appeared in this sample. The compositional information of Co-Cu/Cu_2O@C was determined via the XRD measurement in Figure 5.9 (c), HRTEM images in Figure 5.5 (c) and EDS mapping in Figure 5.5 (d). This sample processes similar composition to Ni-Cu/Cu_2O@C, obvious Cu and Cu_2O peaks appear in the XRD measurement. The HRTEM image at selected area 1 (Figure 5.5 (c) (1)) of the outer part of a nano-core indicates a typical Cu_2O lattice spacing of 0.25 nm which corresponds to the (111) lattice planes; and the HRTEM image of selected area 2 (Figure 5.5 (c) (2)) of a tiny particle shows a lattice spacing of 0.24 nm reflecting to (311) lattice planes for cobalt oxide Co_3O_4. As shown in EDS images, the large size cores show copper and oxygen signals having oxygen only exists at their outer layers, the cobalt and oxygen signals appear at the small particles and also at the surface of large nano-cores. Therefore, it can be identified that this catalyst has Co doped large Cu/Cu2O cores and very small Co_3O_4 nanoparticles encapsulated within carbon shell.

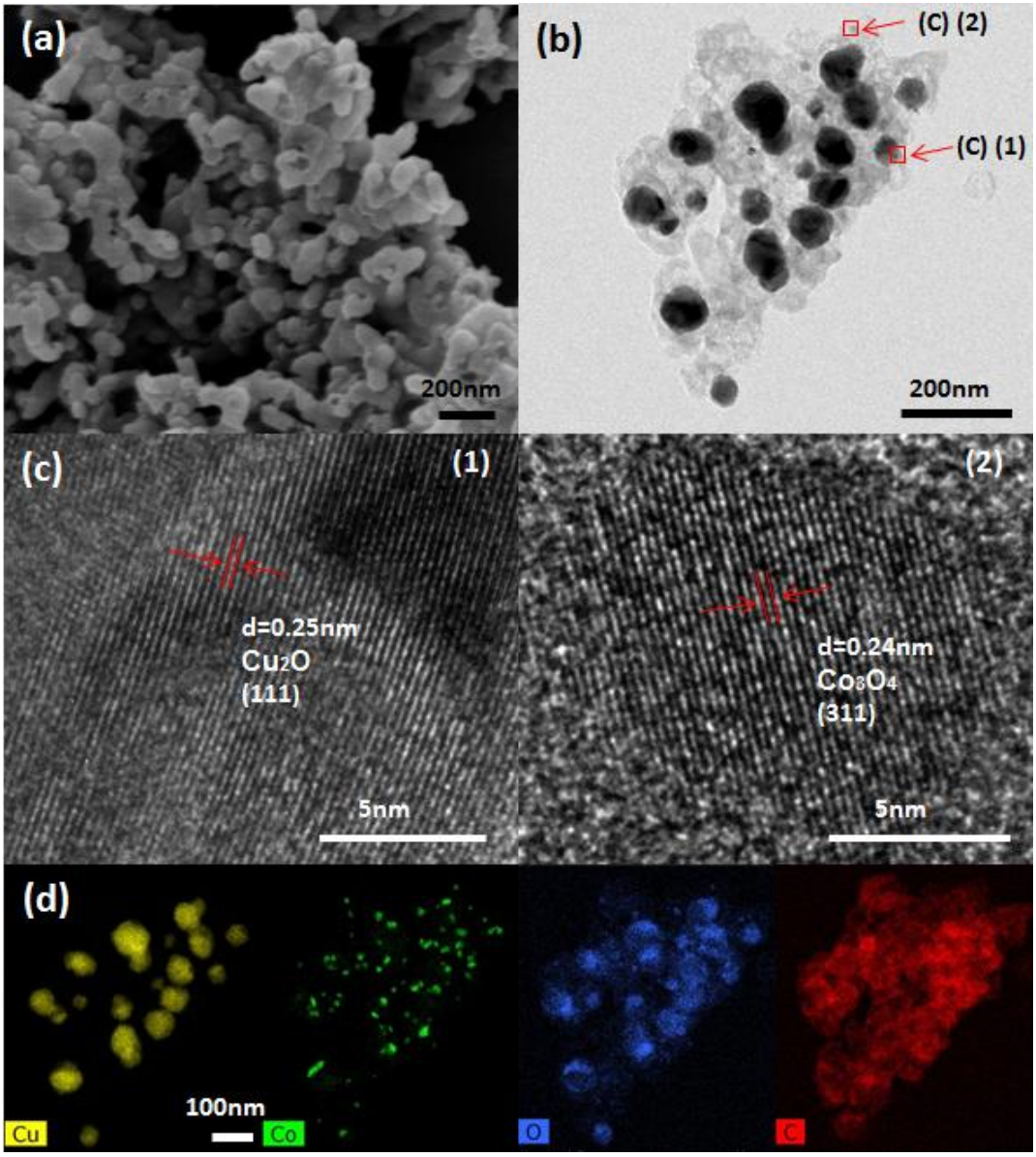

Figure 5.5**:** (a) SEM image of Co-Cu/Cu_2O@C core-shell particles; (b) TEM image of Co-Cu/Cu_2O@C core-shell particles; (c) HRTEM images; (d) EDS mapping of Co-Cu/Cu_2O@C core-shell particles.

Such Co attached sample was also calcined at 900 °C. Similar to Ni attached sample, the structural morphology of this sample changed from core-shell structure to metal particles with carbon support structure as shown in Figure 5.6 (a) and (b). The exposed metal particles possess their size in range from 180 – 220 nm. Moreover, in comparison with Co-Cu/Cu2O@C sample, as Cu particles aggregate, the Co patch on these particles assemble toward each other forming slightly bigger ones as well, however, the scattered tiny Co nanoparticles seem remain unchanged. Again, according to the XRD result in Figure 5.9 (d), this sample has the almost identical

composition as Ni-Cu/C, which confirms that the large particles are metallic Cu particles with almost negligible Cu_2O layer outside them. The oxygen signals from EDS mapping in Figure 5.6 (c) appear at where cobalt signals are which further confirms that these small particles and also the patch attached on the Cu particles are Co_3O_4.

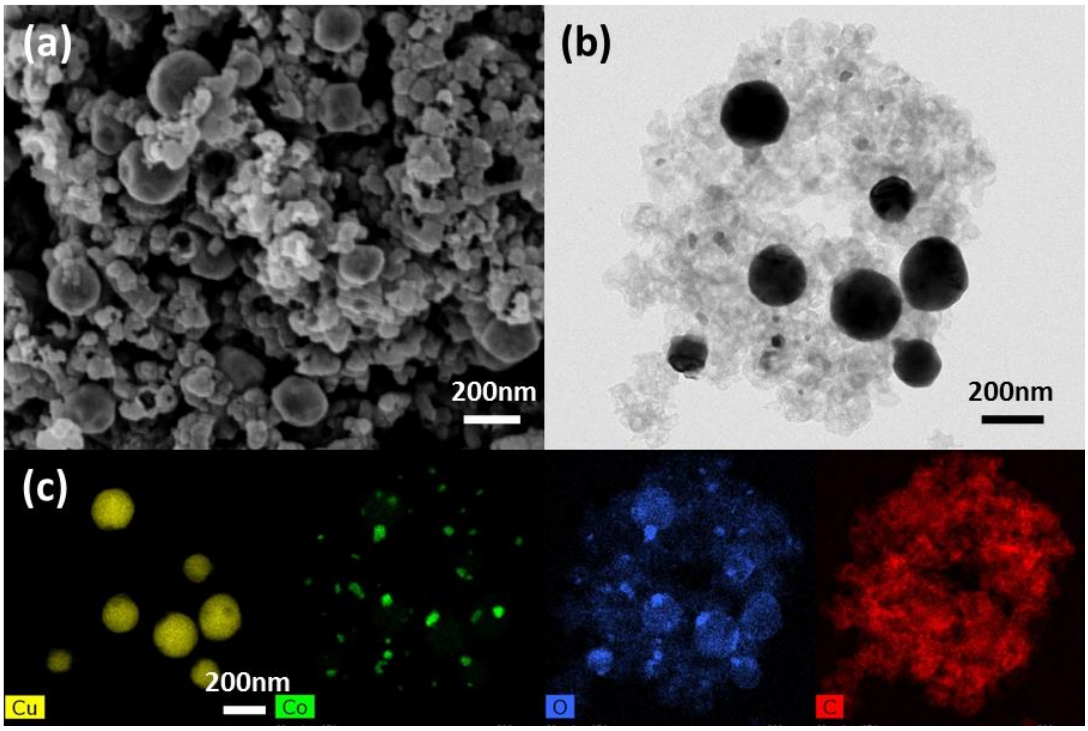

Figure 5.6**:** (a) SEM image of Co-Cu/C particles; (b) TEM image of Co-Cu/C particles; (c) EDS mapping of Co-Cu/C particles.

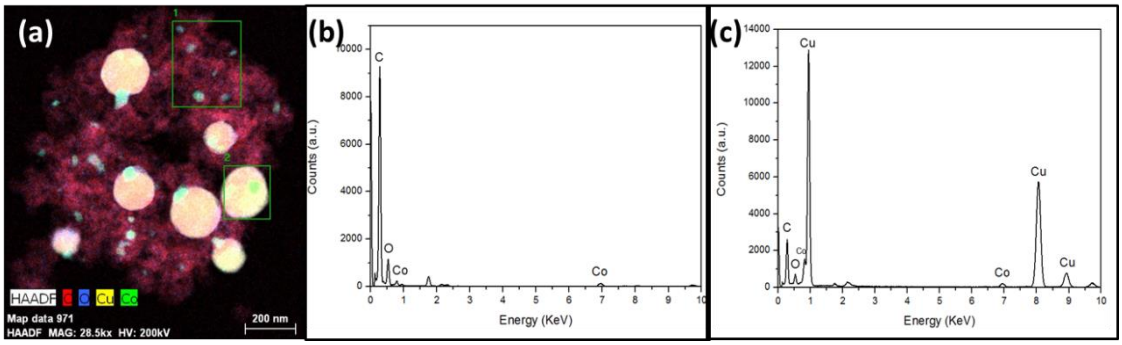

Figure 5.7: (a) EDS element distribution map of Co-Cu/C; (b) EDS spectrum of selected area of Co-Cu@C.

As the carbonization temperature increase, the carbon materials transform from amorphous carbon to slight graphitic carbon. To compare the graphitic degrees between sample Ni-Cu/C and Co-Cu/C, Co attached sample seems to have higher graphitic level than Ni attached sample as shown in Figure 5.8.

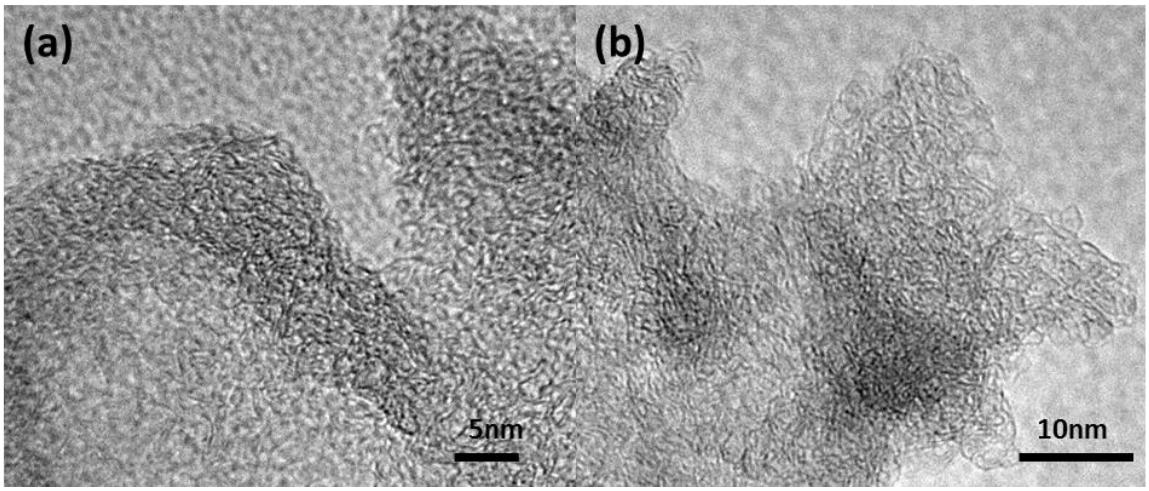

Figure 5.8**:** (a) HRTEM image of carbon shell of Ni-Cu/C sample; (b) HRTEM image of carbon shell of Co-Cu/C sample.

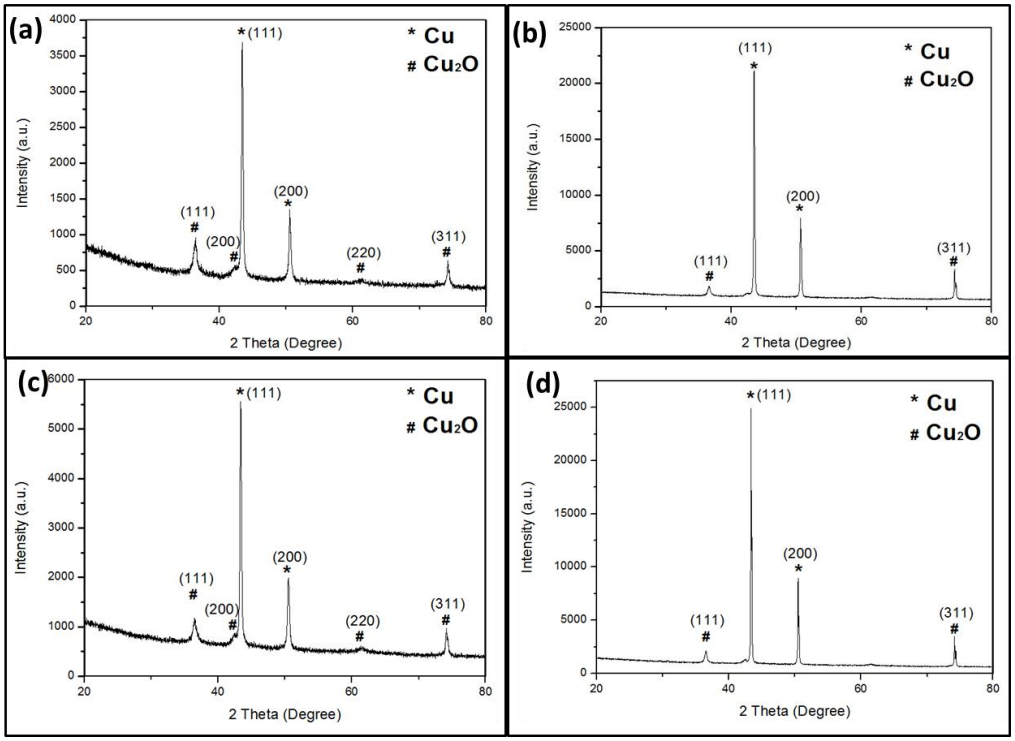

Figure 5.9: XRD patterns of (a) Ni-Cu/Cu2O@C core-shell particles; (b) Ni-Cu/C particles; (c) Co-Cu/Cu2O@C core-shell particles; (d) Co-Cu/C particles.

5.3.2 Electrocatalytic performance

The electrocatalytic activities of as-prepared samples toward ORR were initially evaluated by cyclic voltammetry (CV) tests in O_2-saturated KOH solutions, as shown in Figure 5.10 (a). It is clear that there is a notable cathodic peak in each CV curve which identifies the electrochemical catalytic ability for the reduction process. A substantial reduction of Co-Cu/Cu_2O@C appeared at approximately 0.73 V (vs. reversible hydrogen electrode (RHE)) which is the most positive peak, and followed by Co-Cu@C showing slightly negative peak reading at 0.7 V. In contrast to Ni-Cu/Cu_2O@C and Ni-Cu@C, Co attached samples are more active by having faster appearance of cathodic peaks in the CV measurements. The similar catalytic activities trend was further proofed via linear sweep voltammetry (LSV) measurements which were conducted in a standard three-electrode system using a rotating disk electrode (RDE) at a scan rate of 10 mV s^{-1}, and results were recorded at different rotating speeds from 400 to 2500 rpm, as shown in Figure 5.11. Figure 5.10 (b) indicates the combined LSV curves of all catalysts at rotating speed of 1600 rpm. It can be clearly seen that Co attached catalysts have more positive onset potentials at about 0.86 V than the onset potentials of Ni attached catalysts approximately 0.82 V. Even through Ni-Cu/Cu_2O@C and Co-Cu/Cu_2O@C catalysts show the similar diffusion-limiting current density around 5.2 mA cm^{-2}, Co-Cu/Cu_2O@C delivered the highest half-wave potential at 0.69 V. To further evaluate the ORR process, the electron-transfer numbers (n) of all catalysts were calculated using linear fitted Kouteckey-Levich (K-L) plots (J^{-1} vs $\omega^{-1/2}$) as shown in Figure 5.12 and Figure 5.10 (c). The n values of sample Ni-Cu/Cu_2O@C and Co-Cu/Cu_2O@C were 3.69-4.00 and 3.72-3.96, respectively, demonstrates that oxygen reduction processes over such two catalysts favoured by four-electron ORR pathway. Therefore, according to all electrochemical measurements above, it is clear that both Ni-Cu/Cu_2O@C and Co-Cu/Cu_2O@C core-shell structured catalysts performed excellently towards ORR, and Co-Cu/Cu_2O@C exhibited even better catalytic ability by owning more positive cathodic peak and higher onset and half-wave potentials. It is believed that the bimetallic system, existence of Cu_2O, small metal particle size and synergetic effects of core-shell structure could reasonably attribute to the good catalytic activity for reducing O_2 into OH^- (1, 9, 14, 29, 31). In addition, the ultra-small Co_3O_4 nanoparticles not only provide larger catalytic contacting area, Co_3O_4

itself also possesses great electrocatalytic ability for cathodic reactions (31, 32). Thus, these factors possibly result the better performance of Co-Cu/Cu_2O@C sample than the others. Carbon supported catalysts showed much lower catalytic activities and electron-transfer numbers, especially Ni-Cu@C, thus this further confirms the impact of core-shell architecture and existence of small Co_3O_4 nanoparticles to an excellent ORR process. Moreover, all catalysts were also tested for oxygen evolution reaction (OER) in alkaline solution with scan rate at 10 mV s^{-1}, the OER curves as indicated in Figure 5.10 (d), it can be seen that almost identical activity trend in compare with ORR. Overall, the electrochemical catalytic activity of all catalysts increases in the order of Ni-Cu@C < Co-Cu@C < Ni-Cu/Cu_2O@C < Co-Cu/Cu_2O@C.

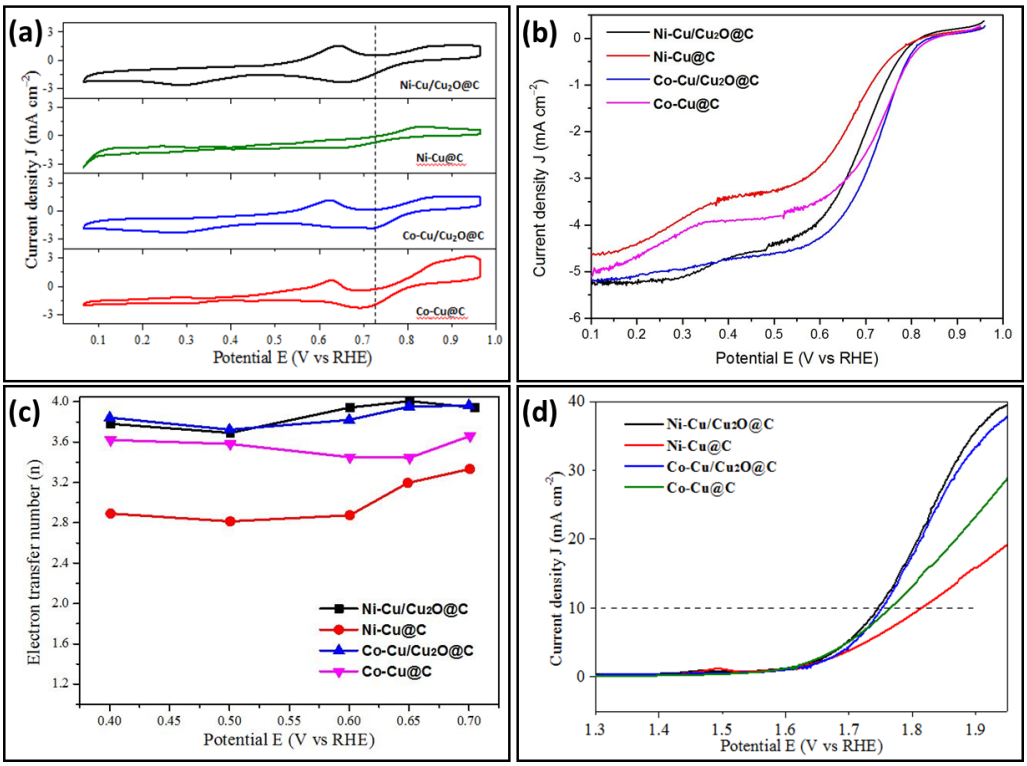

Figure 5.10: (a) CV curves of Ni-Cu/Cu_2O@C, Ni-Cu@C, Co-Cu/Cu_2O@C and Co-Cu@C in O2-saturated 0.1 M KOH solution at a scan rate of 50 mV s-1; (b) LSV curves of all catalysts on the RDE at rotating speed 1600 rpm in O_2-saturated 0.1 M KOH solution at a scan rate of 10 mV s^{-1}; (c) Electron-transfer numbers (n) of all catalysts calculated by their K-L plots; (d) iR-corrected OER polarization curves of Ni-Cu/Cu_2O@C, Ni-Cu@C, Co-Cu/Cu_2O@C and Co-Cu@C.

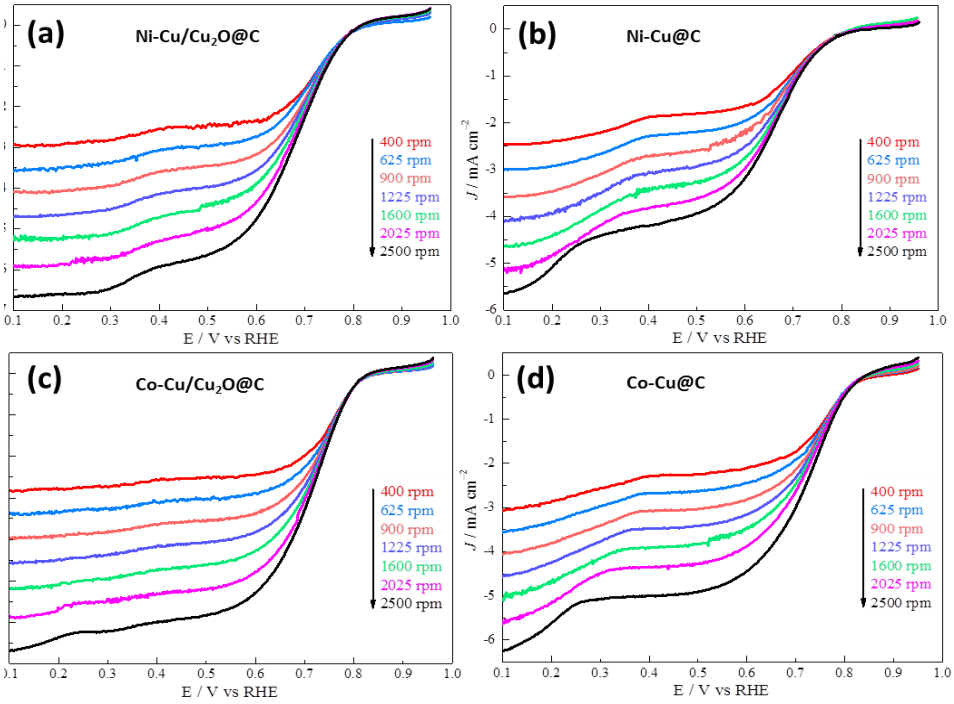

Figure 5.11: LSV curves of (a) Ni-Cu/Cu2O@C, (b) Ni-Cu@C, (c) Co-Cu/Cu2O@C and (d) Co-Cu @C on the RDE at rotating speed from 400 rpm to 2500 rpm in O2-saturated 0.1 M KOH solution at a scan rate of 10 mV s-1.

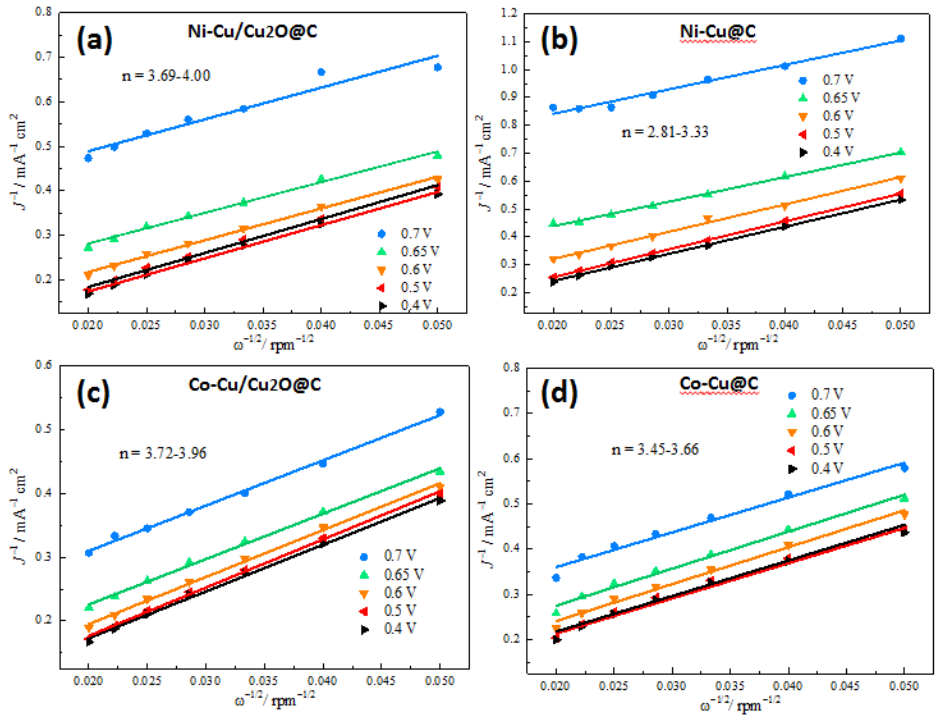

Figure 5.12: K-L plots (J–1 vs ω–1/2) of (a) Ni-Cu/Cu2O@C, (b) Ni-Cu@C, (c) Co-Cu/Cu2O@C and (d) Co-Cu @C at different potentials.

5.4 Conclusions

Ni and Co attached Cu/Cu_2O and Cu cores encapsulated within carbon shell particles have been successfully prepared via a simple synthesis method. The CuO base particles were reduced to Cu_2O and Cu cores through the carbonization process and very tiny Co_3O_4 nanoparticles formed in the Co attached catalysts. Such facile fabrication method is believed could be advantageous applying for reducing other metal oxide nanoparticles. Electrochemical catalytic activity of all as-prepared catalysts was evaluated through ORR and OER. $Co\text{-}Cu/Cu_2O@C$ nanocatalyst exhibited the best electrochemical performance, because of its small Cu/Cu_2O particles size, synergetic effects of core-shell structure and the formation of ultra-fine Co_3O_4 nanoparticles.

References

1. Shao M, Chang Q, Dodelet J-P, Chenitz R. Recent Advances in Electrocatalysts for Oxygen Reduction Reaction. Chem Rev. 2016;116(6):3594-657.

2. Wang MW, Boyjoo Y, Pan J, Wang SB, Liu J. Advanced yolk-shell nanoparticles as nanoreactors for energy conversion. Chin J Catal. 2017;38(6):970-90.

3. Liu J, Jiao M, Lu L, Barkholtz HM, Li Y, Wang Y, et al. High performance platinum single atom electrocatalyst for oxygen reduction reaction. Nat Commun. 2017;8:15938.

4. Liu S, Wang Z, Zhou S, Yu F, Yu M, Chiang C-Y, et al. Metal–Organic-Framework-Derived Hybrid Carbon Nanocages as a Bifunctional Electrocatalyst for Oxygen Reduction and Evolution. Adv Mater. 2017;29(31):n/a-n/a.

5. Sun K, Xue J, Tai K, Dillon SJ. The Oxygen Reduction Reaction Rate of Metallic Nanoparticles during Catalyzed Oxidation. Sci Rep. 2017;7(1):7017.

6. Huo L, Liu B, Zhang G, Si R, Liu J, Zhang J. 2D Layered non-precious metal mesoporous electrocatalysts for enhanced oxygen reduction reaction. J Mater Chem A. 2017;5(10):4868-78.

7. Zhang X, Li K, Yan P, Liu Z, Pu L. N-type Cu2O doped activated carbon as catalyst for improving power generation of air cathode microbial fuel cells. Bioresour Technol. 2015;187:299-304.

8. Wang MW, Su C, Saunders M, Liang J, Shao ZP, Wang SB, et al. Yolk–Shell-Structured Cu/Fe@γ-Fe2O3 Nanoparticles Loaded Graphitic Porous Carbon for the Oxygen Reduction Reaction. Part Part Syst Charact. 2017:n/a-n/a.

9. Yan Y, Du JS, Gilroy KD, Yang D, Xia Y, Zhang H. Intermetallic Nanocrystals: Syntheses and Catalytic Applications. Adv Mater. 2017;29(14):n/a-n/a.

10. Wang J, Chen F, Jin Y, Lei Y, Johnston RL. One-Pot Synthesis of Dealloyed AuNi Nanodendrite as a Bifunctional Electrocatalyst for Oxygen Reduction and Borohydride Oxidation Reaction. Adv Funct Mater. 2017;27(23):n/a-n/a.

11. Wang W, Lei B, Guo S. Engineering Multimetallic Nanocrystals for Highly Efficient Oxygen Reduction Catalysts. Adv Energy Mater. 2016;6(17):n/a-n/a.

12. Zhao X, Li Y, Guo Y, Chen Y, Su Z, Zhang P. Coral-Like MoS2/Cu2O Porous Nanohybrid with Dual-Electrocatalyst Performances. Adv Mater Interfaces. 2016;3(23):n/a-n/a.

13. Zhang J, Zhao Z, Xia Z, Dai L. A metal-free bifunctional electrocatalyst for oxygen reduction and oxygen evolution reactions. Nat Nano. 2015;10(5):444-52.

14. Perez-Alonso FJ, McCarthy DN, Nierhoff A, Hernandez-Fernandez P, Strebel C, Stephens IEL, et al. The Effect of Size on the Oxygen Electroreduction Activity of Mass-Selected Platinum Nanoparticles. Angew Chem Int Ed. 2012;51(19):4641-3.

15. Tang J, Liu J, Torad NL, Kimura T, Yamauchi Y. Tailored design of functional nanoporous carbon materials toward fuel cell applications. Nano Today. 2014;9(3):305-23.

16. Aijaz A, Masa J, Rösler C, Xia W, Weide P, Botz AJR, et al. Co@Co3O4 Encapsulated in Carbon Nanotube-Grafted Nitrogen-Doped Carbon Polyhedra as an Advanced Bifunctional Oxygen Electrode. Angew Chem Int Ed. 2016;55(12):4087-91.

17. Zhang Z, Luo Z, Chen B, Wei C, Zhao J, Chen J, et al. One-Pot Synthesis of Highly Anisotropic Five-Fold-Twinned PtCu Nanoframes Used as a Bifunctional

Electrocatalyst for Oxygen Reduction and Methanol Oxidation. Adv Mater. 2016;28(39):8712-7.

18. Lee J-Y, Han S-B, Kwak D-H, Kim M-C, Lee S, Park J-Y, et al. Porous Cu-rich@Cu3Pt alloy catalyst with a low Pt loading for enhanced electrocatalytic reactions. J Alloys Compd. 2017;691:26-33.

19. Kong J, Cheng W. Recent advances in the rational design of electrocatalysts towards the oxygen reduction reaction. Chin J Catal. 2017;38(6):951-69.

20. Zhao Q, Zhang G, Xu G, Li Y, Liu B, Gong X, et al. Synthesis of highly active and dual-functional electrocatalysts for methanol oxidation and oxygen reduction reactions. Appl Surf Sci. 2016;389:181-9.

21. Kang YS, Heo Y, Kim P, Yoo SJ. Preparation and characterization of Cu–N–C electrocatalysts for oxygen reduction reaction in alkaline anion exchange membrane fuel cells. J Ind Eng Chem. 2017;52:35-41.

22. Dombrovskis JK, Palmqvist AEC. One-pot synthesis of transition metal ion-chelating ordered mesoporous carbon/carbon nanotube composites for active and durable fuel cell catalysts. J Power Sources. 2017;357:87-96.

23. Hu H, Han L, Yu M, Wang Z, Lou XW. Metal-organic-framework-engaged formation of Co nanoparticle-embedded carbon@Co9S8 double-shelled nanocages for efficient oxygen reduction. Energy Environ Sci. 2016;9(1):107-11.

24. Ren S, Guo Y, Ma S, Mao Q, Wu D, Yang Y, et al. Co3O4 nanoparticles assembled on polypyrrole/graphene oxide for electrochemical reduction of oxygen in alkaline media. Chin J Catal. 2017;38(7):1281-90.

25. Fan W, Li Z, You C, Zong X, Tian X, Miao S, et al. Binary Fe, Cu-doped bamboo-like carbon nanotubes as efficient catalyst for the oxygen reduction reaction. Nano Energy. 2017;37:187-94.

26. Gawande MB, Goswami A, Asefa T, Guo H, Biradar AV, Peng D-L, et al. Core-shell nanoparticles: synthesis and applications in catalysis and electrocatalysis. Chem Soc Rev. 2015;44(21):7540-90.

27. Liu J, Qiao SZ, Chen JS, Lou XW, Xing X, Lu GQ. Yolk/shell nanoparticles: new platforms for nanoreactors, drug delivery and lithium-ion batteries. Chem Commun. 2011;47(47):12578-91.

28. Mahata A, Pathak B. Bimetallic core-based cuboctahedral core-shell nanoclusters for the formation of hydrogen peroxide (2e- reduction) over water (4e-reduction): role of core metals. Nanoscale. 2017;9(27):9537-47.

29. Sun D, Ye L, Sun F, García H, Li Z. From Mixed-Metal MOFs to Carbon-Coated Core–Shell Metal Alloy@Metal Oxide Solid Solutions: Transformation of Co/Ni-MOF-74 to CoxNi1–x@CoyNi1–yO@C for the Oxygen Evolution Reaction. Inorg Chem. 2017;56(9):5203-9.

30. Tian W, Zhang H, Sun H, Suvorova A, Saunders M, Tade M, et al. Heteroatom (N or N-S)-Doping Induced Layered and Honeycomb Microstructures of Porous Carbons for CO2 Capture and Energy Applications. Adv Funct Mater. 2016;26(47):8651-61.

31. Li Q, Xu P, Zhang B, Tsai H, Zheng S, Wu G, et al. Structure-Dependent Electrocatalytic Properties of Cu2O Nanocrystals for Oxygen Reduction Reaction. J Phys Chem C. 2013;117(27):13872-8.

32. Vincent I, Bessarabov D. Electrochemical Characterization and Oxygen Reduction Kinetics of Cu-incorporated Cobalt Oxide Catalyst. Int J Electrochem Sci. 2016;11:8002-15.

Chapter 6: Synthesis of TiO_2@TiO_2 yolk-shell nanoparticles

Abstract

Yolk-shell TiO2@TiO2 particles have been fabricated through a four-step synthesis method using titanium(IV) butoxide as the titanium precursor and resorcinol-formaldehyde (RF) as the sacrificing template. The yolk-shell structure was created by removing RF layer via gentle calcination under air. The void size between yolk and shell could be simply tailored by adjusting the thickness of RF layer. A numbers of investigation of morphological effects of synthetic parameter are conducted. This well-designed semiconductor yolk-shell nanocatalyst is believed to be versatile in many catalytic applications.

6.1 Introduction

The environmental crisis has put mankind into a critical stage demanding immediate changes and improvements. Apart from desirable clean energy conversion and generation, usage of unlimited solar power has also been intensively investigated. Being a "green process, photocatalysis accelerates a chemical reaction by light which has caught overwhelmed attentions. Researchers and scientists paid great efforts in searching for the right catalytic materials which could be utilised under visible lights making catalysis happening naturally.

Titanium oxide (TiO_2), is a wide-band-gap metal oxide semiconductors, has been widely involved in many advanced structured nanocatalysts exhibiting outstanding catalytic activities towards many applications, such as photocatalytic degradation of pollutants, dye-sensitized solar cell, electrocatalytic reduction of CO_2 and also lithium-ion batteries (1-6). This material was firstly tested by Fujishima and Honda in 1972 for photocatalytic water splitting (4, 7, 8). Since then TiO_2 has undergone an intensive investigation on its various potentials in applications due to its advantages of abundance, stability and non-toxicity (3, 9-11). The two main phases of TiO_2 are anatase and rutile having the band gaps at 3.2 eV and 3.0 eV, respectively, and only can be photoactivated by UV irradiation (4% of natural sunlight) which makes bare TiO_2 very inefficient in catalysis (3, 12-14). However, it has been found that TiO_2 photocatalytic activity could be improved by limiting the charge recombination

through tuning the crystallinity, architecture, particle size, porosity and co-catalysts (8, 12, 15-18).

Here, in this chapter, I present a four-step synthesis method to fabricate spindle-like yolk-shell TiO_2@TiO_2 nanoparticles (as shown in Scheme 6.1) with several investigations of morphological effects of synthesis parameters. RF layer was used as the sacrificing template and removed via calcination to creative yolk-shell structure. This well-designed yolk-shell nanocatalyst is believed to have great potential in photocatalytic applications.

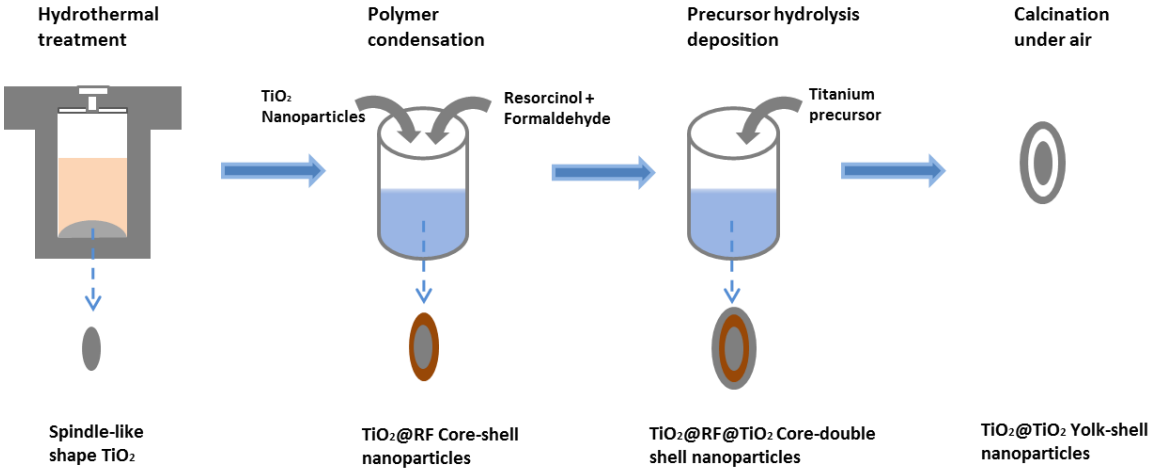

Scheme 6.1: Schematic illustration of synthesis steps of TiO_2@TiO_2 yolk-shell nanoparticles.

6.2 Experimental Section

6.2.1 Chemicals and reagents

Resorcinol (99%), ammonium hydroxide solution (25%), formaldehyde aqueous solution (37%), polyvinylpyrolidone PVP-40 (MW=40000), formaldehyde (36.5%-38%), titanium(IV) butoxide (reagent grade 97%), acetic acid (>99.7%), absolute ethanol, hydrochloric acid (HCl) were purchased from Sigma-Aldrich company and used as supplied. Ammonia solution (25%) was purchased from VWR International PTY LTD. Water was purified by a Milli Q system and had an electrical resistance of 18 MΩ•cm.

6.2.2 Preparation of Spindle-like shape TiO_2 nanoparticles

The preparation of spindle-like TiO2 nanoparticles was based on D. Wu and co-workers' work (16) with some modifications. 0.2 g of PVP (MW-40,000) was firstly added into 30 ml of acetic acid, mixture was stirred magnetically for few minutes before 1ml of TBOT was injected dropwise. Solution was kept stirred for 10 min then transferred into 50 mL a Teflon-liner autoclave and underwent hydrothermal treatment in an electrical oven at 180 °C for 24 hour. The autoclave was cooled naturally to room temperature, and precipitates were collected through centrifugation and washed with alcohol aqueous three times before dried at 60 °C for at least 6 hour.

6.2.3 Preparation of TiO_2@RF core-shell nanoparticles

100 mg of as-prepared TiO_2 cores were added into ethanol and water mixture (V/V 3/7) and dispersed through ultrasonic treatment for at least 15 min before moving back to magnetic stirring plate. Subsequently, 2 ml of CTAB (0.1 M) and 0.2 ml of ammonia solution (25 wt%) were added into mixture followed by adding 0.05 g of resorcinol. After 30 min 0.07 ml of formaldehyde was injected in and such mixture was kept stirring for 24 hour at 35°C before products were collected and washed. TiO_2@RF nanoparticles were then dried at 80 °C for 6 hour.

6.2.4 Preparation of TiO2@RF@TiO2 core-double shell nanoparticles

The synthesis method of coating of TiO2 layer followed C. Wang and his co-workers' work (19) and W. Tu and his colleagues' work (15) with slight modifications. 50 mg of TiO2@RF core-shell nanoparticles were dispersed in 25 ml of absolute ethanol via sonication for 15 min. The mixture was magnetically stirred at 45 °C with adding of 0.1 ml of ammonia solution (25 wt%) for 2 hour. Then 0.5 ml of TBOT was dropped in then kept stirred for 24 hour before final product was collected and washed. TiO_2@RF@TiO_2 core-double shell nanoparticles were dried at 60 °C for at least 8 hour.

6.2.5 Preparation of TiO2@TiO2 yolk-shell nanoparticles

TiO_2@RF@TiO_2 core-double shell nanoparticles were calcined at 500 °C for 1 hour with temperature increment at 1 °C per min in air.

6.2.6 Characterisation

Transmission electron microscopy (TEM) images were acquired with a JEOL 2100 microscope operated at 120 KV. Samples were prepared by suspending fine powder products in 100% ethanol under sonication and placing a drop of the suspension onto a carbon coated gold grid and allowing the ethanol to evaporate naturally before analysis. XRD measurements were obtained using a Bruker-AXS D8 Advance Diffractometer with Cu Kα radiation (40 KV, 40 mA) and a LynxEye position sensitive detector. Information on crystalline phases was confirmed against the database of JCPDS files.

6.3 Results and Discussion

6.3.1 Synthesis and characterisations of TiO_2@TiO_2 yolk-shell nanoparticles

As illustrated in Scheme 6., the synthesis of spindle-like TiO_2 nanoparticles was via a solvothermo method using acetic acid as the reaction media and PVP as the copping agent. Clear acetic acid solvent changed to white milky solution immediately after adding TBOT dropwise which indicates the rapid condensation of titanium precursor. Such mixture was heated up to 180°C and kept for 24 hour for generating the uniform size and unique shape TiO_2 particles. As shown in Figure 6. (a), the spindle-like TiO_2 nanoparticles are approximate 100 nm in length and 50 nm in width. A layer of RF was deposited uniformly outside TiO_2 particles (about 40 nm) formed a core-shell structured TiO_2@RF particles, as seen in Figure 6. (b). The synthetic effect of copping agent was investigated by varying the PVP amount added into this fabrication process. Through the observation of TEM measurements (Figure), it was proved that PVP has impact on the formation of TiO_2 particles to some extent in terms of morphology. The TiO_2 particle size increased with decrease of PVP amount, and particles are rounder than those generated with higher content of PVP. Together with the study in Chapter 3, it confirms again that PVP possesses certain ability in controlling the formation of metal nanoparticles, it restricts the extensive growth of particles resulting smaller and more dispersed products.

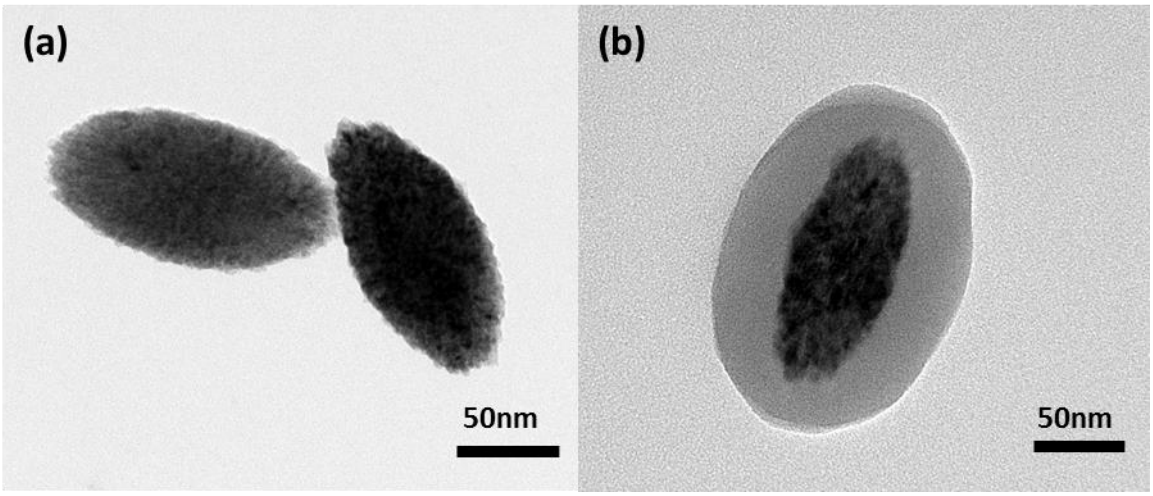

Figure 6.1: (a) TEM image of spindle-like TiO_2 particles; (b) TEM image of spindle-like TiO_2@RF core-shell particles.

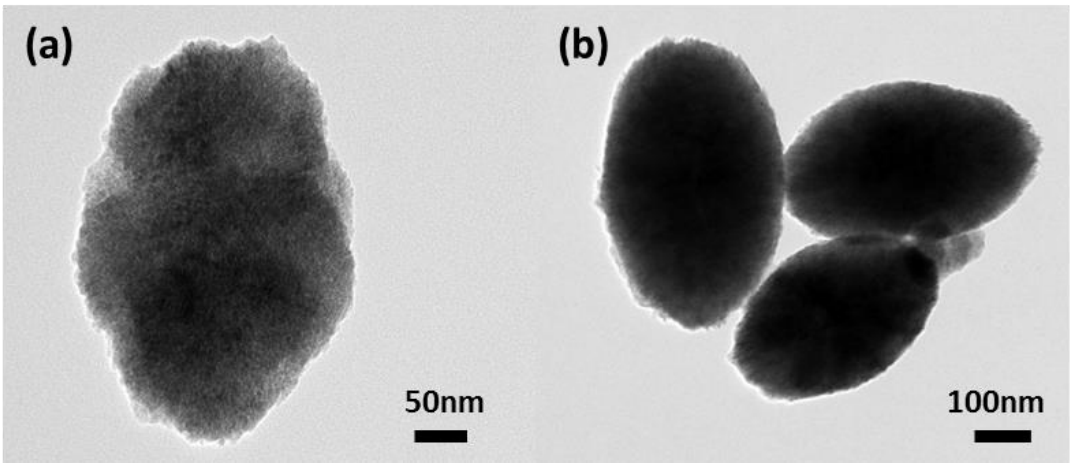

Figure 6.2: (a) TEM image of TiO_2 particles synthesized without PVP; (b) TEM image of TiO_2 particles synthesized with 0.1 g PVP.

A layer of TiO2 was coated outside sol-gel derived RF shell to form a double shelled core-shell particle TiO_2@RF@TiO_2 via a versatile kinetic controlled coating method, as seen in Figure (a). The shell thickness is approximately 50 nm, and this thickness could be controlled by varying the amount of TBOT in this synthesis step. The temperature is a critical factor in this coating process; and 45°C was set as the reacting temperature. It was found that lower reacting temperature could result very fragile and ultra-thin of TiO_2 shell and TiO_2 fragments, as seen in Figure (a). Moreover, isopropyl alcohol was also tested to replace absolute ethanol for TiO_2 shell coating, as indicated in Figure (b), no solid TiO2 layer formed outside

TiO2@RF particles, and no titanium oxide fragments was observed via TEM measurements as well. Therefore, it is suspected that titanium precursor rapidly hydrolysed but no sufficient condensation reaction happened to precipitate the solid TiO_2 shell or fragments (20). In order to create yolk-shell structure, core-double shelled TiO_2@RF@TiO_2 particles were calcined at 500°C for 1 hour with temperature increment of 1°C/min under air. This process removed the sacrificing template RF layer to generate void in between yolk and shell resulting the final TiO_2@TiO_2 yolk-shell nanoparticles, as seen in Figure (b). It is clear that the structure was not perfectly kept after calcination. Some of TiO_2 shells broke and shrunk into a clump of small TiO_2 pieces co-existing with TiO_2 yolks, as shown in Figure . Calcination at moderate temperature can develop highly crystalline TiO_2 particles (11), but it also destroys the structure of nanoparticles. Therefore, a slower temperature increment is expected to maintain the architecture of final products. The composition of yolk-shell TiO_2@TiO_2 nanoparticles was identified through XRD and HRTEM measurements. As seen in Figure (c) and (d), the XRD peaks fits perfectly with data obtained from JCPDS files (no. 21-1272) indicating a typical Anatase TiO_2, and the lattice spacing of 0.35 nm in the HRTEM image corresponds to the (101) lattice planes.

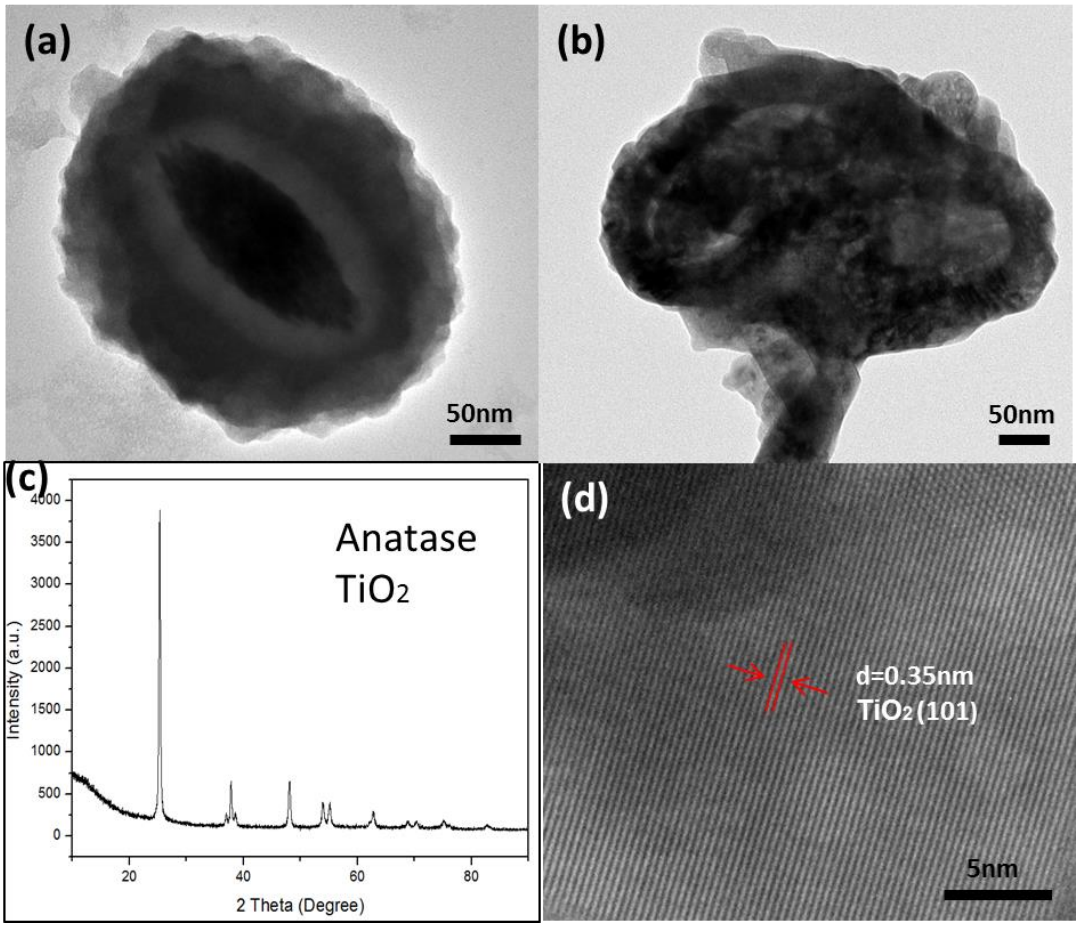

Figure 6.3: (a) TEM image of core-double shell TiO_2@RF@TiO_2 particle; (b) TEM image of yolk-shell structured TiO_2@TiO_2 particles; (c) XRD measurement of TiO_2@TiO_2 yolk-shell particles; (d) HRTEM of TiO_2@TiO_2 yolk-shell particles.

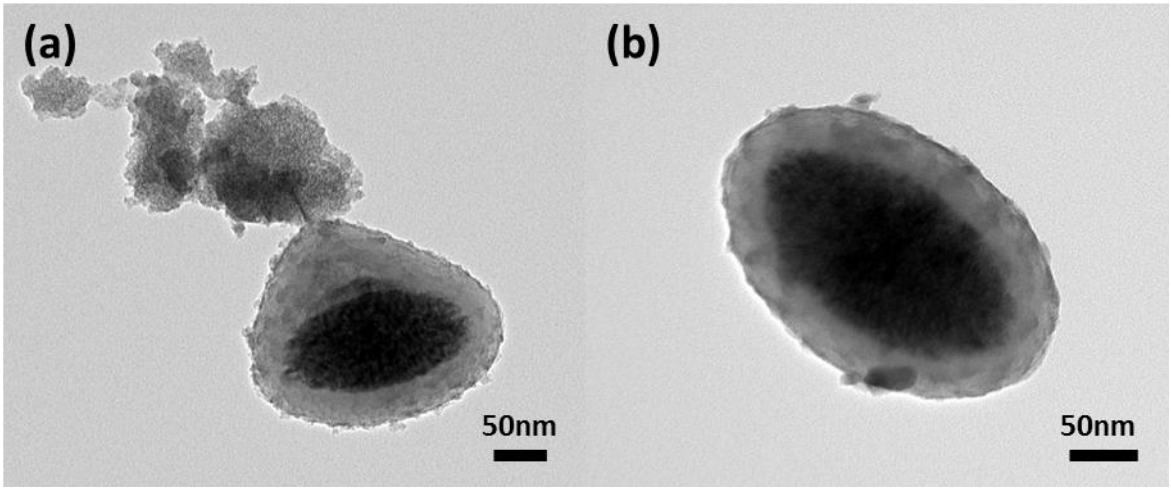

Figure 6.4: (a) TEM image of TiO_2@RF@TiO_2 particle with TiO2 shell coating temperature at room temperature; (b) TEM image of TiO_2@RF@TiO_2 particle using isopropyl alcohol.

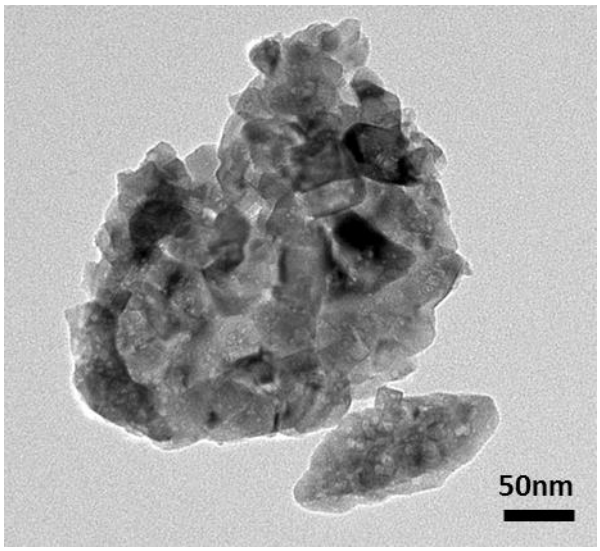

Figure 6.5: TEM image of broken TiO_2@TiO_2 particles after calcination.

6.4 Conclusions

TiO_2@TiO_2 yolk-shell structured particles were prepared by a fabrication process consisting of solvothermo, sol-gel, kinetic controlled and calcination methods. RF layer was used as a sacrificing and removed by simple calcination under air to create yolk-shell structured final products. TBOT was chosen as the titanium precursor for this study, the hydrolysis and condensation steps of such precursor are very important for forming a well-designed TiO_2 yolk and shell. Many difficulties remain in synthesizing such yolk-shell nanoparticles; further study is required to tailor the fabrication method. It is believed that well-designed TiO_2@TiO_2 yolk-shell structured particles will be versatile in many catalysis applications, especially photocatalysis.

Reference

1. Sambur JB, Chen T-Y, Choudhary E, Chen G, Nissen EJ, Thomas EM, et al. Sub-particle reaction and photocurrent mapping to optimize catalyst-modified photoanodes. Nature. 2016;530(7588):77-80.

2. Tang C, Liu L, Li Y, Bian Z. Aerosol spray assisted assembly of TiO2 mesocrystals into hierarchical hollow microspheres with enhanced photocatalytic performance. Applied Catalysis B: Environmental. 2017;201:41-7.

3. Ravishankar TN, Vaz MdO, Ramakrishnappa T, Teixeira SR, Dupont J. Ionic liquid assisted hydrothermal syntheses of Au doped TiO2 NPs for efficient visible-light photocatalytic hydrogen production from water, electrochemical detection and photochemical detoxification of hexavalent chromium (Cr6+). RSC Advances. 2017;7(68):43233-44.

4. Ge M, Cao C, Huang J, Li S, Chen Z, Zhang K-Q, et al. A review of one-dimensional TiO2 nanostructured materials for environmental and energy applications. Journal of Materials Chemistry A. 2016;4(18):6772-801.

5. Liu B, Wang Q, Yu S, Jing P, Liu L, Xu G, et al. Architecture engineering toward highly active palladium integrated titanium dioxide yolk-double-shell nanoreactor for catalytic applications. Nanoscale. 2014;6(20):11887-97.

6. Zhou W, Du G, Hu P, Li G, Wang D, Liu H, et al. Nanoheterostructures on TiO2 nanobelts achieved by acid hydrothermal method with enhanced photocatalytic and gas sensitive performance. Journal of Materials Chemistry. 2011;21(22):7937-45.

7. Kment S, Riboni F, Pausova S, Wang L, Wang L, Han H, et al. Photoanodes based on TiO2 and [small alpha]-Fe2O3 for solar water splitting - superior role of 1D nanoarchitectures and of combined heterostructures. Chemical Society Reviews. 2017;46(12):3716-69.

8. Yao X, Liu X, Liu T, Wang K, Lu L. One-step and large-scale synthesis of anatase TiO2 mesocrystals along [001] orientation with enhanced photocatalytic performance. CrystEngComm. 2013;15(47):10246-54.

9. Li Y, Wang S, Lei D, He Y-B, Li B, Kang F. Acetic acid-induced preparation of anatase TiO2 mesocrystals at low temperature for enhanced Li-ion storage. Journal of Materials Chemistry A. 2017;5(24):12236-42.

10. Li H, He Y, Liu Z, Jiang B, Huang Y. A flexible thin-film membrane with broadband Ag@TiO2 nanoparticle for high-efficiency solar evaporation enhancement. Energy. 2017;139:210-9.

11. Primo A, Corma A, Garcia H. Titania supported gold nanoparticles as photocatalyst. Physical Chemistry Chemical Physics. 2011;13(3):886-910.

12. Zeng M, Li Y, Mao M, Bai J, Ren L, Zhao X. Synergetic Effect between Photocatalysis on TiO2 and Thermocatalysis on CeO2 for Gas-Phase Oxidation of Benzene on TiO2/CeO2 Nanocomposites. ACS Catalysis. 2015;5(6):3278-86.

13. Shojaie A, Fattahi M, Jorfi S, Ghasemi B. Hydrothermal synthesis of Fe-TiO2-Ag nano-sphere for photocatalytic degradation of 4-chlorophenol (4-CP): Investigating the effect of hydrothermal temperature and time as well as calcination temperature. Journal of Environmental Chemical Engineering. 2017;5(5):4564-72.

14. Lee YJ, Joo JB, Yin Y, Zaera F. Evaluation of the Effective Photoexcitation Distances in the Photocatalytic Production of H2 from Water using Au@Void@TiO2 Yolk–Shell Nanostructures. ACS Energy Letters. 2016;1(1):52-6.

15. Tu W, Zhou Y, Li H, Li P, Zou Z. Au@TiO2 yolk-shell hollow spheres for plasmon-induced photocatalytic reduction of CO2 to solar fuel via a local electromagnetic field. Nanoscale. 2015;7(34):14232-6.

16. Wu D, Cao K, Wang H, Wang F, Gao Z, Xu F, et al. Tunable synthesis of single-crystalline-like TiO2 mesocrystals and their application as effective scattering layer in dye-sensitized solar cells. Journal of Colloid and Interface Science. 2015;456:125-31.

17. Yang M, Dong B, Yang X, Xiang W, Ye Z, Wang E, et al. TiO2 nanoparticle/nanofiber-ZnO photoanode for the enhancement of the efficiency of dye-sensitized solar cells. RSC Advances. 2017;7(66):41738-44.

18. Ziarati A, Badiei A, Mohammadi Ziarani G, Eskandarloo H. Simultaneous photocatalytic and catalytic activity of p–n junction NiO@anatase/rutile-TiO2 as a

noble-metal free reusable nanoparticle for synthesis of organic compounds. Catalysis Communications. 2017;95(Supplement C):77-82.

19. Wang C, Wang F, Zhao Y, Li Y, Yue Q, Liu Y, et al. Hollow TiO2–X porous microspheres composed of well-crystalline nanocrystals for high-performance lithium-ion batteries. Nano Research. 2016;9(1):165-73.

20. Velasco MJ, Rubio F, Rubio J, Oteo JL. Hydrolysis of Titanium Tetrabutoxide. Study by FT-IR Spectroscopy. Spectroscopy Letters. 1999;32(2):289-304.

Chapter 7: Conclusions and Perspectives

7.1 Conclusions

In this thesis, a brief summary has been done to summarize the general synthesis methods of yolk-shell structured nanoparticle and resent uses as nanoreactors in energy-conversion applications covering utilization of carbon sources, photosynthesis and fuel cell. The current synthesis methods of yolk-shell structured nanoparticles are usually complex involving multiple-step and hazardous chemicals, and are also lacking of precious control in fabrication resulting low uniformity and quality. Such drawbacks are preventing yolk-shell structured nanoreactors being fabricated in large scale and used commercially. Therefore, facile, low cost and versatile synthesis methods are much desirable.

7.1.1 Brush-like copper oxide encapsulated within mesoporous silica shell yolk-shell nanoparticles

The study of designed advanced yolk-shell nanoreactors started with the understanding the effects of synthetic parameters in fabrication process. Brush-like CuO encapsulated within SiO_2 mesoporous shell was firstly designed and synthesized using RF as the sacrificing template via a common selective etching process. It was discovered that PVP and CTAB have significant influence on the structure and size of CuO nanoparticles, and this conclusion was confirmed again in the following study; and calcination temperature and shell thickness are critical for maintaining the shape of brush-like yolks.

7.1.2 Yolk-shell structured Fe@ɣ-Fe_2O_3 nanoparticles loaded graphitic porous carbon for efficient oxygen reduction reaction

Study continued on designing the synthesis method to prepare Cu/ɣ-Fe_2O_3@C, Cu/Fe@ɣ-Fe_2O_3@C core-shell particles and highly graphitic carbon particles. The brush-like CuO nanoparticles played an important role in creating Cu doped Fe@ɣ-Fe_2O_3 yolk-shell nanoparticles. The evaluations of electrochemical catalytic activities

of as-prepared nanoreactors were carried out through ORR. The results indicated that such catalysts possess reasonably good electrocatalytic performances, and were believed to be a promising candidate for fuel cell applications with further modification.

7.1.3 Ni and Co attached Cu/Cu_2O@C core-shell nanoparticles

Iron precursor from previous study was replaced by nickel and cobalt precursor. The brush-like CuO nanoparticles were reduced to Cu_2O and Cu cores via the annealing process under nitrogen gas flow and ultra-fine Co_3O_4 nanoparticles formed in the cobalt attached sample. The ORR testings were conducted again for examining the catalytic activities of nickel and cobalt attached samples. According to the ORR results, Co-Cu/Cu_2O@C nanocatalyst exhibited the best electrochemical performance, because of its small Cu/Cu_2O particles size, synergetic effects of core-shell structure and the formation of ultra-fine Co_3O_4 nanoparticles.

7.1.4 Synthesis of TiO_2@TiO_2 yolk-shell nanoparticles

In this study, TiO_2@TiO_2 yolk-shell structured particles were fabricated via a four-step synthesis method. As same as in chapter 3, RF layer was used as sacrificing template for creating yolk-shell structure at last. TBOT was chosen as the titanium precursor, and it its hydrolysis and condensation were very critical in forming a well-designed TiO_2 nanoparticle. The influence of PVP polymer in controlling the size and shape of metal nanoparticles was studied again, it was further proved that higher concentration of polymer in solution will lead to smaller metal nanoparticles.

7.2 Perspectives

1. The main focus of the works in this thesis is to design fabrication methods for yolk-shell structured nanoparticles. Although copper oxide, iron precursor, cobalt precursor, nickel precursor and titanium oxide were used, the material selection was quite limited. Metal organic framework is very popular in the research field for generating complex structured nanoparticles due to its organic ligands content. Thus, it is expected that such material could have great potentials for synthesizing metal

yolk with metal shell yolk-shell nanoparticles with precious control in size and quality.

2. Ostwald Ripening and inward diffusion of Kirkendall Effect were proposed to be the formation mechanism of Fe@ɣ-Fe_2O_3 in Chapter 4 leaving an uncertainty in this study. A systematic and detail investigation should be conducted to discover the true mechanism behind this transformation, and it will definitely make a big contribution for synthesizing other yolk-shell metal nanoparticles via this facile synthesis route.

3. ORR tests were carried out to determine the electrocatalytic ability of Cu/ɣ-Fe_2O_3@C and Cu/Fe@ɣ-Fe_2O_3@C particles. However, it is believed that these catalysts may also have good catalytic activity for lithium-ion battery application. Such testing shall be done to reveal more possibility of these catalysts.

4. Electrochemical reduction of CO_2 testings were conducted over Ni-Cu/Cu2O@C, Ni-Cu@C, Co-Cu/Cu2O@C and Co-Cu @C samples showing low CO and H_2 production. Therefore, it is suspected that organic compounds properly formed as the final products. However, such testing is still at its initial stage, comprehensive report will be done after obtaining the full results.

5. The synthesis of TiO_2@TiO_2 yolk-shell structured particles is not perfect at this stage, some shells collapse after calcination leaving yolks exposed. Slower temperature increment may help for maintaining the yolk-shell structures. Moreover, catalytic application is yet tested for this sample. It is believed that such nanocatalysts may have excellent activity towards photocatalytic applications. The void size and porosity of TiO_2 shell may need to be further tailored for future testing in photocatalytic reactions.

Appendix: Permission of Reproduction from the Copyright Owner

Chapter 2: Literature Review

10/24/2017 Rightslink® by Copyright Clearance Center

Copyright Clearance Center RightsLink®

Home | Account Info | Help

Title: Advanced yolk-shell nanoparticles as nanoreactors for energy conversion

Author: Meiwen Wang,Yash Boyjoo,Jian Pan,Shaobin Wang,Jian Liu

Publication: Chinese Journal of Catalysis

Publisher: Elsevier

Date: June 2017

Logged in as:
Meiwen Wang
Account #:
3001126026
LOGOUT

Please note that, as the author of this Elsevier article, you retain the right to include it in a thesis or dissertation, provided it is not published commercially. Permission is not required, but please ensure that you reference the journal as the original source. For more information on this and on your other retained rights, please visit: https://www.elsevier.com/about/our-business/policies/copyright#Author-rights

BACK CLOSE WINDOW

https://s100.copyright.com/AppDispatchServlet 1/1

Chapter 4: Yolk-shell structured Fe@ɣ-Fe2O3 nanoparticles loaded graphitic porous carbon for efficient oxygen reduction reaction